Pion Interferometry in 158 GeV/Nucleon Pb+Pb Collisions

DISSERTATION

Presented in Partial Fulfillment of the Requirements for the Degree Doctor of Philosophy in the Graduate School of The Ohio State University

By

David H. Hardtke, B.S.

* * * * *

The Ohio State University

1997

Dissertation Committee:

Dr. Thomas J. Humanic, Advisor

Dr. Evan R. Sugarbaker

Dr. Eric Braaten

Dr. David Stroud

Approved by

____

Advisor

Department of Physics

Abstract

Pion interferometry measurements are made for the reactions Pb+Pb$\rightarrow \pi^-\pi^- + X$ and Pb+Pb$\rightarrow \pi^+\pi^+ + X$ using the 158 GeV/nucleon ^{208}Pb beam from the CERN Super Proton Synchrotron (SPS). Two-particle intensity interferometry measurements are sensitive to the spatial and temporal extent of the source as well as the expansion dynamics of the system. Experiment NA44, a focussing spectrometer, is used in two angular settings (44mr and 131mr) to identify and track pions in a small acceptance region near mid-rapidity at two different mean transverse momenta (150 MeV/c and 450 MeV/c). The data are corrected for two-particle Coulomb interactions and experimental distortions, and then the correlation functions are parameterized in terms of gaussian radius parameters.

The radius parameters extracted from the pion interferometry measurements are significantly larger than the projectile size, which suggests that the system expands before freeze-out. The radius parameters decrease with increasing transverse momentum as would be expected for an expanding source. The results do not suggest the long-lived source expected in the case of a first-order phase transition from a Quark-Gluon Plasma.

The radius parameters extracted from Pb+Pb collisions at 158 GeV/nucleon are slightly larger than those extracted for S+Pb collisions at 200 GeV/nucleon, but they do not scale with the nuclear radii of the projectile. The current correlation radii are similar to the results from Au+Au collisions at 10.6 GeV/nucleon.

The Relativistic Quantum Molecular Dynamics (RQMD) model predicts radius parameters that are equal to or slightly larger than the measured radius parameters. A simple rescattering model gives similar predictions to the RQMD model, suggesting that final state rescattering is largely responsible for the trends observed in the data. The rescattering model is also used to evaluate the effects of the nuclear Coulomb field on the HBT results, and it is found using a classical approximation that the nuclear Coulomb field leads to a small reduction in the measured interferometric radius parameters.

Acknowledgments

I would like to thank each member of the NA44 collaboration for making this thesis possible. This includes both those people I had the priveledge of working with and those who came before me and built the experiment. In particular I would like to thank Jerry Dodd for teaching me about the MC, Achim Franz for helping me to understand the hardware, and Nu Xu for helping me to understand the physics. There are many others who I must thank, including Hans Bøggild, Hubert van Hecke, Ian Bearden, Atsushi Sakaguchi, Michael Murray, Barbara Jacak, Hiroaki Ohnishi, Roman Malina, Dennis Reichhold, and Shinichi Esumi. I would also like to acknowledge the contributions of the late Kazuhiro Kaimi.

Four people have been so instrumental in my growth as a physicist that they deserve a separate paragraph. I would like to thank Rama Jayanti for showing me the basics of HBT when I did not know what a pion was. I would like to thank Sanjeev Pandey for teaching me that problems that disappear are not solved unless they are also understood. I would like thank John Sullivan for helping me to figure out many of the technical problems that plagued these measurements and for his generous assistance. I would like to thank my advisor, Tom Humanic, for allowing me to work somewhat independently while keeping me focussed.

I would also like to thank those at the Van de Graaff. These people include Gaspare LoCurto, Dan Cooper, Evan Sugarbaker, Michael Lisa, Ivan Kotov, Howard Dyke, and Linda O'Brien.

Finally, I must thank my Father, Mother, and Brother for giving me constant support.

VITA

April 10, 1973 .... Born - Burlingame, CA

1994 .... B.S. Physics
Duke University
Durham, NC

1994-1995 .... Graduate Teaching Assistant
Department of Physics
The Ohio State University
Columbus, OH

1995-present .... Graduate Research Assistant
Department of Physics
The Ohio State University
Columbus, OH

Publications

Collective Expansion in High Energy Heavy Ion Collisions, I.G. Bearden, *et al.*, Phys. Rev. Lett. **78**, 2080 (1997).

Mid-rapidity protons in 158A GeV Pb+Pb collisions, I.G. Bearden, *et al.*, Phys. Lett. **B388**, 431 (1996).

Coulomb effects in single-particle distributions, H. Bøggild, *et al.*, Phys. Lett. **B372**, 339 (1996).

Probing the Space-Time Evolution of Heavy-Ion Collsions: Recent Results from the CERN Experiment NA44, I.G. Bearden, *et al.*, Nucl. Phys. **A610**, 240c (1996).

Hadron Distributions - Recent Results from the CERN Experiment NA44, I.G. Bearden, *et al.*, Nucl. Phys. **A610**, 175c (1996).

Charged hadron distributions in pA and AA collisions at the CERN SPS, H. Bøggild, *et al.*, Nucl. Phys. **A590**, 523c (1995).

Recent Results from NA44 and a Review of HBT, B.V. Jacak for the NA44 collaboration, Nucl. Phys. **A590**, 215c (1995).

Fields of Study

Major Field: Physics

Table of Contents

List of Figures

FIGURE PAGE

List of Tables

CHAPTER 1

INTRODUCTION

Ultra-relativistic heavy-ion physics straddles the boundary between traditional nuclear and high energy physics. In nuclear physics, the relevant degrees of freedom are protons and neutrons which interact via meson exchange. In high energy physics, the relevant degrees of freedom are constituent quarks and leptons which interact via the exchange of gauge bosons. Nuclear physics attempts to explain the strong interaction in the low energy limit; high energy physics attempts to explain the strong interaction in the high energy limit. Somewhere between these two limits, however, is a regime that had not been explored either theoretically or experimentally until the emergence of relativistic heavy-ion physics.

Figure 1.1 shows the theoretically predicted phase diagram for nuclear matter. In the ground state, protons and neutrons are bound in nuclei. If this nuclear matter is heated or compressed, a hadron gas is created where the relevant degrees of freedom are protons, neutrons, and other short lived hadrons (π, K, Λ, etc.). If further heating and/or compression occurs, hadrons can no longer exist and quarks and gluons become the relevant degrees of freedom. This state of matter is known as the quark-gluon plasma (QGP), and is thought to have existed until $\approx 10^{-6}$s after the Big Bang.

Lattice QCD (Quantum Chromodynamics) simulations have been used to investigate quantitatively both the critical temperature (T_C) for the QGP phase transition and the order of the phase transition. The current estimate for the critical temperature from lattice QCD simulations is 140 MeV [Lae96]. The order of the phase transition depends on the number of light quark flavors. If there are three or more light quark flavors, then the transition is predicted to be first order. For two light quark flavors, it has not yet been determined whether the phase transition is first order or continuous. Nonetheless, lattice QCD makes the unambiguous prediction that the QGP phase transition should exist so the experimental observation of quark matter would be an important confirmation of QCD.

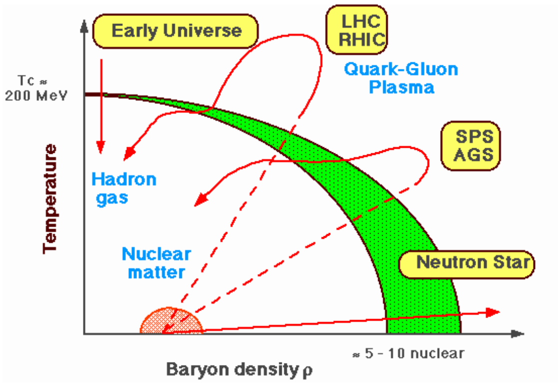

Figure 1.1: The theoretically predicted phase diagram for nuclear matter.

The goal of ultra-relativistic heavy ion physics is to create the conditions thought to be necessary for QGP formation in the laboratory. The predicted space-time evolution of an ultra-relativistic heavy-ion collision is shown in Figure 1.2. It is thought that sufficiently energetic nuclear collisions can create the necessary temperatures and/or energy densities for the quark-gluon plasma phase. Experiments are used to probe the system and look for evidence of new physics that cannot be explained using conventional hadronic models.

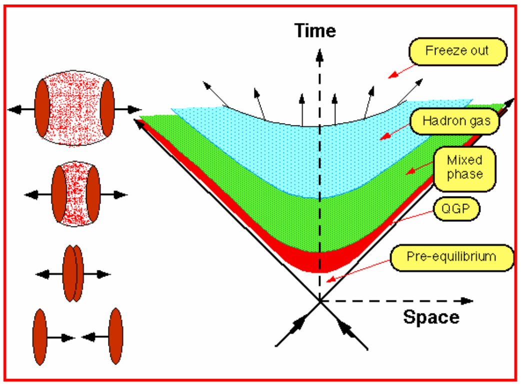

Figure 1.2: The theoretically predicted space-time evolution of a relativistic nuclear collision.

This thesis will examine hadronic data from the most energetic nucleus-nucleus collisions studied so far, Pb+Pb collisions at 158 GeV/nucleon. Specifically, intensity interferometry between identical bosons will be used to study the spatial and temporal extent of the excited nuclear system at hadronic freeze-out. These measurements will be compared to models, and the models will then be used to look back into the early stages of the collision.

CHAPTER 2

THEORY OF INTENSITY INTERFEROMETRY

By definition, hadrons (i.e. bound quark states) cannot probe the deconfined QGP state directly. Even in the absence of a QGP state, strongly interacting hadrons only probe the early stages of the nucleus-nucleus collision indirectly. Why then does one wish to measure and understand the hadronic observables from relativistic nucleus-nucleus collisions?

1. Hadrons are the most abundantly produced particles in relativistic nucleus-nucleus collisions and hence the easiest to measure.

2. Hadrons carry away most of the energy from the collision region. They are important for inferring the energy density, spatial extent, and dynamics of the system.

3. Hadronic spectra can be used to infer whether the system reaches an equilibriated state and can be used to indirectly infer several important thermodynamic quantities including the temperature and pressure of the system.

4. Hadronic correlations probe the space-time geometry the system.

5. Any valid model of a relativistic heavy-ion collision must be able to reproduce the hadronic data. Thus hadronic observables are a very important test for the theories.

This chapter will present the theoretical foundations of hadronic measurements with a particular focus on two particle intensity interferometry. First, the phase-space density function formalism that allows a connection between theory and experiment will be developed. This phase-space density function formalism will then be related to single particle measurements. The theory, practice, and interpretation of two particle intensity interferometry will then be discussed in detail.

2.1 The Phase Space Density Function

In practice, hadronic measurements are used to constrain models of relativistic heavy-ion collisions. These models include cascade models, hydrodynamical models, and simple analytic models. In order for a model to be valid, its predictions must be in agreement with the experimental data. Comparing experimental data with a model, however, is not entirely straightforward. To accomplish this goal, the phase space density function formalism is used.

The phase space density function, $S_i(x, p)$, gives the probability of emitting a particle of type i (i.e. π, K, p, etc.) from position x with momentum p. The laws of quantum mechanics state that it is impossible to accurately measure the position and momentum of a particle simultaneously. It is possible, however, to relate the phase space density function to experimentally measured observables using some well established theoretical approximations.

One common experimental observable is the single inclusive particle yield, $dN_i/d^3\vec{p}$. This observable can be related to the phase space density function by integrating it over all space:

$$E_p \frac{dN_i}{d^3\vec{p}} = \int d^4x S_i(x,p), \tag{2.1}$$

where E_p is the energy of a particle with momentum $\vec{p}$. In doing this integral, all of the geometric and temporal information about the particle emitting source is lost. This means that measured single inclusive particle yields are unable to constrain the space-time geometry of the particle emitting source.

2.2 Basics of Intensity Interferometry

The technique of intensity interferometry allows for an indirect extraction of the space-time geometry of a particle-emitting source under certain conditions. This technique was originally developed by Hanbury-Brown and Twiss to measure the size of distant stars [HBT56]. Because of their pioneering efforts, the technique of intensity interferometry is commonly know as HBT. The first application of the technique to subatomic reactions was by Goldhaber, Goldhaber, Lee and Pais [GGLP60] who invoked the concept of Bose-Einstein statistics to explain the anomalous angular distribution of pions created in $\bar{p}-p$ annihilation experiments.

The basic diagram for all HBT experiments is shown in Figure 2.1. A source, characterized by a distribution $\rho(\vec{x})$, emits two identical particles from positions $\vec{x}_1$ and $\vec{x}_2$. These particles are measured to have momenta $\vec{p}_1$ and $\vec{p}_2$ at some detector(s). It is impossible, however, to determine whether the particle with momenta $\vec{p}_1$ came from position $\vec{x}_1$ or position $\vec{x}_2$. If the outgoing particles are bosons (fermions), their final state must be symmetrized (anti-symmetrized). In the ideal case with no final state interactions, the outgoing two-particle wave function ($\Psi_{12}(\vec{x}_1, \vec{x}_2)$) can be written in terms of plane waves as

$$\Psi_{12}(\vec{x}_1, \vec{x}_2) = \frac{1}{\sqrt{2}}(e^{i\vec{p}_1\vec{x}_1}e^{i\vec{p}_2\vec{x}_2} \pm e^{i\vec{p}_1\vec{x}_2}e^{i\vec{p}_2\vec{x}_1}), \tag{2.2}$$

where the (+) sign is for bosons and the (-) sign is for fermions.

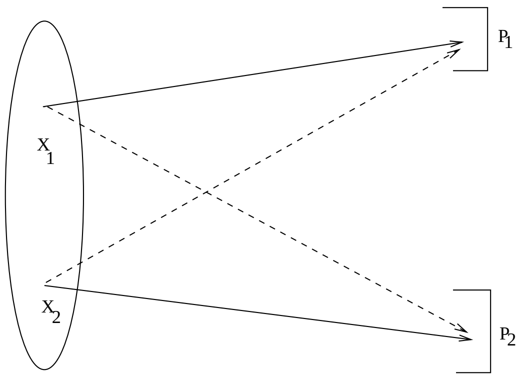

Figure 2.1: Schematic diagram for an HBT experiments.

The probability for observing such a state is different depending on whether the particles are emitted coherently or incoherently. For the case of coherent emission, the probability for observing such a state is given by [BGJ90]

$$P_C(\vec{p}_1,\vec{p}_2) = \frac{1}{2}|\int d^3x_1 d^3x_2 \Psi_{12}(\vec{x}_1,\vec{x}_2) f(\vec{x}_1) f(\vec{x}_2)|^2, \tag{2.3}$$

where $f(\vec{x})$ is the source amplitude at position $\vec{x}$. For fermions, this expression vanishes due to the anti-symmetrized wave function. For bosons, this expression becomes

$$P_C(\vec{p}_1,\vec{p}_2) = |\tilde{f}(\vec{p}_1)\tilde{f}(\vec{p}_2)|^2, \tag{2.4}$$

where $\tilde{f}(\vec{p})$ is the Fourier transform of the source amplitude. The single particle probability for coherent emission is

$$\begin{aligned} P_C(\vec{p}) &= |\int d^3x e^{i\vec{p}\vec{x}} f(\vec{x})|^2 & (2.5)\\ &= |\tilde{f}(\vec{p})|^2. & (2.6)\end{aligned}$$

For the coherent case, the probability for observing two particles with momenta $\vec{p}_1$ and $\vec{p}_2$ factorizes into the individual probabilities for observing particles of momenta $\vec{p}_1$ and $\vec{p}_2$

$$P_C(\vec{p}_1,\vec{p}_2) = P_C(\vec{p}_1)P_C(\vec{p}_2). \tag{2.7}$$

Hence, in the limit of a coherent source, there are no correlations present between the two momenta.

The incoherent emission of a particle can be treated in a similar way except that it is necessary to integrate over the squared amplitudes. In this case the source amplitude $f(\vec{x})$ is replace by a random variable that must be averaged over. The probability for observing a single particle of momentum $\vec{p}$ is

$$P_I(\vec{p}) = \int d^3x_1 d^3x_2 (e^{i\vec{p}\cdot\vec{x}_2})^* e^{i\vec{p}\cdot\vec{x}_1} \langle f^*(\vec{x}_2) f(\vec{x}_1)\rangle, \tag{2.8}$$

where $\langle \cdots \rangle$ is the average over the random source amplitude $f(\vec{x})$. For incoherent emission, it is assumed that $f^*(\vec{x}_2)f(\vec{x}_1)$ averages to 0 unless $\vec{x}_1 \approx \vec{x}_2$, in which case the average is proportional to the density distribution of the source $\rho(\vec{x})$. Thus we can write

$$\langle f^*(\vec{x}_2)f(\vec{x}_1)\rangle = \rho((\vec{x}_1 + \vec{x}_2)/2)U(\vec{x}_1 - \vec{x}_2), \tag{2.9}$$

where $U(\vec{x})$ is sharply peaked around $\vec{x} = 0$. Using this, the probability in equation (2.8) reduces to

$$P_I(\vec{p}) = \tilde{U}(\vec{p}) \int d^3x \rho(\vec{x}), \tag{2.10}$$

where $\tilde{U}(\vec{p})$ is the Fourier transform of $U(\vec{x})$.

If two particles are emitted incoherently, the probability for observing such a state is [BGJ90]

$$P_I(\vec{p}_1, \vec{p}_2) =$$
$$\tfrac{1}{2} \int d^3x_1 d^3x_2 d^3x_3 d^3x_4 \Psi^*_{12}(\vec{x}_3, \vec{x}_4)\Psi_{12}(\vec{x}_1, \vec{x}_2)\langle f^*(\vec{x}_3)f^*(\vec{x}_4)f(\vec{x}_1)f(\vec{x}_2)\rangle. \tag{2.11}$$

Once again, equation (2.9) can be used to replace the averages over the randomly fluctuating amplitudes with the density distribution $\rho(\vec{x})$. In this case, however, we can have either $\vec{x}_1 \approx \vec{x}_3; \vec{x}_2 \approx \vec{x}_4$ or $\vec{x}_1 \approx \vec{x}_4; \vec{x}_2 \approx \vec{x}_3$ and this leads to two non-zero terms. The non-zero terms of this expression are are [Bow85]

$$\begin{aligned} P_I(\vec{p}_1, \vec{p}_2) = \tilde{U}(\vec{p}_1)\tilde{U}(\vec{p}_2) \int d^3x_1 d^3x_2 \rho(\vec{x}_1)\rho(\vec{x}_2) \pm \\ [\tilde{U}((\vec{p}_1 + \vec{p}_2)/2)]^2 \int d^3x_1 d^3x_2 \rho(\vec{x}_1)\rho(\vec{x}_2) e^{i(\vec{p}_2 - \vec{p}_1)\cdot(\vec{x}_2 - \vec{x}_1)}. \end{aligned} \tag{2.12}$$

The first term is just the product of the individual observation probabilities, and depends only on the individual momenta $\vec{p}_1$ and $\vec{p}_2$. The second term does not depend on the individual momenta $\vec{p_1}$ and $\vec{p_2}$ but instead depends on the momentum difference $\vec{Q} = \vec{p_1} - \vec{p_2}$ between the two particles and the average momentum of the pair.

The correlation function, $C_2(\vec{p_1}, \vec{p_1})$, is defined as the probability $P(\vec{p_1}, \vec{p_2})$ of observing two particles of momenta $\vec{p_1}$ and $\vec{p_2}$ divided by the individual products of the single particle observation probabilities in the absence of any correlations:

$$C_2(\vec{p_1}, \vec{p_1}) = \frac{P(\vec{p_1}, \vec{p_2})}{P(\vec{p_1})P(\vec{p_2})}. \tag{2.13}$$

For a coherent source, this ratio is unity for all values of $\vec{p_1}$ and $\vec{p_2}$. For a incoherent source, this ratio depends only on the value of the momentum difference $\vec{Q} = \vec{p_1} - \vec{p_2}$ if it is assumed that $U(\vec{x}) = \delta(\vec{x})$ in which case $\tilde{U}(\vec{p})$ is a constant. In this case, the correlation function for an incoherent source becomes [Bow85],

$$\begin{aligned} C_2(\vec{Q}) &= 1 \pm \frac{\int d^3x_1 d^3x_2 \rho(\vec{x}_1)\rho(\vec{x}_2) e^{i(\vec{p}_2 - \vec{p}_1)\cdot(\vec{x}_2 - \vec{x}_1)}}{\int d^3x_1 d^3x_2 \rho(\vec{x}_1)\rho(\vec{x}_2)} && (2.14) \\ &= 1 \pm |\tilde{\rho}(\vec{Q})|^2. && (2.15) \end{aligned}$$

Thus, for incoherently emitted particles, the correlation function measures the Fourier transform of the source distribution.

Thus far, only a static source has been considered in which the distribution $\rho(\vec{x})$ is time independent. This is a reasonable assumption for a star, but in relativistic heavy-ion collisions the source is dynamic and the naive interpretation of the correlation function is not entirely correct. Because of dynamical correlations in the source, HBT does not measure a true "source size" but instead measures only a part of the source and mixes in some temporal information about the source. In addition, due to pions from resonance decay, the measured correlation function in fact represents a superposition of several sources with different sizes.

Equation (2.15) has the following implicit conditions that are not fulfilled in relativistic heavy-ion collisions:

1. There are no position-momentum correlations – *i.e.* a particle of momentum $\vec{p}$ is equally likely to come from any part of the source distribution $\rho(\vec{x})$.

2. The source distribution is static.

3. The outgoing particles can be treated as plane waves – *i.e.* there are no final-state interactions.

2.3 HBT in Dynamical Systems

Equation 2.15 predicts that the correlation function should be a function only of the momentum difference $\vec{Q}$ and independent of the total momenta of pair. For an expanding system, however, this need not be the case [Pra84, Pra86]. Particles of a given velocity are more likely to come from a region of the source that is moving with a similar velocity. Hence, the correlation function is in reality a function of both the momentum difference $\vec{Q}$ and the total average momentum of the pair ($\vec{K} = (\vec{p}_1 + \vec{p}_2)/2$):

$$C_2(\vec{Q}) \rightarrow C_2(\vec{Q}, \vec{K}). \tag{2.16}$$

This has two profound implications for interferometry measurements. First, the interferometric measurements cannot be used to measure the actual size of the source distribution directly. However a measurement of the correlation function as a function of both the momentum difference and total momentum of the particle pair can be used to gain dynamical information about the particle emitting source.

2.4 Final-State Interactions

In deriving equation (2.15) it was assumed that the outgoing particles can be described by plane waves. For hadrons produced in relativistic heavy-ion collisions, this is certainly not the case. For all hadrons there is a strong interaction between the outgoing pair. For charged hadrons, an additional final- state interaction is the Coulomb interaction between the outgoing pair. Additionally, but less important, there is also a Coulomb interaction between the outgoing particles and the residual charge of the nuclear system.

2.4.1 Strong Interaction

In the case of pp correlations, the final-state strong interaction between the outgoing pair is the dominant feature of the correlation function. An attractive S-wave nuclear potential leads to a pronounced peak in the correlation function around $Q \approx 40$ MeV.

The focus of this investigation, however, is $\pi\pi$ correlations and for this system the strong interaction between the outgoing particles is very weak. A repulsive s-wave interaction exists for the I=2 $\pi\pi$ system. The range of this interaction, however is estimated to be around 0.2 fm [BOW88], while the characteristic separation between pions produced in relativistic heavy-ion collisions is around 5 fm.

2.4.2 Coulomb Interaction between Outgoing Particles

Like-sign charged particles are typically used for HBT measurements in relativistic heavy-ion collisions. Charged particle pairs are easily measured, but the observed rate of charged particle pair production is strongly suppressed at low momentum difference due to the Coulomb repulsion between the outgoing particles. This means that the assumption that the particles propagate from the source to the detector as plane waves is not correct. In order to account for this Coulomb repulsion, it is possible to either include the effect in model calculations or to correct the experimental data for the Coulomb suppression. In this work, the experimental data will be corrected.

In the center-of-mass (C.M.) system, the Coulomb scattering between two particles can be reduced to a non-relativistic problem. The two-particle wave function can be factored into a center of mass part and a relative part [Pra86b]:

$$\Psi_{12}(\vec{p}_1, \vec{p}_2; \vec{x}_1, \vec{x}_2) = e^{i(\vec{p}_1+\vec{p}_2)\cdot(\vec{x}_1+\vec{x}_2)/2} \times \psi_r(\vec{p}_1 - \vec{p}_2, \vec{x}_1 - \vec{x}_2), \tag{2.17}$$

where $\psi_r(\vec{p}_1 - \vec{p}_2, \vec{x}_1 - \vec{x}_2)$ is the relative wave function. In the C.M. system, the Schrödinger equation for the Coulomb wave function is [Bay69]

$$(-\frac{\nabla^2}{2m} - E + \frac{e^2}{r})\psi_c(\vec{Q}, \vec{r}) = 0 \tag{2.18}$$

where r is the relative coordinate, $E = Q^2/2m$ is the energy of the particle in the C.M. system, and m is the reduced mass. The scattering solutions of this equation are of the form

$$\psi_c(\vec{Q},\vec{r}) = \Gamma(1+i\eta)e^{-\pi\eta/2}e^{iQr}F(-i\eta|1|iQr - i\vec{Q}\cdot\vec{r}), \tag{2.19}$$

where $\eta = me^2/Q$ and F is the confluent hypergeometric function.

The symmetrized Coulomb wave function is

$$\psi_r(\vec{Q},\vec{r}) = \frac{1}{\sqrt{2}}(\psi_c(\vec{Q},\vec{r}) + \psi_c(\vec{Q},-\vec{r})). \tag{2.20}$$

This can be combined with equation (2.17) and inserted into equation (2.11):

$$P(\vec{p}_1,\vec{p}_2) = \int d^3x_1 d^3x_2 |e^{i(\vec{p}_1+\vec{p}_2)\cdot(\vec{x}_1+\vec{x}_2)/2} \times \psi_r(\Delta\vec{p},\Delta\vec{x})|^2 \rho(\vec{x}_1)\rho(\vec{x}_2). \tag{2.21}$$

This expression is then integrated numerically to calculate the Coulomb wave correction [Pra86b]. When using equation (2.21) to correct real data, the source distribution $\rho(\vec{x})$ is not known in advance, so an iterative approach is used. The distribution $\rho(\vec{x})$ is taken from a gaussian parameterization of the correlation function from the previous iteration.

In the point-source approximation, equation (2.21) is greatly simplified [GKW79]:

$$P(\vec{p}_1,\vec{p}_2) \approx G(\eta)\int d^3x_1 d^3x_2 |e^{i\vec{p}_1\vec{x}_1}e^{i\vec{p}_2\vec{x}_2} + e^{i\vec{p}_1\vec{x}_2}e^{i\vec{p}_2\vec{x}_1}|^2 \rho(\vec{x}_1)\rho(\vec{x}_2), \tag{2.22}$$

where $\eta = me^2/Q$ is the Sommerfeld parameter and $G(\eta)$ is the Gamow penetrability factor:

$$\begin{aligned} G(\eta) &= |\psi_c(\vec{Q},\Delta\vec{x}=0)|^2 \qquad (2.23) \\ &= \frac{2\pi\eta}{e^{2\pi\eta}-1}. \qquad (2.24) \end{aligned}$$

Using this expression, the Coulomb corrected correlation function can be written in terms of the experimentally measured correlation function:

$$C_2(\vec{p}_1, \vec{p}_2) = C_2^{exp}(\vec{p}_1, \vec{p}_2) G^{-1}(\eta). \tag{2.25}$$

This is computationally much simpler than the numerical evaluation of equation (2.21) and has thus been used in most previous HBT analyses. For extended sources, such as those present in Pb+Pb collision, the Gamow factor greatly overpredicts the Coulomb repulsion leading to an overcorrection of the data. Although the most accurate results are obtained using the Coulomb Wave function integration technique, both corrections are used is this analysis since it is necessary to compare to previous data that have been corrected with the Gamow factor.

It has been suggested that the Coulomb interaction between outgoing pions can be measured experimentally by looking at opposite-sign pairs (i.e. $\pi^+\pi^-$) [Alb97]. The assumption is that any correlation between opposite-sign particles arise purely from the Coulomb interaction. This approach would be desirable since it removes the model dependence of the Coulomb correction in equation (2.21). This approach, however, has several flaws. First, even in the point source approximation, the Gamow penetrability factor for opposite-sign particles is not equal to the Gamow penetrability factor for like-sign particles:

$$\frac{-2\pi\eta}{e^{-2\pi\eta} - 1} = e^{2\pi\eta} \frac{2\pi\eta}{e^{2\pi\eta} - 1}. \tag{2.26}$$

Of even more concern, however, are the experimental limitations. Due to finite momentum resolution, the measured correlation functions are a convolution of the true correlation and the detector resolution. This means that any measured opposite-sign correlation function used to correct the like-sign correlation function for two-particle Coulomb repulsion needs to be taken by the same experiment and in the same impact parameter range. Because of this experimental limitation, this Coulomb correction approach will not be used.

2.4.3 Central Coulomb Interactions

The influence of the central Coulomb potential on the outgoing particle pair has been largely ignored theoretically, primarily because of the insolubility of the three-body Coulomb problem. The central Coulomb potential is created by the primary protons in the projectile and target. For Pb+Pb collisions, this Coulomb potential could be quite large, so its influence on the measured correlation functions will be investigated.

At Bevelac Energies ($\approx$ 0.1-1.0 GeV/nucleon), strong Coulomb effects were observed experimentally in the π^+ and π^- inclusive yields [Ben79, Sul82]. This lead to great theoretical interest on the influence of the nuclear Coulomb charge on pions originating from nuclear collisions. A thorough theoretical investigation [GK79] showed that simple Coulomb effects could completely account for the observations if a realistic charged source distribution is used and quantum mechanical and relativistic effects are taken into account.

The formalism developed in [GK79] was first extended to interferometry measurements in [ZAJ84] and subsequently in [Cha91]. In [ZAJ84] it was observed that the $\pi^-\pi^-$ and $\pi^+\pi^+$ interferometry measurements in Ar+KCl collisions at 1.8

GeV/nucleon give different results. It was speculated that this difference might be due to the nuclear charge. The approach used in these works was to analytically correct the observed pion momenta for the effects of the nuclear Coulomb interaction. In order to use the formalism of [GK79], however, the source geometry and dynamics are needed as inputs to the calculation. In addition, it is assumed in this approach that the many-body Coulomb interaction can be factorized into the two-body Coulomb interaction between the outgoing pair and the two-body Coulomb interactions between the outgoing pions and the nuclear charge fragment. Using this approach, it was found in [ZAJ84] that the effects of the nuclear Coulomb charge effects were very small and could not explain the difference between the $\pi^+\pi^+$ and $\pi^-\pi^-$ interferometry measurements.

The approach taken in this work will be entirely different from that taken in [ZAJ84, Cha91]. The correlation data will not be corrected for the nuclear Coulomb effects. Instead, Coulomb effects will be added to a model in Chapter 6, and the influence of the nuclear Coulomb effects on the model predictions will be explored. This approach avoids the two main problems with the previously discussed approach – the source geometry is exactly known from the model and the many-body Coulomb interactions can be ignored in the model calculations.

2.5 Parameterization of the Correlation Function

The correlation function $C_2(\vec{p}_1, \vec{p}_2)$ for identical particles is in reality a function of six momentum components. This parameterization, although completely general, is cumbersome. As mention earlier, for a dynamical system the correlation function can be written more intuitively in terms of the momentum difference and the average momentum of the pair:

$$C_2(\vec{p}_1, \vec{p}_2) \simeq C_2(\vec{Q}, \vec{K}), \tag{2.27}$$

where $Q_i(\vec{p}_1, \vec{p}_2)$ are the momentum differences defined in some reference frame and $K_i(\vec{p}_1, \vec{p}_2)$ are the average momenta of the pair.

At some point it is necessary to choose a coordinate system and reference frame. This choice is based largely on the information that one wishes to extract from the correlation measurement. Pragmatically, the choice of a coordinate system is also based on the capabilities of the detector and the statistics available.

2.5.1 One-Dimensional Parameterization

A convenient way of avoiding the choice of a coordinate system or reference frame is to paramterize $C_2(\vec{Q}, \vec{K})$ is terms of quantities that are invariant under Lorentz transformations. For two particles, there are two Lorentz invariant quantities. One is the invariant mass of the two particles and the other is the invariant momentum difference

$$Q_{inv} = \sqrt{|\vec{Q}|^2 - Q_0^2}, \tag{2.28}$$

where $Q_0 = E_1 - E_2$. In the rest frame of the pair, $Q_{inv} = |\vec{Q}|$. The one-dimensional gaussian parameterization of the identical boson correlation function is:

$$C_2(Q_{inv}, \vec{K}) = 1 + \lambda e^{-Q_{inv}^2 R_{inv}^2(\vec{K})}, \tag{2.29}$$

where $R_{inv}(\vec{K})$ is the invariant radius parameter and λ is intercept of the correlation functions as $Q_{inv} \to 0$. The λ parameter should be unity for a completely incoherent source where no pions come from long-lived resonance decays. In principle, the λ parameter is also a function of $\vec{K}$.

This parameterization is useful for two reasons. First, for poor statistics a 1-dimensional parameterization is often the only parameterization that will allow the fits to converge. In addition, the fact that Q_{inv} is a relativistic invariant means that the invariant radius does not depend on the choice of coordinate system and can be used to compare the results of different experiments that may choose to evaluate their three-dimensional correlation functions in different coordinate systems and reference frames. The drawback of the parameterization in terms of Q_{inv} is that the measured radius parameter $R_{inv}(\vec{K})$ has no intuitive physical meaning in terms of a length in a fixed reference frame.

2.5.2 Three-Dimensional Parameterization

When sufficient statistics are available a 3-dimensional parameterization allows a larger amount of information to be extracted than a 1-dimensional parameterization. In this case, it is necessary to choose a coordinate system and reference frame. This choice is largely motivated by the physics goal of the measurement.

The most common 3-dimensional parameterization is the so called Bertsch-Pratt parameterization [BGT88, Pra86]. The momentum difference vector $\vec{Q}$ is decomposed into a "longitudinal" direction along the beam axis (Q_L) and a direction transverse to

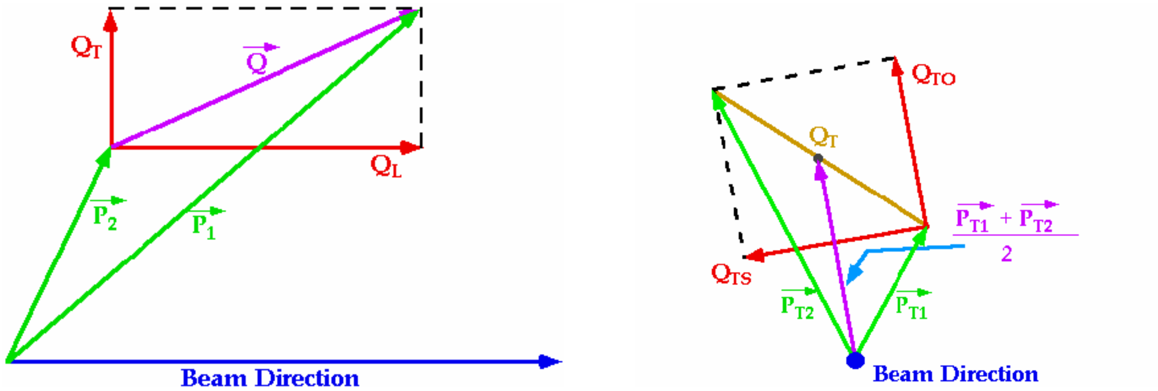

Figure 2.2: The Bertsch-Pratt coordinate system used for 3-dimensional HBT analysis.

the beam axis (Q_T). The transverse momentum difference is further decomposed into a "sideward" and "outward" direction. The "outward" momentum difference (Q_{TO}) is defined as the component of the transverse momentum difference parallel to the total transverse momentum of the pair. The "sideward" momentum difference (Q_{TS}) is defined as the component of the transverse momentum perpendicular to the total transverse momentum of the pair. The Bertsch-Pratt coordinate system is shown in Figure 2.2.

In this coordinate system, the 3-dimensional gaussian parameterization of the correlation function becomes

$$C_2(\vec{Q}, \vec{K}) = 1 + \lambda e^{-Q_{TO}^2 R_{TO}^2(\vec{K}) - Q_{TS}^2 R_{TS}^2(\vec{K}) - Q_L^2 R_L^2(\vec{K})}, \tag{2.30}$$

here $R_L(\vec{K})$ is the "longitudinal" radius parameter, $R_{TO}(\vec{K})$ is the "outward" radius parameter, and $R_{TS}(\vec{K})$ is the "sideward" radius parameter. Note that each of these radius parameters is in principle a function of the average momentum of the pair.

In certain cases, this parameterization allows for the measurement of the longitudinal size of the system, the transverse size of the system, and the duration of particle emission. The sideward radius (R_{TS}) is thought to measure the transverse size of the system directly. The outward radius (R_{TO}), however, couples the transverse radius with the lifetime of the source. This is shown in Figure 2.3. If the particles are emitted over a long period from a static source, it is expected that $R_{TO} \gg R_{TS}$.

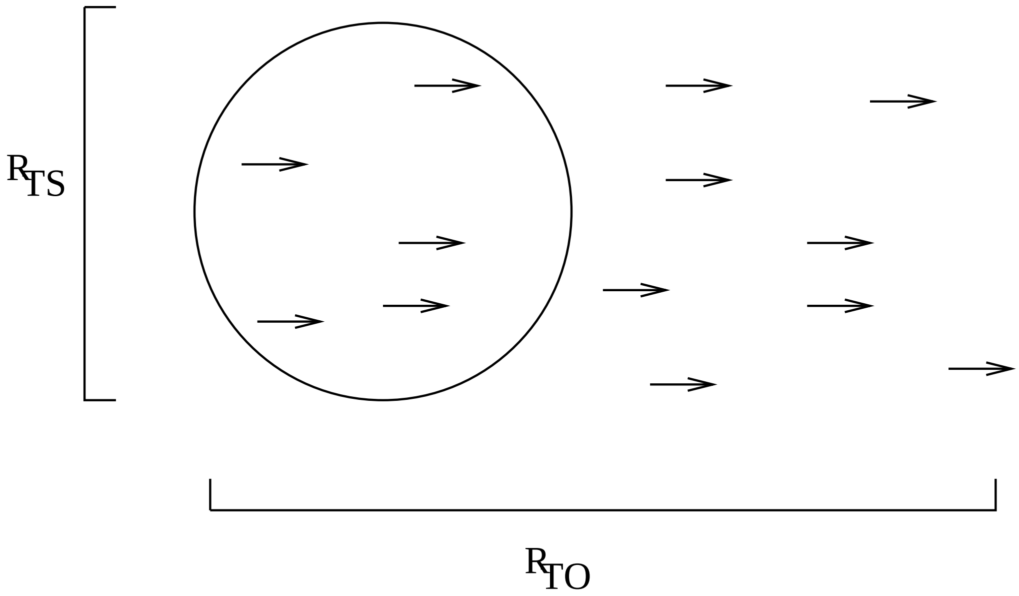

Figure 2.3: The simple picture of the outward and sideward radii. A source (circle) radiates particles over a long period, and these particles travel to the detector (to the right).

For a first order phase transition from the Quark-Gluon Plasma state it is expected that the QGP state will be long-lived. This can be explained in terms of simple entropy arguments. In the QGP state, the relevant degrees of freedom are quarks and gluons. Hence, the number of fermionic degrees of freedom (neglecting strange particles) is 4 quarks $(u, \bar{u}, d, \bar{d})$ with 3 colors and 2 spin states. This gives a total of 24 fermionic degrees of freedom. The number of bosonic degrees of freedom is 16 (8 gluons with 2 spin states[1]). A pion gas, on the other hand, has only 3 degrees of freedom corresponding to the three pion states. This large discrepancy in the number of degrees of freedom means that the QGP state hadronizes very slowly. This leads to a long duration of particle emission which can perhaps be measured via HBT.

2.6 Analytic Expressions for HBT Radii

It has been argued that the measured HBT radius parameters are somehow related to the longitudinal and transverse size of the system, the duration of particle emission, and the expansion dynamics of the system. These quantities, however, cannot be extracted directly from the data. Instead, it is necessary to assume some model and extract the physics information within the context of that model.

Under a certain set of theoretical approximations, the two boson-correlation function can be written as [Pra84]

$$C_2(\vec{Q}, \vec{K}) \simeq 1 + \frac{\int d^4x d^4x' S(x, \vec{K}) S(x', \vec{K}) exp[iQ \cdot (x - x')]}{\int d^4x d^4x' S(x, \vec{K}) S(x', \vec{K})}, \tag{2.31}$$

[1]Although the gluon is spin 1, it is massless and only two of the three spin states are allowed.

where $S(x, \vec{K})$ is the phase space density function of the emitting source. One of the approximations made in equation (2.31) is that $S(x, \vec{p})$, where $\vec{p}$ is the single particle momentum, can be replaced by $S(x, \vec{K})$, where$\vec{K}$ is the average pair momentum. This approximation is only true when the spread in the momentum distribution of $S(x, p)$ is much larger than R^{-1} [Pra84]. For a relativistic heavy-ion collision with characteristic size 10 fm, this requires that the spread of the momentum distribution is much greater than 20 MeV, and this condition is easily satisfied. This expression is usually written in the more compact form [CSH95]

$$C_2(\vec{Q}, \vec{K}) \simeq 1 + \frac{|\int d^4x S(x, \vec{K}) exp[iQ \cdot x]|^2}{|\int d^4x S(x, \vec{K})|^2}. \tag{2.32}$$

Equations (2.31) or (2.32) can then be used with a theoretically assumed emission function $S(x, \vec{K})$ to predict the HBT radius parameters.

Theoretically, the HBT radius parameters can be defined in terms of the curvature of the correlation function in the limit $\vec{Q} \to 0$, where the curvature $I(\vec{Q}, \vec{K})$ is defined by [Pra84]

$$C_2(\vec{Q}, \vec{K}) = 2 - \frac{1}{2} I(\vec{Q}, \vec{K}) |\vec{Q}|^2 \tag{2.33}$$

It was noted that for a gaussian source $S(x, \vec{K}) = \delta(t) exp[-r^2/R^2]$ the curvature is R^2. This definition of the radius parameters in not useful experimentally since the lowest Q bins are the most poorly measured. Since the experimental radius parameters are taken from a fit the the entire correlation function, the experimental radius parameters are only weakly influenced by the shape of the correlation function as $\vec{Q} \to 0$. If the correlation function is roughly gaussian, however, then the definition of the radius parameters as the curvature of the correlation function as $\vec{Q} \rightarrow 0$ should be approximately equal to the gaussian fit of the entire correlation function.

2.6.1 Lengths of Homogeneity

HBT radius parameters do not measure the physical dimensions of the system in all cases – instead the radius parameters represent lengths of homogeneity [AS95]. The length of homogeneity is the length scale over which pairs of particles of an average momentum K are emitted.

The physical meaning of the length of homogeneity can be seen by expanding equation (2.32) [CNH95, CSH95]. To do this, a quadratic saddle point approximation is used where the saddle point $\bar{x}_\mu(\vec{K})$ is defined by

$$\frac{\partial}{\partial x_\mu} lnS(x,K)|_{\bar{x}_\mu} = 0. \tag{2.34}$$

Physically, the saddle point is the position of maximum probability for emitting a single particle of momentum K. Using this, the phase space density function can be approximated as

$$S(x,K) \simeq S(\bar{x},K)exp[-\frac{1}{2}(x-\bar{x})^\mu (x-\bar{x})^\nu B_{\mu\nu}(\vec{K})], \tag{2.35}$$

where μ, ν are the indices of a space-time four vector and

$$B_{\mu\nu}(\vec{K}) = -\partial_\mu \partial_\nu ln\, S(x,K)|_{\bar{x}_\mu} \tag{2.36}$$

is the symmetric curvature tensor. The inverse of this curvature tensor is

$$(B^{-1})_{\mu\nu}(\vec{K}) = \langle x_\mu x_\nu \rangle - \langle x_\mu \rangle \langle x_\nu \rangle, \tag{2.37}$$

where $\langle f(x) \rangle$ is the average value of the function $f(x)$ with respect to the distribution $S(x, K)$. If equation (2.32) is expanded using the saddle point aprroximation given in equation (2.35) the correlation function can be expressed in term of the inverse of the curvature tensor:

$$C_2(\vec{Q}, \vec{K}) = 1 + e^{-Q^\mu Q^\nu B^{-1}_{\mu\nu}(\vec{K})}. \tag{2.38}$$

This is the most general gaussian parameterization of the correlation function.

Alternatively, consider the following approximation valid for pairs with $|\vec{Q}| \ll E_K$:

$$Q \cdot x \simeq (\beta_T Q_{TO} + \beta_L Q_L)t - Q_{TO}x - Q_{TS}y - Q_L z, \tag{2.39}$$

where β_T is the transverse velocity of the pair and β_L is the longitudinal velocity of the pair. This suggests the following transformation:

$$x \rightarrow x - \beta_T t \tag{2.40}$$

$$z \rightarrow z - \beta_L t. \tag{2.41}$$

Using these transformations and equating equation (2.30) with equation (2.38) the following expressions are derived for the HBT radii:

$$R^2_{TS}(\vec{K}) = \langle y^2 \rangle - \langle y \rangle^2 \tag{2.42}$$

$$R^2_{TO}(\vec{K}) = \langle (x - \beta_T t)^2 \rangle - \langle (x - \beta_T t) \rangle^2 \tag{2.43}$$

$$R^2_L(\vec{K}) = \langle (z - \beta_L t)^2 \rangle - \langle (z - \beta_L t) \rangle^2. \tag{2.44}$$

Here the HBT radii are expressed in terms of variances around the saddle point of the emission function. These are mathematical expressions for the lengths of homogeneity.

It was shown [CSH95] that the 3-dimensional parameterization (equation (2.30)) is not the most general. It is also necessary to include one of the cross-terms allowed by equation (2.38):

$$C_2(\vec{Q},\vec{K}) = 1 + \lambda e^{-Q_{TO}^2 R_{TO}^2(\vec{K}) - Q_{TS}^2 R_{TS}^2(\vec{K}) - Q_L^2 R_L^2(\vec{K}) - 2R_{OL}^2(\vec{K}) Q_{TO} Q_L}, \tag{2.45}$$

where $R_{OL}^2(\vec{K})$ can be positive or negative. It can be expressed in terms of variances as

$$R_{OL}(\vec{K})^2 = \langle (x - \beta_T t)(z - \beta_L t) \rangle - \langle (x - \beta_T t) \rangle \langle (z - \beta_L t) \rangle. \tag{2.46}$$

This "out-longitudinal" cross term measures the $x - z$, $x - t$ and $z - t$ correlations of the source. In principle, there are also other crossterms (R_{SL}^2 and R_{OS}^2), but these vanish for azimuthally symmetric sources [CNH95].

2.7 LCMS Reference Frame

Although somewhat model-independent expressions have now been developed that express the correlation radii in terms of lengths of homogeneity, these lengths are of course reference frame dependent. In the present work, the 3-dimensional correlation functions will be evaluated in the "longitudinally co-moving system" (LCMS). This is defined as the frame where $p_{z_1} + p_{z_2} = 0$ [PCZ90]. This means that the reference frame is different for each pair. The advantage of this frame is that the outward direction corresponds to the direction coming straight from the source in the rest frame of the source. Hence, the duration of particle emission, extracted by comparing R_{TO} and R_{TS}, is most directly measured in this frame.

CHAPTER 3

EXPERIMENT NA44

NA44 is a second generation heavy-ion experiment at the CERN Super Proton Synchrotron (SPS). Originally designed in 1989 for the 200 GeV/nucleon ^{32}S beam, the experiment underwent a major upgrade in 1994 in order to handle the increased particle multiplicities in 158 GeV/nucleon ^{208}Pb ion induced collisions. The experiment took data using the Pb beam from 1994-1996.

NA44 resided in the North Experimental Hall in Prevessin, France. The high intensity H4 beamline was used. For Pb ion running, the maximum beam intensity was 6×10^6 Pb ions per 2 second spill, although lower beam intensities were normally used except in the case of rare triggers. For the pion data presented here, the nominal beam intensity was 3×10^6 Pb ions per spill.

NA44 is a focussing spectrometer designed to measure mid-rapidity single-particle spectra and yields as well as two-particle correlations. The experiment is shown in Figure 3.1. Because of its small acceptance, the multiplicities in the detector are very low, typically averaging 1-2 particles per event. The low multiplicities within the detector allow for excellent track by track particle identification (PID) through time-of-flight and Cerenkov measurements. Tracking is done via three highly segmented hodoscopes and three multi-wire proportional chambers.

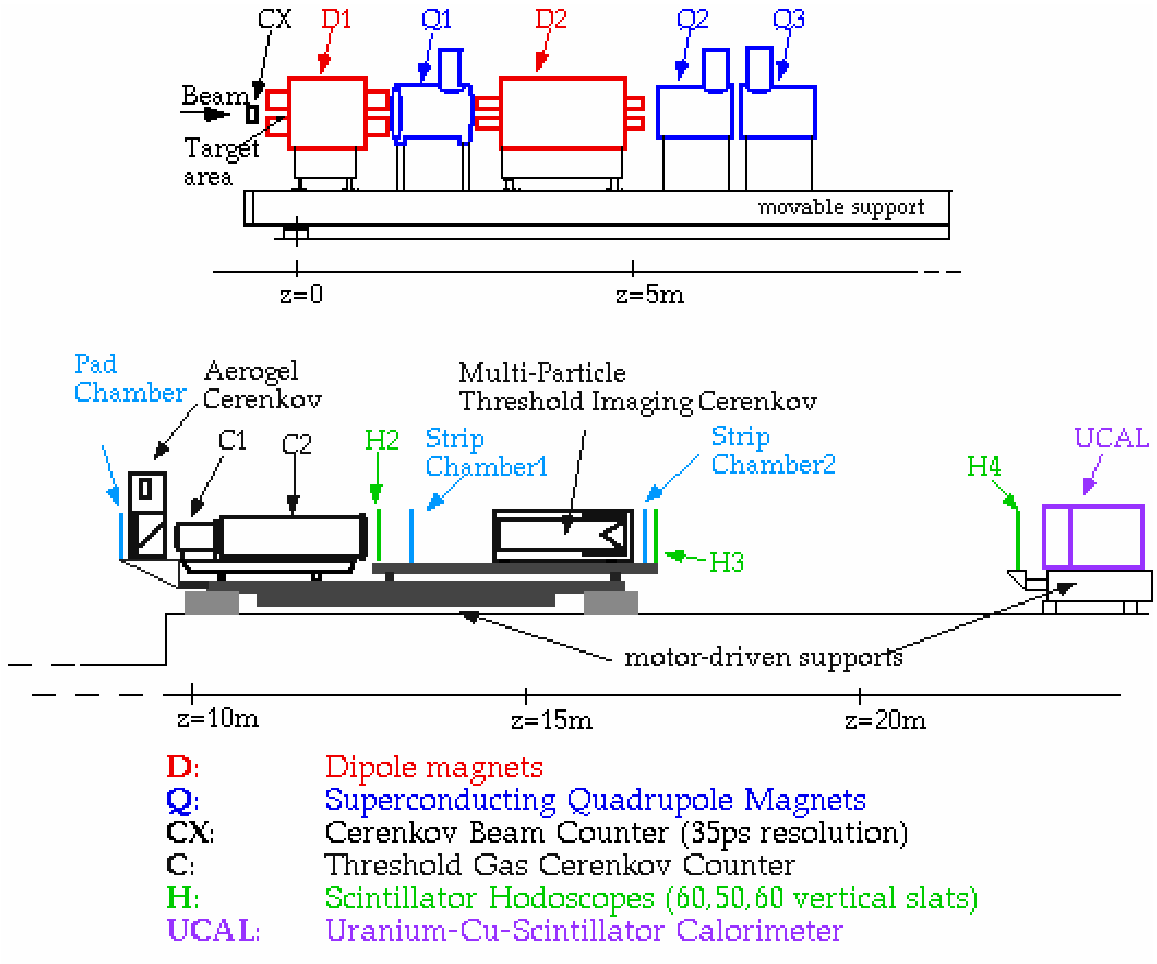

Figure 3.1: Experiment NA44 in 1995 and 1996.

3.1 The Target Area

Incoming beam particles are identified through a Cerenkov beam counter [MAE94]. This device consists of two small Cerenkov radiators with a single phototube attached to each. By comparing the TDC signals from each beam counter, it is possible to estimate the timing resolution ($\sigma \approx 35$ ps.). In addition, the ADC signals from the beam counter are used to eliminate events in which two beam particles strike the target within the timing gate of the experiment. The ADC signal from the beam counter, and the associated double beam cut is shown in Figure 3.2. In order to ensure that the beam particle strikes the target, two scintillators (CXVLA and CXVRA) are located around the beam line. Events are rejected if there is a large signal in either detector.

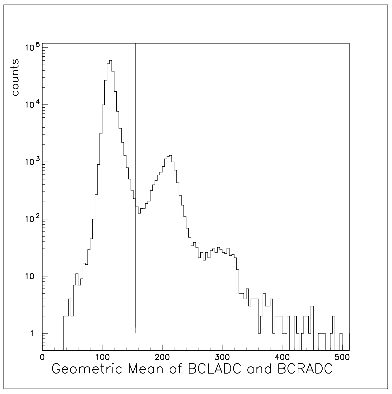

Figure 3.2: ADC signal from beam counter. The line indicates the cut used to remove events where more than one beam particle was present.

After beam counter there is a target. For each data set, a target was chosen to maximize the data taking rate while minimizing the multiple scattering.

After the target, there are two centrality detectors. T0 consists of two thin, parallel pieces of scintillator that cover the pseudo-rapidity window $1.3 \leq \eta \leq 3.5$. Each scintillator is attached to two phototubes. Particles in the NA44 acceptance pass between the two pieces of scintillator, but other produced particles pass through the scintillators. The ADC signal from the phototubes can be used to measure the centrality. In addition, T0 is used as the centrality trigger. The rough centrality of the trigger is determined by,

$$\text{centrality} \approx \frac{\text{T0 count rate}}{\text{beam counter rate} \times \text{target interaction length}}. \tag{3.1}$$

The signal from T0, however, does not come entirely from particles originating in the collision. There is a large background from delta electrons produced as the beam particle passes through the target. Since T0 sits within the first dipole magnet, however, the delta electron are swept to one side of T0.

In addition to T0, there is a highly segmented silicon pad multiplicity detector. This is not used in the trigger, but can be used off-line as an independent centrality measurement. The silicon pad detector consists has 512 pads, covers a pseudo-rapidity range $1 \leq \eta \leq 4$, and has full azimuthal symmetry. In nearly central Pb+Pb collisions, the mean occupancy per pad is close to 1, so the total number of pads hit is not a good indicator of centrality. Instead, the sum of the calibrated ADC signals in each pad is used.

3.2 The Magnets

The NA44 magnet section consists of two dipole and three superconducting quadrupole magnets arranged as shown in Figure 3.1. All of the magnets are mounted on a rotating platform so that different ranges in transverse momentum (p_t) can be explored. Data are typically taken at two angular settings: 44mr (2°) and 131mr (7°). The dipole magnetic fields are adjusted to select particles with nominal momenta of 4 GeV/c, 6 GeV/c, or 8 GeV/c. The range in momenta around the nominal setting is roughly 20%.

The superconducting quadrupoles are used to maximize the acceptance in the various components of the momentum difference $\vec{Q}$ for HBT studies. A normal spectrometer without quadrupole magnets does not have a large acceptance for the momentum difference in the direction perpendicular to the total momentum of the pair. This limits the ability to do three dimensional HBT measurements. The use of superconducting quadrupoles, however, allows NA44 to measure all three components of the momentum difference.

Two quadrupole settings are used: horizontal and vertical. The horizontal setting maximizes the acceptance in Q_{TO} and Q_L, while the vertical setting maximizes the acceptance in Q_{TS} and Q_{TO}. Since the momentum resolution of the horizontal setting is slightly better than that of the vertical setting, the horizontal setting is used when measuring single particle yields and spectra. The p_t versus rapidity acceptances for pions from the 4 GeV horizontal and vertical settings are shown in Figure 3.3. The acceptances for the various components of the momentum difference are shown in Figures 3.4 and 3.5.

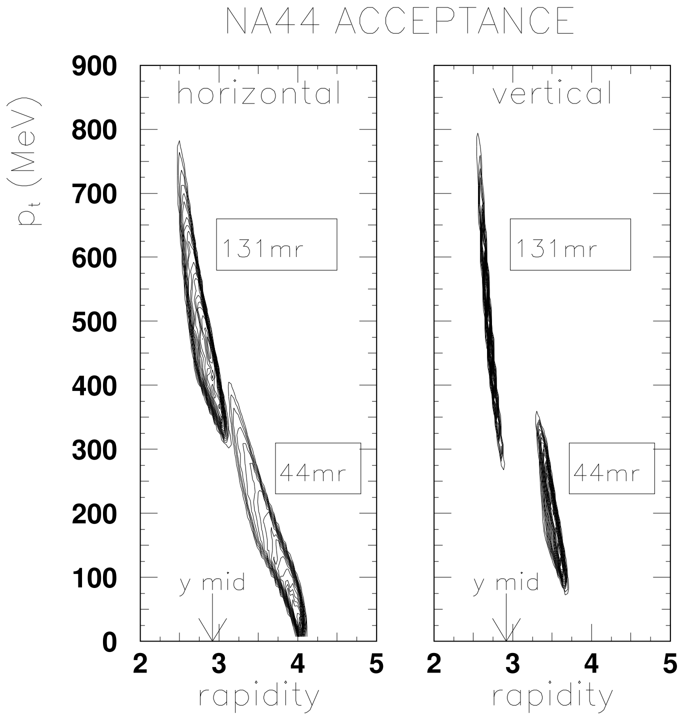

Figure 3.3: NA44 acceptance for low and high angle 4 GeV/c pions.

3.3 The Detectors

After the magnets, particles are tracked and identified. Particles are identified using two threshold Cerenkov counters, a Threshold-Imaging Cerenkov (TIC) and three

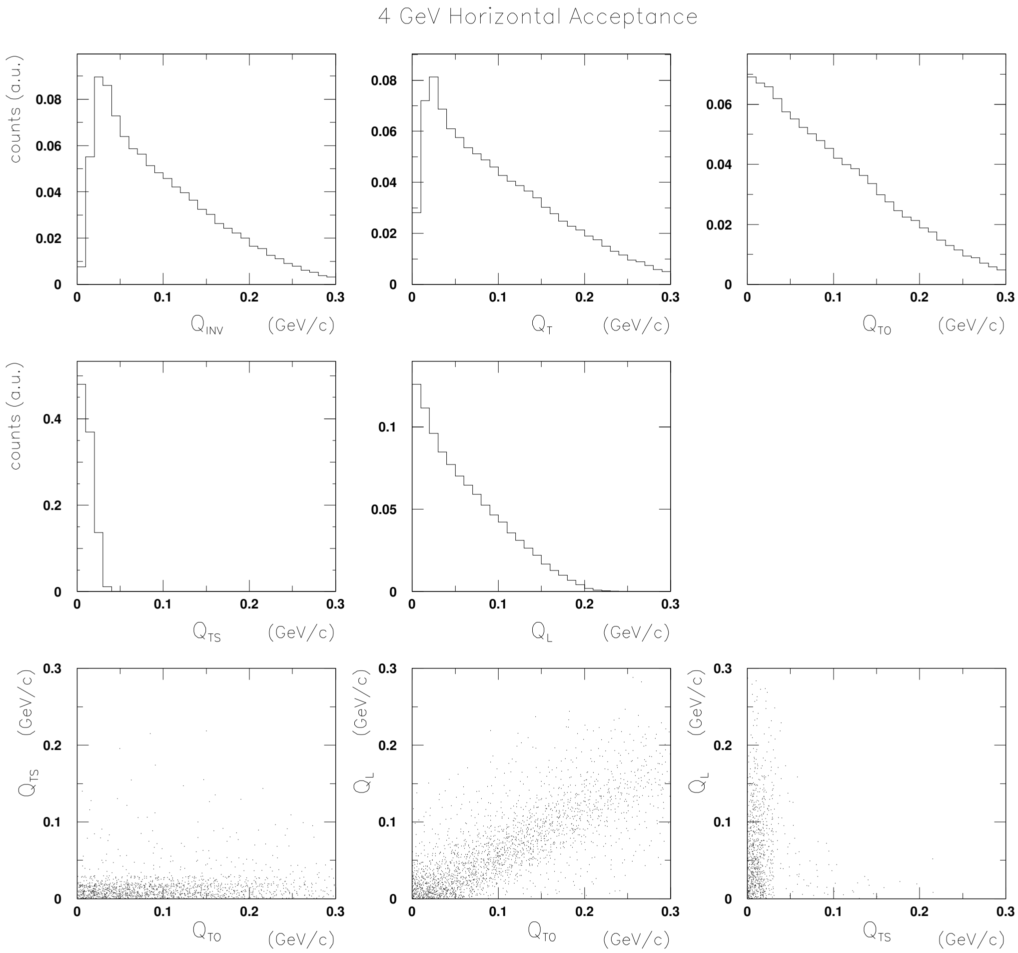

Figure 3.4: NA44 acceptance for 44mr horizontal pions.

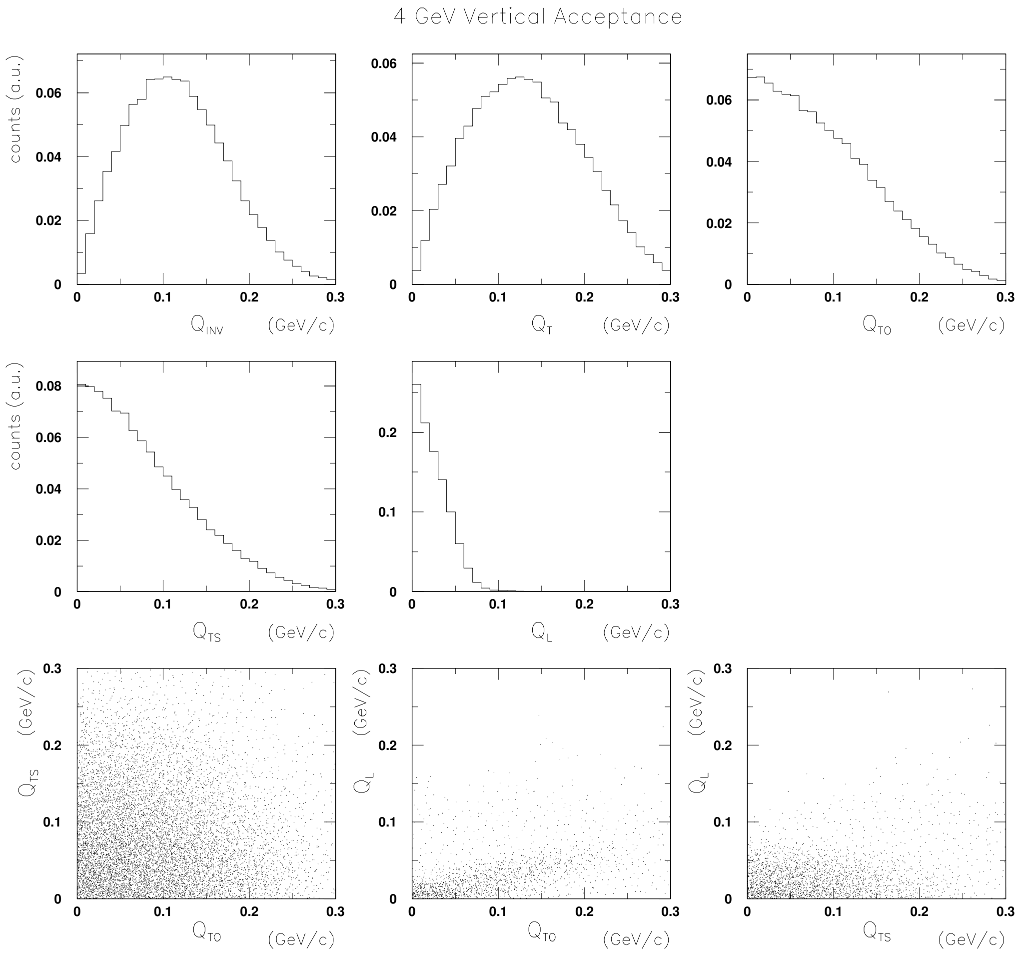

Figure 3.5: NA44 acceptance for 44mr vertical pions.

time-of-flight (TOF) hodoscopes (H2, H3, and H4). In addition to the TOF information, the hodoscopes provide position information about the track. Additional position information is provided by three multi-wire proportional chambers (the Pad Chamber, Strip Chamber 1 and Strip Chamber 2). The position information from the hodoscopes and multi-wire proportional chambers is used to reconstruct the straight-line trajectories of each track. The trajectory of the track is then converted into a momentum vector using a set of momentum coefficients calculated from the Monte-Carlo (MC). These coefficients parameterized the momentum in terms of the position of the track at the Pad Chamber and H2.

3.3.1 The Hodoscopes

NA44 uses three highly segmented scintillating TOF hodoscopes to get position and time-of-flight information for each track. H2 is located 13.9 m downstream of the target and consists of 60 vertically aligned plastic scintillating slats with dimension $6 \times 6 \times 200$ mm (width $\times$ thickness $\times$ length). H3 is located 18.4 m downstream of the target and has 50 slats of dimension $13 \times 10 \times 220$ mm. H4 is located 24.7 m from the target and has 60 slats with dimension $23 \times 20 \times 700$ mm. H2 and H3 are aligned perpendicular to the optical axis of the experiment, while H4 sits at a small angle which depends on the spectrometer setting.

A photomultiplier tube is attached at the top and bottom of each slat. The y-position of a hit on a slat is determined by the time difference between the signals at the top and bottom phototubes. The y-resolution is estimated to be 0.9 cm for

H2, 0.7 cm for H3 and 1.3 cm for H4. The x-position is determined by which slat is hit, so the x-position resolutions are of the same order as the slat widths. The TOF resolution for each of the hodoscopes is around σ =100 ps.

Since the signals from the hodoscopes come very fast, the TDC signals from the hodoscopes are used to trigger on events that may contain tracks. The "pairs" trigger requires two valid TDC signals from both H2 and H3.

3.3.2 Multi-wire Proportional Chambers

In order to improve the momentum resolution, three multi-wire proportional chambers were installed during the upgrade for the Pb beam. The Pad Chamber (PC) is located 9.5m downstream from the target. It uses a pad readout which allows for a simultaneous measurement of the x and y positions of a hit. The vertical and horizontal position resolutions of this detector are 0.27 cm and 0.43 cm, respectively. Because of its excellent position resolution and location closest to the target, the raw position at the pad chamber is used directly in the momentum calculation.

Two additional multi-wire proportional chambers are located directly after H2 (SC1) and before H3 (SC2). SC1 is located 14.4 m downstream of the target and SC2 is located 17.9 m downstream of the target. Each uses a strip readout, with one set of horizontal strips and one set of vertical strips. This readout method means that the x and y positions of a track passing through one of the strip chambers are measured independently. Each detector is treated as two detectors in the reconstruction with the vertical strips giving a list of x-positions and the horizontal strips giving a list of

y-positions. The position resolution of SC1 (SC2) in x and y are 0.12 cm (0.14 cm) and 0.11 cm (0.23 cm), respectively.

One area of great concern in HBT studies is the ability to resolve close by tracks. The two-hit resolution of the pad chamber is approximately 0.5 cm, so a cut is applied in the data analysis on tracks that have separations less than 0.5 cm. The strip chambers have a similar two-hit resolution in each direction.

3.3.3 Threshold Cerenkov Counters

NA44 uses two threshold Cerenkov counters in order to trigger on events with particles of a given species. These detectors sit between the pad chamber and H2 and are named C1 and C2. Both detectors have high and low pressure settings. Changing the pressure changes the index of refraction and thus changes the threshold for production of Cerenkov light.

Each Cerenkov can be used in the trigger in either veto, ignore or require mode. C2 is used primarily to reject events with electrons and is used in veto mode while taking pion pairs. C1 is used to identify events with pions. For pion pairs, the trigger is set in "C1 ignore" mode. Off-line the signal in C1 is used to ensure that at least two pions are in the spectrometer.

3.3.4 Threshold Imaging Cerenkov

In order to enhance NA44's particle identification capabilities in the higher multiplicity Pb beam events, a Threshold Imaging Cerenkov (TIC) was constructed in 1994 [FAB95]. The TIC helps to separate pions from heavier particles on a track by track basis using Cerenkov light. The principle of operation is shown in Figure 3.6. Pions that enter the TIC pass through a radiator gas and produce a forward cone of Cerenkov photons. These photons are then reflected by two mirrors towards CsI based multi-wire proportional chamber photon detectors. Heavier particles do not produce Cerenkov light. In the analysis, track are reconstructed through the TIC and the number of hit pads in the MWPC are counted in a small fiducial area around the track. If there are more than 2 hits pads in the fiducial area, the particle is assumed to be a pion and a looser mass-squared cut can be used. The TIC is especially useful for eliminating kaons from the pion sample since the mass-squared distributions for kaons and pions are not distinct. In Figure 3.7, the number of TIC pads hit is plotted against the mass-squared measured at hodoscope 3 for an ideal run. The pions are clearly separated from the kaons and protons. It should be noted that the TIC performance varied somewhat due to transperency problems in the radiator gas. For the data presented in this thesis, the mean number of TIC pads hit for a pion was lower than for the data shown in Figure 3.7. Hence, the pion identification is not as good as Figure 3.7 would suggest.

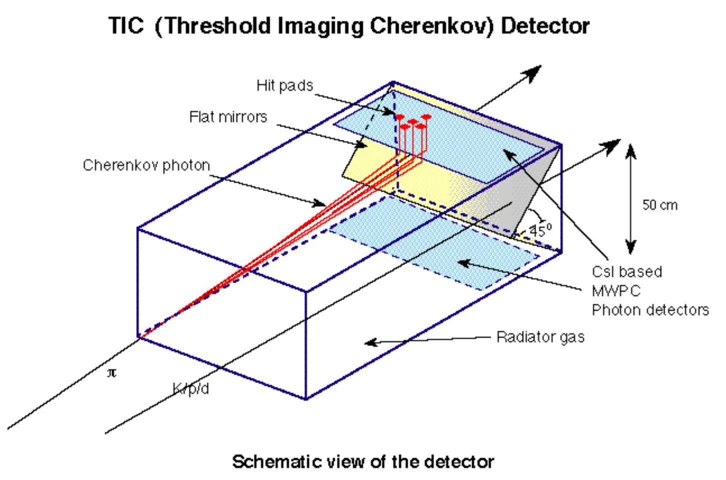

Figure 3.6: The NA44 Threshold Imaging Cerenkov.

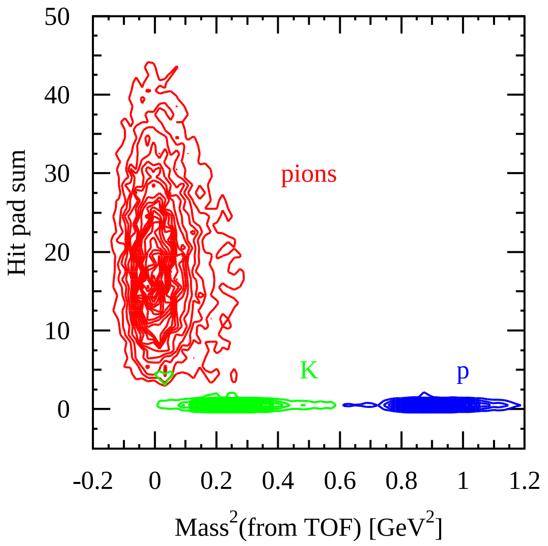

Figure 3.7: The number of hit TIC pads versus the mass-squared at Hodoscope 3 for an ideal run.

3.3.5 Other Detectors

NA44 was equipped with two additional detectors that were not used in this analysis. A Uranium Calorimeter (UCAL) is located after H4, 24.9 m downstream of the target. This detector is used primarily to identify electrons and muons for the single particle analyses. An Aerogel Cerenkov counter is located between the pad chamber and C1, 10.1 m downstream of the target. Aerogel has a higher index of refraction than gas, so this detector was designed to detect kaons and be used as a kaon trigger. The detector, however, never reached design specifications and served primarily as a source of multiple scattering.

3.4 NA44 Monte-Carlo

In order to correct the data for the experimental momentum resolution and detector acceptance, a Monte-Carlo (MC) is used as an integral part of the data analysis for both the single particle and HBT measurements. Being a simple experiment, NA44 employs a simpler and faster simulation package (DECAY TURTLE [BRO74]) than most experiments. This simulation package is based on TRANSPORT [BRO80]. The speed of the NA44 MC allow for high statistics MC simulations which are then used to correct the data.

In TRANSPORT, propagation of a particle through the NA44 magnets is treated as simple matrix multiplication. The field maps for the dipoles and quadrupoles are used by TRANSPORT to create transfer matrices. A track is propagated by matrix multiplication through the transfer matrices, a process called ray tracing. The effects of multiple scattering and particle decay are simulated in the DECAY TURTLE package.

The DECAY TURTLE package is used in the NA44 Monte-Carlo to propagate tracks, but the detector simulations are not incorporated into this package. For each detector, the (x, y, z) and (p_x, p_y, p_z) given from TURTLE are used to simulate the detector response using NA44 detector simulation routines. The dE/dx of the track is calculated for each detector, and this information is used to simulate the ADC response of each detector. The TDC response of each detector is also simulated, but it is not used in the analysis of the MC data. The results of these detector simulations are then treated like real data and run through the standard NA44 reconstruction routines. By comparing the input to the MC and the output from the reconstruction, it is possible to evaluate and correct for the distortion of the physics signal due to detector efficiencies and resolutions.

As input to the MC simulation, NA44 typically samples from a simple thermal parameterization

$$\frac{1}{m_t^2}\frac{d^2N}{dy\;dm_t} = e^{(-m_t/T)}e^{((y-y_0)^2/\sigma^2)} \tag{3.2}$$

where $m_t = \sqrt{m^2 + p_t^2}$ is the transverse mass, y is the rapidity, y_0 is mid-rapidity, T is the slope parameter, and σ is the rapidity width. T and σ are either taken from data when available, or tuned so that the distributions in the MC match the distributions in the real data. Figure 3.8 shows a comparison of the MC data and real data for a typical setting. The agreement between MC and data is very good. The discrepancy in p_z is due to the fact that the data were taken with a veto on C2, and the pion threshold for Cerenkov light production in C2 is 5.2 GeV. This trigger effect is not simulated in the MC. The excellent agreement in the confidence level distributions should be emphasized since it shows that the amount of multiple scattering in the MC closely approximates the real experiment.

The MC can also be used to estimate the momentum resolution of the spectrometer. This is done by subtracting the simulated momenta from the reconstructed momenta, forming a histogram of the results, and fitting the histogram to a gaussian. The momentum difference resolutions for the 4 GeV/c 44mr and 131mr horizontal and vertical settings are listed in Table 3.1. The momentum difference resolution is clearly better for the horizontal setting.

	44mr hor	44mr ver	131mr hor	131mr ver
$\sigma(\Delta Q_{inv})$	11.6	16.3	10.8	16.4
$\sigma(\Delta Q_{TO})$	12.8	17.3	11.8	23.4
$\sigma(\Delta Q_{TS})$	7.8	17.4	7.3	17.8
$\sigma(\Delta Q_L)$	8.3	8.3	11.0	10.8

Table 3.1: The estimated momentum difference resolution (in MeV/c) for Q_{inv}, Q_{TO}, Q_{TS}, and Q_L for the 44mr and 131mr 4 GeV/c horizontal and vertical settings. The Pb target thickness is 2.27 gm/cm^2 except for the 131mr horizontal setting where a 1.14 gm/cm^2 Pb target is assumed. The Q_L resolution is evaluated in the LCMS frame.

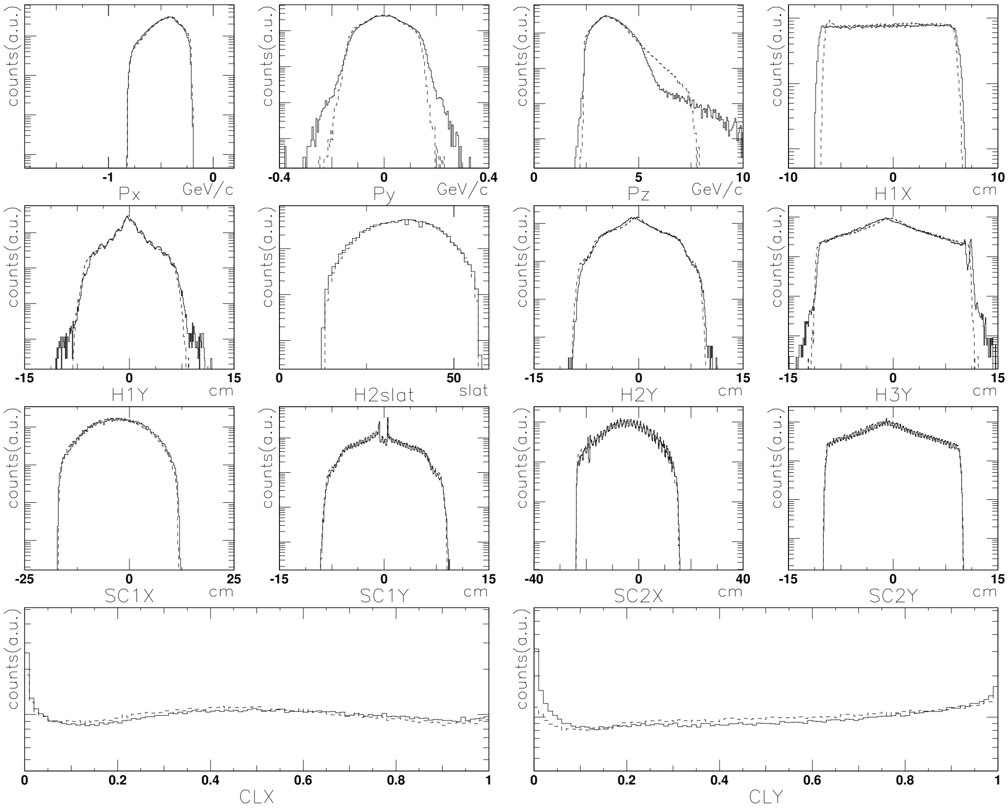

Figure 3.8: A comparison of data and MC for the 131mr vertical setting. The solid lines are data and dashed lines are MC. Clx and Cly are the confidence levels in x and y for the reconstructed tracks.

CHAPTER 4

DATA ANALYSIS

This chapter will explain the techniques by which several million physics events taken by NA44 are reduced to a few thousand data points and then further reduced to a few fit parameters. The path to the final physics result has several stages. First, the data are taken by the experiment. Next, the detectors are calibrated. After this, the data are passed through a reconstruction program. The output of this reconstruction program is then filtered such that only the information useful for the HBT analysis are kept. The reduced data are then passed through an HBT program which forms the correlation function. The correlation function is then fit and characterized by a few fit parameters.

4.1 The Data

The analyses described here will be the low-p_T $\pi^-\pi^-$ and high-p_T $\pi^+\pi^+$ correlation measurements. When the results are presented, these data will be compared to low-p_T $\pi^+\pi^+$ data that were analyzed by John Sullivan at Los Alamos. The data analysis techniques for all three data sets are essentially the same.

The 44mr $\pi^-\pi^-$ data were taken during the 1995 Pb run. Since pions are copiously produced, this data set was taken in a period of less than 24 hours. 16 runs were taken in the 4 GeV/c horizontal setting (runs 3909-3924) and 24 runs were taken in the 4 GeV vertical setting (runs 3931-3956), where each run contains about 35K events. A Pb target of thickness 2.27 gm/cm^2 was used, corresponding to roughly 4.2% of an interaction length for a Pb projectile. The centrality of the trigger was $\sigma_{trig}/\sigma_{geom} = 19 \pm 1\%$.

The 131mr 4 GeV/c $\pi^+\pi^+$ horizontal data were taken during the 1994 Pb run (runs 3069-3084, 3105-3118, 3131-3139) using a Pb target of thickness 1.15 gm/cm^2 (2.1% of an interaction length). The centrality of the trigger was $\sigma_{trig}/\sigma_{geom} = 15 \pm 1\%$. A set of 131mr 4 GeV/c $\pi^+\pi^+$ vertical data was also taken in 1994, but the statistics proved insufficient. The 131mr $\pi^+\pi^+$ vertical measurement was repeated in 1995 (runs 3685-3718) using a target of thickness 2.27 gm/cm^2. The centrality of the trigger was $\sigma_{trig}/\sigma_{geom} = 19 \pm 1\%$. Since the 1995 vertical data sample is more than a factor of two larger than the 1994 vertical data sample, only the 1995 vertical data are used in the high-p_T $\pi^+\pi^+$ analysis presented here.

4.2 Hodoscope Calibrations

Several of the detectors used in experiment NA44 need to be calibrated in order to get optimum performance. In particular, the 3 hodoscopes and the CX counter need to be calibrated often in order to get the best position and TOF resolution possible. Fortunately, the physics data can be used to calibrate the detectors so dedicated calibration runs are unnecessary in most cases. These calibrations are typically performed either every 5-10 runs, when the trigger is changed, or when there is an extended break between runs. The calibration procedure is a five step process, and these 5 "passes" will now be described.

During pass 1, a rough calibration is performed for CX and the three hodoscopes. For each photomultiplier tube attached to CX or a hodoscope slat, the ADC pedestal (PED) is calculated during pass 1. This pedestal value is then subtracted from the total ADC value to get the true ADC value. During pass 1, a crude TOF offset (TOF) for each slat is also calculated. This offset is used to roughly align the peak of the TDC distribution for each slat at the origin.

In passes 2 and 3, slewing constants are calculated. The slewing constants are used to correct for the fact that the TOF response of the hodoscope slats are somewhat dependent on the amount of charge deposited in the slat. If a large amount of charge is deposited, the discriminator on the TDC tends to be satisfied at an earlier time leading to a faster time measurement. The corrected TDC_{corr} is parameterized in terms of the raw TDC_{raw} and the pedestal subtracted ADC by [Lee93]

$$TDC_{corr} = TDC_{raw} - SLW \times \frac{1}{\sqrt{ADC}}, \tag{4.1}$$

where $ADC = ADC_{raw} - PED$ and SLW is the slewing constant.

In pass 4, the final calibrations are done for each of the hodoscope slats and CX using the calibration constants calculated is passes 1-3. The calibration constants calculated in pass 4 are the least stable, so pass 4 is typically performed every 5 runs. The TOF distribution is calculated using the slewing constants from passes 2 and

3. This TOF distribution is then fit with a gaussian, and the gaussian is moved so that its peak is located at the origin. The amount by which the gaussian must be moved is the TOF offset constant (OST). In addition, the vertical position at which the top and bottom phototubes fire simultaneously is calculated (YOF). Finally, the gains of each phototube on the hodoscopes and CX are calculated (ADC). The ADC calibration constants are used to gain match the different hodoscope slats.

Pass 5 is a diagnostic pass used to check whether passes 1-4 have indeed worked correctly. This pass is performed for every run. After pass 5 has been completed and the results checked, the calibration constants calculated in passes 1-4 are inserted into the NA44 database for use by the reconstruction program.

4.3 Reconstruction and DST production

After the calibrations are completed, the DST (data summary tape) production and reconstruction can be performed. First the raw data are read in from the data tape. The raw data are then converted into a form that can be used by the reconstruction algorithm. The hodoscope and multi-wire proportional chamber information are converted into lists of valid hits. The valid hits are then used to find tracks, and the momenta of these tracks are calculated. Finally, the DST is produced in the form of an ntuple [BRU88].

The data written to tape are almost entirely in the form of scaler information, ADC values, and TDC values. The scaler information is used primarily in single particle analysis. The ADC and TDC information is used to identify and track particles. The hodoscope ADC and TDC information is used to produce a list of valid hits at each hodoscope with associated x-position, y-position, and TOF information. A minimum ADC threshold is required for a valid hodoscope hit in order to reduce noise and prevent ghost tracks.

The SC and PC ADC information has the pedestals subtracted at the hardware level. Valid hits are identified using a clustering and deconvolution algorithm [SPE94]. The ADC clusters are fit by a gaussian, and the center of the gaussian is used as the track position. For the pad chamber, a 2-dimensional gaussian is used to fit the clusters. For the strip chambers, however, a 1 dimensional gaussian is used. A major concern in HBT analysis is ghost hits which in turn lead to ghost tracks. In order to reduce ghost hits in the pad and strip chambers, a minimum ADC value is required for a valid cluster.

After the hodoscope and chamber ADC information has been converted into a list of valid hits, tracks are fit using a chi-squared technique. The resolutions assigned to each detector are determined from the data, and hence incorporate both the intrinsic position resolution of the detector and the multiple scattering contribution from material before the detector. Since H4 is very far from the target, the multiple scattering contribution to its position resolution is quite large, leading to a very poor position resolution. For this reason, H4 is not used in the track fitting procedure. Also note that the multiple scattering contribution depends on the momentum of the particle, so the resolutions assigned to each detector in the track fitting procedure depend on the momentum setting of the spectrometer. A valid track is required to have hits in the PC, H2, H3 and 3 of the 4 SC planes. A study was performed and it was shown that the HBT results are essentially the same if all 4 SC planes are required in the tracking [HAR97].

After the tracks have been fit, the momentum of each track is calculated. The momentum is parameterized in terms of the position of the track at the PC and H2. The coefficients used in the polynomial parameterization of the momentum in terms of the positions at the PC and H2 are calculated using the NA44 MC with multiple scattering turned off. In the momentum calculation, the raw position at the PC and fit position at H2 are used since it was found that this greatly improves the momentum resolution. The PC, being closest to the target, is least affected by multiple scattering.

When an event has been completely processed, it is written out to a DST file. This DST file contains all of the global event information and track-by-track information needed for the physics analyses.

4.4 Pair Files

Although the DST could in principle be used directly to produce the correlation functions, the data are further reduced so that only the data relevant to the HBT analysis remains. This condensed data file is know as a pair file. During the production of the pair file, cuts are applied so that the remaining data sample consists entirely of "golden" events. Events where two beam particles strike the target within the timing gate of the experiment are rejected by making an ADC cut on the Cerenkov Beam

Counter, and events from the beam halo are rejected by making an ADC cut on the CX veto detectors. Events with possible electron contamination are rejected by making a tight cut on the ADC value of C2, and events with at least 2 pions are selected by requiring a sufficient ADC signal in C1.

After the event cuts are performed, PID and track quality cuts are performed on the individual tracks. In order to reduce ghost tracks or tracks that may have experienced a nuclear interaction, tracks with very low confidence levels are rejected. Also, since the calibrations of hodoscope slats toward the edge of the spectrometer acceptance tend to be suspect due to low statistics, tracks that strike an outer hodoscope slat are rejected.

Finally, the tracks that are pions are identified. A loose cut on the H2 and H3 TOF is made. For final pion identification, the mass-squared at H3 (H3MSQ) is calculated using the H3 TOF and the calculated momentum of the track. Pions should have a mass-squared of 0.02 GeV^2, but due to the momentum and TOF resolution of the detectors the pion mass-squared peak has a width ($\sigma \approx 0.05$ GeV^2) and tends to merge with the kaon mass-squared peak at 0.24 GeV^2. In order to cleanly separate the pions from the kaons, the information for the TIC is used in conjunction with the mass-squared for final pion identification. For tracks in which the TIC has more than two pads hit within the fiducial area around the track, a loose mass-squared cut is applied (-0.15 GeV^2 $<$H3MSQ$<$0.2 GeV^2). For tracks in which there are only 1 or 0 TIC pads hit, a tighter mass-squared cut is applied (-0.15 GeV^2 $<$H3MSQ$<$0.10 GeV^2). The mass-squared distributions with and without the TIC cut are shown in

Figure 4.1. The plotted mass-squared distributions are for negative particles. The contamination by particles other than pions in the data sample is estimated to be less than 2% for the 131mr $\pi^+\pi^+$ data and less than 1% for the 44mr $\pi^-\pi^-$ data.

After an event has passed the event cut and has been found to contain at least two pions, it is written into the pair file. For each event, the run number, event number, T0 ADC value, silicon pad multiplicity and ADC sum, and number of pions are recorded in the pair file. For each track, the momentum (p_x, p_y, p_z), pad chamber x and y position, H2 slat and y position, H3 slat and y position, and number of SC hits for that track are recorded in the pair file.

One advantage of HBT analysis is that the normalization of the correlation function is arbitrary. Hence, the efficiency of a given cut is not important for the final results, and it is desirable to err on the side of caution when determining the exact cuts to use.

4.5 Forming the Correlation Function

The raw correlation function is

$$C_{raw}(\vec{k}_1, \vec{k}_2) = \frac{R(\vec{k}_1, \vec{k}_2)}{B(\vec{k}_1, \vec{k}_2)}, \tag{4.2}$$

where $\vec{k}_i$ are the particle momenta, $R(\vec{k}_1, \vec{k}_2)$ is the observed distribution of events with momenta $\vec{k}_1$ and $\vec{k}_2$, and $B(\vec{k}_1, \vec{k}_2)$ is the distribution of events with momenta $\vec{k}_1$ and $\vec{k}_2$ that would be observed if Bose-Einstein correlations were not present. $R(\vec{k}_1, \vec{k}_2)$ is often called the "real distribution", and $B(\vec{k}_1, \vec{k}_2)$ is often called the "background

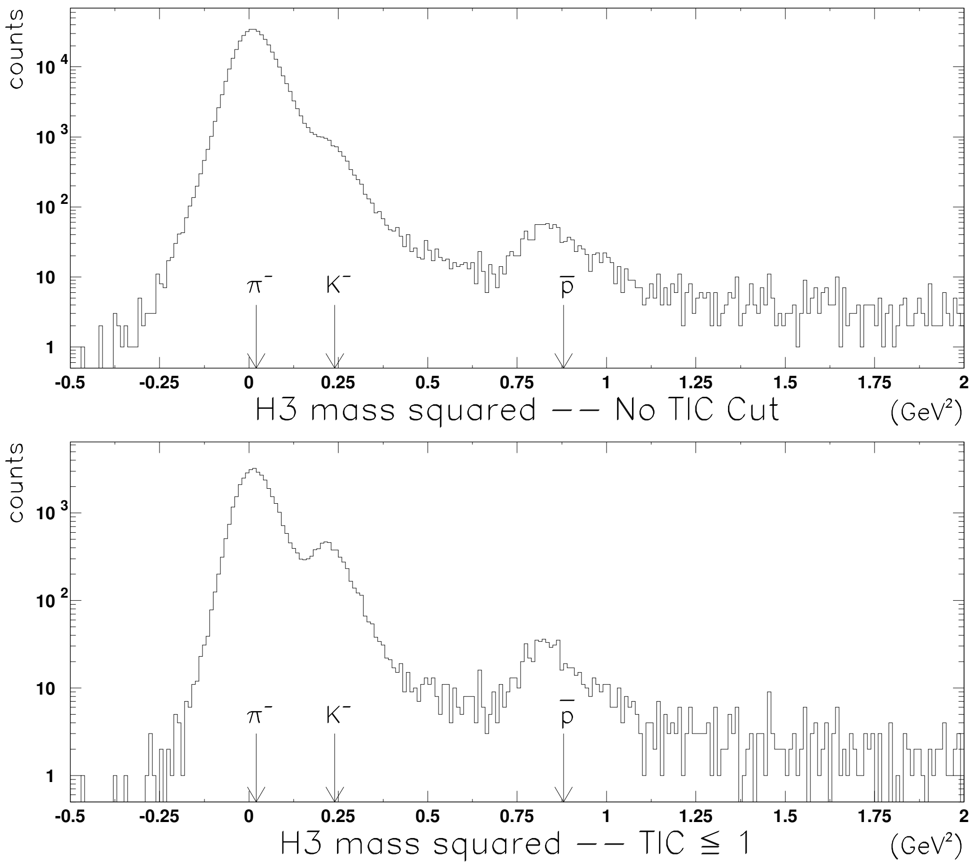

Figure 4.1: H3 mass squared distributions for the 44mr 4 GeV/c horizontal setting. The upper plot shows the distribution without any TIC cut. The lower plot shows the resulting mass squared distribution if each track is required to have less than 2 TIC pads hit. Also shown are the expected positions for the π^-, K^-, and $\bar{p}$ peaks.

distribution". The background distribution is formed by mixing events from the same data sample. The same analysis cuts are applied to the background distribution as are applied to the real distribution. Typically, ten background pairs are formed for each real pair so the statistical error is dominated by the real distribution.

After the raw correlation function is created, corrections are applied for the two-particle Coulomb repulsion of the outgoing pair (Coulomb correction), the experimental momentum resolution and two-track efficiency (Acceptance correction), and the distortion of the background due to residual correlations in the mixed events (Background Correction). In order to calculate the magnitude of these corrections a knowledge of the shape of the correlation function is necessary, so an iterative procedure is used where the parameterized shape of the correlation function from the previous iteration is used in the calculation of each correction. The results typically converge in less than 5 iterations.

4.5.1 Coulomb Correction

The Coulomb correction is calculated using the procedures described in Section 2.4.2. For large sources, the Coulomb Wave function integration technique is more accurate than the Gamow correction. In order to do the Coulomb Wave function integration, however, it is necessary to know the size of the pion-emitting source. The size of the pion-emitting source is taken from the fitted values of the radius parameters from the previous iteration.

Although the Gamow factor is known to over-estimate the value of the Coulomb correction for large sources, the data are also corrected using the Gamow correction. This is done primarily so that the current results can be compared with previous NA44 HBT results for the S+Pb system which used the Gamow correction in the data analysis [BOG95, BEK95].

4.5.2 Acceptance Correction

No physics detector is capable of making a perfect measurement, and the acceptance correction is used to account for the experimental distortions of the correlation function. There are two primary experimental effects that distort the correlation function. Finite momentum resolution tends to reduce the value of the correlation function at $Q = 0$ and increase the width. In addition, the Coulomb correction is calculated using the measured momentum difference and not the true momentum difference and this leads to a somewhat incorrect Coulomb correction.

In addition to problems of momentum resolution, the efficiency for resolving nearby tracks is closely linked to the efficiency for measuring pairs at low momentum difference. As an extreme example, consider two pions produced with exactly the same momentum. These pions would strike precisely the same location on each detector and would be considered a single track. This inefficiency tends to suppress the correlation function at low momentum difference and must be accounted for in the correction procedures.

The acceptance correction is calculated using the NA44 Monte-Carlo. Two particle events are simulated and reconstructed. For each event used in the calculation, there are two input momenta $(\vec{k}_1, \vec{k}_2)$ and two reconstructed momenta $(\vec{k}'_1, \vec{k}'_2)$. The acceptance correction $(K_{acceptance})$ is then

$$K_{acceptance} = \frac{C_2(ideal)}{C_2(reconstructed)} = \frac{\frac{R(\vec{k}_1,\vec{k}_2)}{B(\vec{k}_1,\vec{k}_2)}}{\frac{R(\vec{k}'_1,\vec{k}'_2)}{B(\vec{k}'_1,\vec{k}'_2)}}. \tag{4.3}$$

$R(\vec{k}_1, \vec{k}_2)$ is the real distribution of simulated events weighted by the Bose-Einstein correlation:

$$R(\vec{k}_1, \vec{k}_2) = \frac{d^6 N}{d^3\vec{k}_1\, d^3\vec{k}_2} \times C_2(\vec{k}_1, \vec{k}_2), \tag{4.4}$$

where $C_2(\vec{k}_1, \vec{k}_2)$ is calculated using the parameterized correlation function. $B(\vec{k}_1, \vec{k}_2)$ is the background distribution of simulated events:

$$B(\vec{k}_1, \vec{k}_2) = \frac{d^6 N}{d^3\vec{k}_1\, d^3\vec{k}_2}. \tag{4.5}$$

In forming the ideal correlation function, no cuts are applied to the simulated real or background distributions. As an example, the ideal correlation function used in the 1d Q_{inv} calculation of the 44mr $\pi^-\pi^-$ acceptance correction is shown in the top panel of Figure 4.2.

The denominator of the acceptance correction $(C_2(reconstructed))$ is formed using the reconstructed momenta $(\vec{k}'_1, \vec{k}'_2)$. In forming the reconstructed correlation function, the same cuts are applied to the MC data as the real data. $R(\vec{k}'_1, \vec{k}'_2)$ is the real distribution of reconstructed MC events weighted by the Bose-Einstein correlation calculated using the simulated momenta:

$$R(\vec{k}_1, \vec{k}_2) = \frac{d^6 N}{d^3 \vec{k}_1' \, d^3 \vec{k}_2'} \times C_2(\vec{k}_1, \vec{k}_2). \tag{4.6}$$

$B(\vec{k}_1', \vec{k}_2')$ is the background distribution, and it is formed from mixed MC events. Since in the real data the Coulomb correction is applied to background, $B(\vec{k}_1', \vec{k}_2')$ is corrected for the fact that the Coulomb correction has been applied the reconstructed momenta and not the true momenta. If $B_{raw}(\vec{k}_1', \vec{k}_2')$ is the raw distribution of mixed reconstructed MC pairs, then

$$B(\vec{k}_1', \vec{k}_2') = B_{raw}(\vec{k}_1', \vec{k}_2') \times \frac{K_{coul}(\vec{k}_1, \vec{k}_2)}{K_{coul}(\vec{k}_1', \vec{k}_2')}, \tag{4.7}$$

where $K_{coul}(\vec{k}_1, \vec{k}_2)$ is the Coulomb correction for a pair of particles with momenta $(\vec{k}_1, \vec{k}_2)$. The reconstructed MC Q_{inv} correlation function for the 44mr horizontal pions is shown in the second panel of Figure 4.2, and the acceptance correction for this data set is shown in the bottom panel of Figure 4.2.

Note that in calculating the acceptance correction, the Bose-Einstein weights are calculated using the radius and λ parameters extracted from the real data. Since the radius and λ parameters are not known *a priori*, an iterative procedure is used. Also, it is clear that the acceptance and Coulomb corrections cannot be factorized.

4.5.3 Background Correction

The background in the denominator of the correlation function in equation (4.2) is defined as the distribution of pairs of momenta $\vec{k}_1$ and $\vec{k}_2$ that would be observed

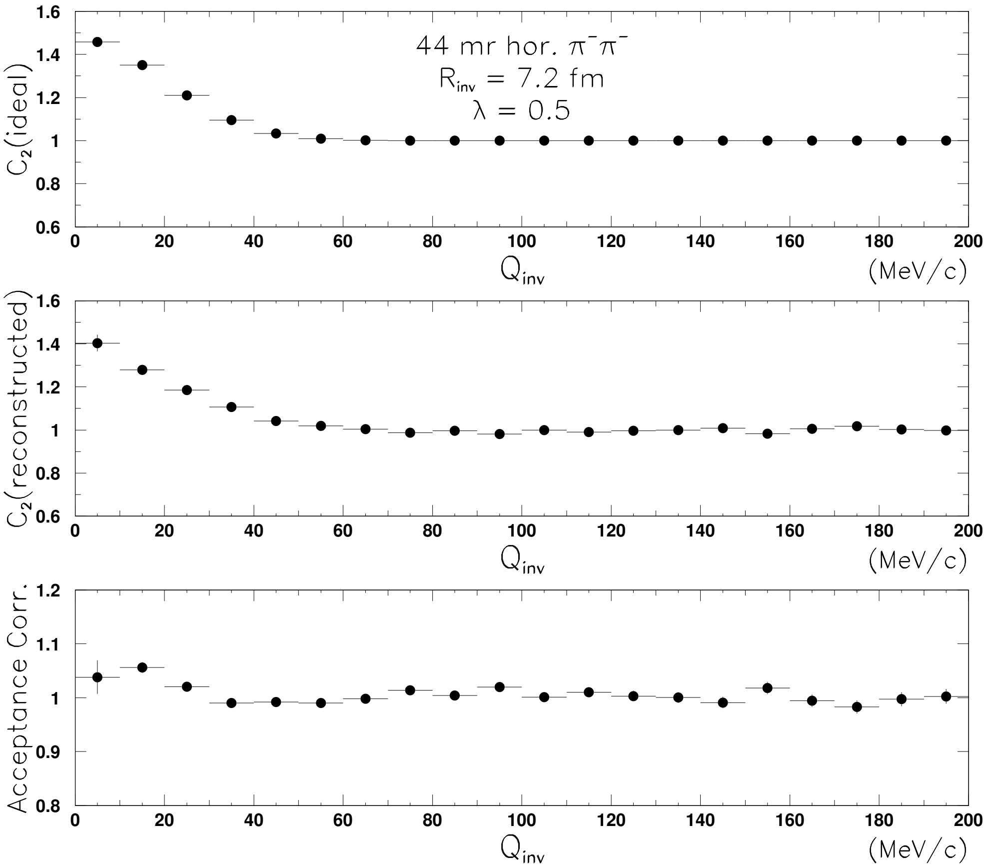

Figure 4.2: The ideal MC correlation function ($C_2(ideal)$), reconstructed MC correlation function ($C_2(reconstructed)$) and acceptance correction for the 44mr horizontal $\pi^-\pi^-$ data. The Bose-Einstein weights for each pair are calculated using $R_{inv} = 7.2$ fm and $\lambda = 0.5$.

in the absence of any Bose-Einstein correlations. This background is generated by mixing different events, so it might be assumed that all correlations are removed during the event mixing. In fact a small residual correlation remains in background if mixed pairs are used [ZAJ84], and the magnitude of these residual correlations is inversely proportional to the size of the detector acceptance [PEI93]. Since NA44 has a small acceptance, these background correlations need to be removed from the background sample.

The origin of the background correlations are shown in [ZAJ84]. The correlation function can be written as

$$C_2(\vec{k}_1, \vec{k}_2) = \frac{\frac{d^6 N}{d^3\vec{k}_1\, d^3\vec{k}_2}}{\frac{d^3 N}{d^3\vec{k}_1}\frac{d^3 N}{d^3\vec{k}_2}} = 1 + \Lambda(\vec{k}_1, \vec{k}_2), \tag{4.8}$$

where $\Lambda(\vec{k}_1, \vec{k}_2)$ is the structure of the correlation function. Using the event mixing technique, the single particle background distributions can be written as

$$\frac{d^3 N_B}{d^3\vec{k}_1} = \sum_{\vec{k}_2} \frac{d^6 N}{d^3\vec{k}_1\, d^3\vec{k}_2} \simeq \int_\Omega \frac{d^6 N}{d^3\vec{k}_1\, d^3\vec{k}_2} d^3\vec{k}_2, \tag{4.9}$$

where Ω is the region of integration (i.e. the detector acceptance). Using equation (4.8) we can rewrite the integrand in equation (4.9):

$$\begin{aligned}
\frac{d^3 N_B}{d^3\vec{k}_1} &\simeq \int_\Omega \frac{d^3 N}{d^3\vec{k}_1}\frac{d^3 N}{d^3\vec{k}_2}[1 + \Lambda(\vec{k}_1, \vec{k}_2)]d^3\vec{k}_2 && (4.10)\\
&\simeq \frac{d^3 N}{d^3\vec{k}_1}\int_\Omega \frac{d^3 N}{d^3\vec{k}_2}[1 + \Lambda(\vec{k}_1, \vec{k}_2)]d^3\vec{k}_2 && (4.11)\\
&\equiv \frac{d^3 N}{d^3\vec{k}_1}[1 + \Delta(\vec{k}_1; \Lambda)]. && (4.12)
\end{aligned}$$

The background formed using the event mixing technique ($d^3 N_B/d^3\vec{k}_1$) is not equal to the ideal background ($d^3 N/d^3\vec{k}_1$) that is used in the definition of the correlation function. Without corrections, the measured correlation function ($C_2'(\vec{k}_1, \vec{k}_2)$) using the background mixing technique is

$$C_2'(\vec{k}_1, \vec{k}_2) = \frac{1 + \Lambda(\vec{k}_1, \vec{k}_2)}{[1 + \Delta(\vec{k}_1; \Lambda)][1 + \Delta(\vec{k}_2; \Lambda)]}. \tag{4.13}$$

The measured correlation function is not equal to the ideal correlation function defined in equation (4.8) but has the unwanted terms ($[1 + \Delta(\vec{k}_1; \Lambda)][1 + \Delta(\vec{k}_2; \Lambda)]$) in the denominator.

If we assume a form of the correlation function, then the unwanted correlations in the background can be removed [ZAJ84]. For each background pair b_{ij}, a weight is calculated from the assumed form of the correlation function

$$\omega(b_{ij}) = [1 + \Delta(\vec{k_i}; \Lambda)][1 + \Delta(\vec{k_j}; \Lambda)]. \tag{4.14}$$

If the background distribution is weighted by this factor, the unwanted correlations in the background are removed.

In order to calculated the background correction, the form of the correlation function needs to be known. Of course, the form of the correlation function is what is being measured so it is not known in advance. In order to calculate the residual background correlations, the correlation function from the data is parameterized and used in the background correction. This requires an iterative approach to fitting the correlation function, and the procedure used by NA44 was first described in [BOG93]. On the first iteration, the uncorrected background is calculated

$$B^0(\vec{k}_1) = \sum_{\vec{k}_2} R(\vec{k}_1, \vec{k}_2), \tag{4.15}$$

where $R(\vec{k}_1, \vec{k}_2)$ is the observed distribution of two particle events. This background is then used to form the correlation function, and the correlation function is fit using a gaussian parameterization. On subsequent iterations, the corrected background spectrum is calculated using the fitted form of the correlation function

$$B^{i+1}(\vec{k}_1) = \sum_{\vec{k}_2} \frac{R(\vec{k}_1, \vec{k}_2)}{C^i_{fit}(\vec{k}_1, \vec{k}_2)}, \tag{4.16}$$

where $C^i_{fit}(\vec{k}_1, \vec{k}_2)$ is the fitted form of the correlation function from the previous iteration. This corrected background is then used in the fit of the correlation function, and the process is repeated until the results converge. The residual background correlation correction factor for the ith iteration is given by

$$K_{back}(\vec{k}_1, \vec{k}_2) = \frac{B^0(\vec{k}_1, \vec{k}_2)}{B^i(\vec{k}_1, \vec{k}_2)}, \tag{4.17}$$

where $B(\vec{k}_1, \vec{k}_2) = B(\vec{k}_1)B(\vec{k}_2)$ and the single particle distributions are calculated using equation (4.16).

4.5.4 Fully Corrected Correlation Function

The fully corrected correlation function is

$$C_2(Q) = C_{raw}(Q) \times K_{coul} \times K_{acc} \times K_{back}, \tag{4.18}$$

where Q is the momentum difference (Q_{inv} for 1d fits, (Q_{to}, Q_{ts}, Q_L) for 3d fits), $C_{raw}(Q)$ is the raw correlation function defined in equation (4.2), K_{coul} is the Coulomb correction (Gamow or Coulomb Wave), K_{acc} is the acceptance correction defined in equation (4.3), and K_{back} is the background correction defined in equation (4.16). It should be noted that since the corrections depend on the assumed shape of the correlation function, the final correlation function is somewhat model dependent. It is, however, impossible to calculate the acceptance and background corrections in a completely model independent way. NA44 assumes a gaussian shape for the correlation function, and the χ^2/DOF from the fits suggest that this is a reasonable assumption in most cases.

4.6 Fitting the Correlation Function

The correlation functions are fit using the MINUIT fitting package [MIN92]. Both the maximum likelihood and chi-squared minimization fitting approaches have been investigated, although the fitted results presented are obtained using the Chi-Squared Minimization technique.

Using the maximum likelihood method, the probability density function is assumed to obey Poisson statistics:

$$P(R_i|\bar{R}_i) = \frac{\bar{R}_i^{R_i}}{R_i!}e^{\bar{R}_i}, \qquad (4.19)$$

where R_i is the number of real counts in bin i, and $\bar{R}_i = C_i B_i$ is the expected number of counts in bin i assuming a functional value C_i and B_i background counts. The likelihood function to be maximized is

$$L = \prod_i P(R_i|\bar{R}_i). \qquad (4.20)$$

In reality, MINUIT is used to minimize the logarithm of the likelihood function so that the product can be replaced by a sum:

$$-\,ln(L) = \sum_i \bar{R}_i - R_i ln(\bar{R}_i) + ln(R_i!). \tag{4.21}$$

It is assumed in this fitting method that the background B_i has small statistical errors compared to R_i. This is approximately true since there are ten times as many background counts as real counts. Also, the acceptance correction K_{acc}, which enters into the calculation of B_i, has statistical errors but these tend to be small compared to the statistical error on the real data since there are roughly 5 times more MC pairs for the acceptance correction than real pairs in the data.

A second fitting technique is also used. This technique is the chi-squared minimization technique. Here the function minimized is

$$\chi^2 = \sum_{i,j} (C_i - R_i/B_i) V_{ij}^{-1} (C_j - R_j/B_j), \tag{4.22}$$

where A_i is the real distribution, B_i is the background distribution, C_i is the fit function, V_{ij} is the covariance matrix, and i, j are the indices for the different data points. If only uncorrelated statistical errors are considered, this expression reduces to

$$\chi^2 = \sum_i \frac{(C_i - R_i/B_i)^2}{\sigma_i^2}, \tag{4.23}$$

where σ_i is the estimated gaussian error on the quantity R_i/B_i. For bins in which there are a small number of counts, however, σ_i underestimates the true error [PAN93]. This leads to problems for bins near the edge of the NA44 acceptance where statistics are minimal. These bins are weighted too strongly in the fit and lead to an incorrect value of the normalization which in turn affects the other fit parameters. It was found, however, that if only bins with at least 30 counts in the real distribution are used in the fit, the maximum likelihood and chi-squared fitting approaches yield nearly identical results. The results of the maximum likelihood fits were found to be independent of the minimum number of counts required in a bin.

Although the chi-squared fitting approach has problems associated with low statistics bins, the fitted results presented use the chi-squared minimization technique. The reason for this is the ease by which systematic errors can be incorporated into the chi-squared fit using equation (4.22). Along with the statistical error on each bin, there is a systematic error. These systematic errors tend to dominate over the statistical error at low values of Q and should be included during the fit. The procedure used by NA44 for calculating systematic errors is outlined in [BEK94]. Contributions to the covariance matrix are additive, so the systematic errors can be calculated independently of the statistical errors. The systematic uncertainty on each point is estimated by varying the analysis conditions and calculating the correlated and uncorrelated change in each of the data points. If there are N variations of the analysis conditions, then the contribution to the covariance matrix from the systematic uncertainty in the data points is

$$V_{ij}^{sys} = [\frac{\sum_{k=1}^{N} C_{ik}C_{jk}}{N} - C_i^{mean}C_j^{mean}]\frac{N}{N-1}, \tag{4.24}$$

where i, j are the data points. The total covariance matrix is then

$$V_{ij} = V_{ij}^{sys} + V_{ij}^{stat}; \quad V_{ij}^{stat} = 0 \text{ if } i \neq j. \tag{4.25}$$

This matrix is inverted and used in equation (4.22) to find the fit parameters. The error calculation includes both correlated and uncorrelated errors, and during the final fit only bins with at least 30 counts in the real distribution are used. More technical details on the systematic error calculation can be found in Appendix B.

CHAPTER 5

EXPERIMENTAL RESULTS AND DISCUSSION

The results for the 44mr $\pi^-\pi^-$ data and 131mr $\pi^+\pi^+$ data will be presented. These will be compared to 44mr $\pi^+\pi^+$ data that were analyzed independently. The results will then be compared to NA44 interferometry results for S+Pb collisions, as well as interferometry results from similar heavy systems at lower energies.

5.1 One-Dimensional Correlation Functions

As mentioned in Chapter 2, one-dimensional Q_{inv} fits are useful in the limit of low statistics. The current data sets do not suffer from insufficient statistics, but one-dimensional fits are performed nonetheless. The data are parameterized by a gaussian

$$C_2(Q_{inv}) = 1 + \lambda e^{-R_{inv}^2 Q_{inv}^2}, \tag{5.1}$$

where $Q_{inv} = \sqrt{|\vec{Q}|^2 - Q_0^2}$. The one-dimensional correlation functions use only data from the horizontal setting. The 44mr $\pi^-\pi^-$ data have a mean transverse momentum (p_T) of 150 MeV/c, while the 131mr $\pi^+\pi^+$ data have a mean p_T of 450 MeV/c.

The one-dimensional correlation functions in Q_{inv} are shown along with the gaussian fit functions in Figure 5.1. Note that the error bars on the data points are statistical only, while the fit functions are calculated using both statistical and systematic errors. The data are corrected for residual background correlations, acceptance effects, and the two-particle Coulomb repulsion between the outgoing pion pairs. For the data shown in Figure 5.1, the Coulomb Wave correction, explained in Section 2.4.2, is used.

Figure 5.2 compares the Coulomb Wave and Gamow corrected data. It is clear the Gamow correction is significantly larger at low Q_{inv}. This is to be expected since the Gamow correction assumes that all pion pairs originate from a point source.

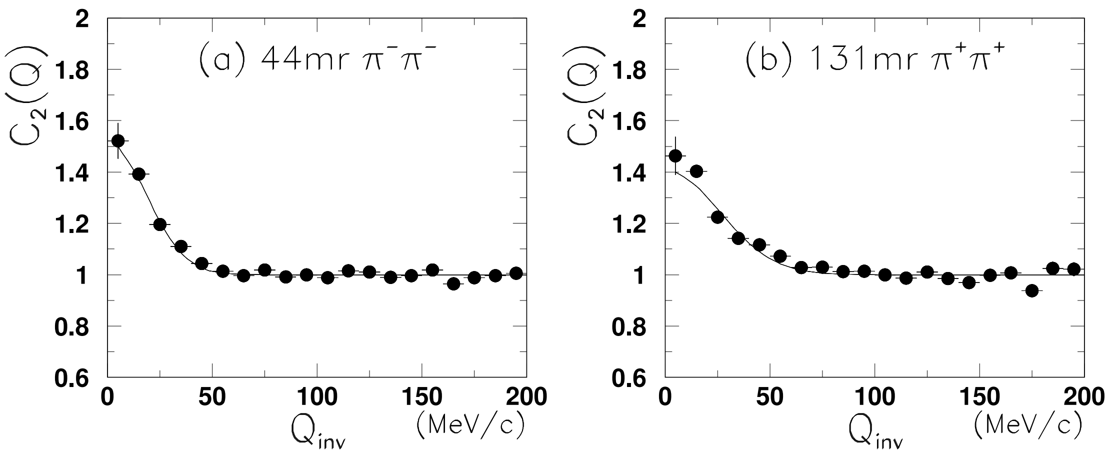

Figure 5.1: The correlation functions in Q_{inv} for the (a) 44mr $\pi^-\pi^-$, and (b) 131 mr $\pi^+\pi^+$ data. The fit functions are also included. These correlation functions are fully corrected and use the Coulomb Wave correction. Error bars on the data points are statistical only.

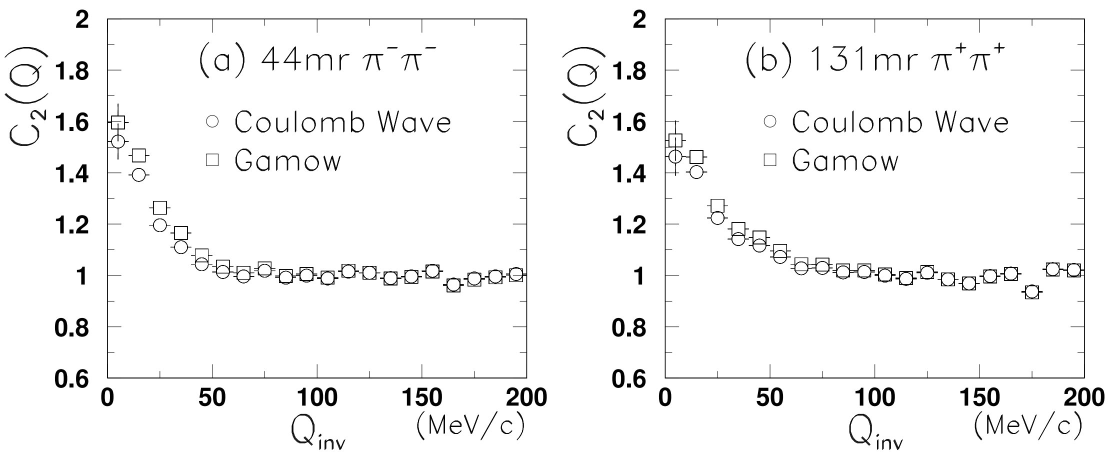

Figure 5.2: A comparison of the Coulomb Wave corrected and Gamow corrected correlation functions in Q_{inv} for the (a) 44mr $\pi^-\pi^-$, and (b) 131 mr $\pi^+\pi^+$ data. Error bars on the data points are statistical only.

The results of the gaussian fits of the correlation functions are listed in Table 5.1 along with the χ^2/DOF for the fit. Both the Coulomb Wave corrected and Gamow corrected results are listed. Note that in the fitting process, all bins are used.

The λ parameter is significantly less than unity for both data sets. The λ parameter should be unity for a single, completely incoherent source. Pions from resonance decays, however, tend to suppress the λ parameter, so it is impossible to determine directly from the data whether the reduction in the λ parameters comes from the resonance decay contribution to the pion sample or whether the source has a coherent component. This question will be addressed when the data are compared to model predictions.

	System	λ	R_{inv} (fm)	χ^2/DOF
Coulomb	44mr $\pi^-\pi^-$	0.517 $\pm$ 0.040	7.56 $\pm$ 0.38	30/36
Wave	131mr $\pi^+\pi^+$	0.407 $\pm$ 0.031	5.39 $\pm$ 0.36	51/35
Gamow	44mr $\pi^-\pi^-$	0.556 $\pm$ 0.033	6.62 $\pm$ 0.29	32/36
	131mr $\pi^+\pi^+$	0.446 $\pm$ 0.029	4.94 $\pm$ 0.28	56/35

Table 5.1: Fitted results of Gaussian parameterizations of the 44mr $\pi^-\pi^-$ and 131mr $\pi^+\pi^+$ correlation functions in Q_{inv}. The errors are statistical+systematic.

Looking at the χ^2/DOF for the fits, it is clear that the 44mr $\pi^-\pi^-$ data are well described by a gaussian, while the 131mr $\pi^+\pi^+$ data are not. The χ^2/DOF for the Coulomb Wave corrected 131mr $\pi^+\pi^+$ data is 51/35, whereas it would be expected that the χ^2/DOF would be of order unity if the data were well described as a gaussian. In the iterative process used to correct the data it is assumed that the correlation function is gaussian. Hence, the deviation of the 131 mr $\pi^+\pi^+$ data from a gaussian shape suggests that the corrections applied to these data are not very accurate. In Figure 5.1, the data are compared to the fit function and there is large discrepancy in the lowest two Q_{inv} bins. Because of the larger statistics, the fit is dominated by the region 25 MeV/c$\leq Q_{inv} \leq$75 MeV/c, and it is clear that the gaussian assumption is also invalid in this region.

The χ^2/DOF is smaller for the Coulomb Wave corrected data than the Gamow corrected data. If it is assumed that correlation function should be described by a gaussian, this is further evidence that the Coulomb Wave correction is more accurate than the Gamow correction.

The radius parameter R_{inv} is larger for the low p_T $\pi^-\pi^-$ data than the higher p_T $\pi^+\pi^+$ data. Assuming perfect isospin symmetry and neglecting Coulomb effects, it can be concluded that the low p_T data originates from a larger source than the high p_T data. In reality, neither the isospin imbalance of the Pb+Pb system or the Coulomb effects should be ignored.

5.2 Three-Dimensional Correlation Functions

In Section 2.5.2 it was shown that significantly more information can be gained from HBT measurements if the data are analyzed in three dimensions. In section 3.2 it was shown that NA44 is suited for such measurements provided that the horizontal and vertical settings are analyzed simultaneously. All data presented have been analyzed in LCMS reference frame and fit using the Bertsch-Pratt parameterization discussed in sections 2.5.2 and 2.6:

$$C_2(Q_{TO}, Q_{TS}, Q_L) = A(1 + \lambda e^{-Q_{TO}^2 R_{TO}^2 - Q_{TS}^2 R_{TS}^2 - Q_L^2 R_L^2}), \tag{5.2}$$

or,

$$C_2(Q_{TO}, Q_{TS}, Q_L) = A(1 + \lambda e^{-Q_{TO}^2 R_{TO}^2 - Q_{TS}^2 R_{TS}^2 - Q_L^2 R_L^2 - 2Q_{TO} Q_L R_{OL}^2}), \tag{5.3}$$

where A is a normalization constant. Note that the horizontal and vertical settings are allowed to have different normalization constants during the fitting process.

The projections of the fully corrected 44mr $\pi^-\pi^-$ correlation function are shown in Figure 5.3. These projections extend over the lowest 20 MeV/c in the other directions of the momentum difference. Both the horizontal and vertical data are shown.

Included is a projection of the fitted gaussian parameterization. As shown in Figures 3.4 and 3.5, the horizontal setting has larger statistics in the lowest $\vec{Q}$ bins and hence dominates the fit at low $\vec{Q}$. There are some small discrepancies between the horizontal and vertical settings at low $\vec{Q}$, but the systematic errors on the vertical data are large compared to the statistical errors in this region.

The projections of the fully corrected horizontal and vertical 131mr $\pi^+\pi^+$ correlation is shown along with the projection of the fitted gaussian parameterization in Figure 5.4. Compared to the 44mr $\pi^-\pi^-$ correlation function, it is clear that the higher p_T pions have a much wider correlation function and a larger intercept at $Q = 0$.

Figure 5.5 and 5.6 show the projected correlation functions and fit functions for the 44mr $\pi^-\pi^-$ and 131mr $\pi^+\pi^+$ data with the R^2_{OL} cross term included in the gaussian parameterization. In this case, Q_{TO} is defined to be positive, while Q_L can be positive or negative. It has been assumed that due to azimuthal symmetry only the magnitude of Q_{TS} is important [CNH95]. The Q_{TO} and Q_L projections show only the data from the horizontal setting while the Q_{TS} setting shows only the data from the vertical setting.

Table 5.2 show the fitted three-dimensional lambda and radius parameters for the 44mr $\pi^-\pi^-$ and 131mr $\pi^+\pi^+$ data. The fitted results for both the Coulomb Wave corrected and Gamow corrected data are listed. Table 5.3 lists the three-dimensional fit results when the R^2_{OL} cross term is included in the fit function. In this case, only the Coulomb Wave corrected results are listed.

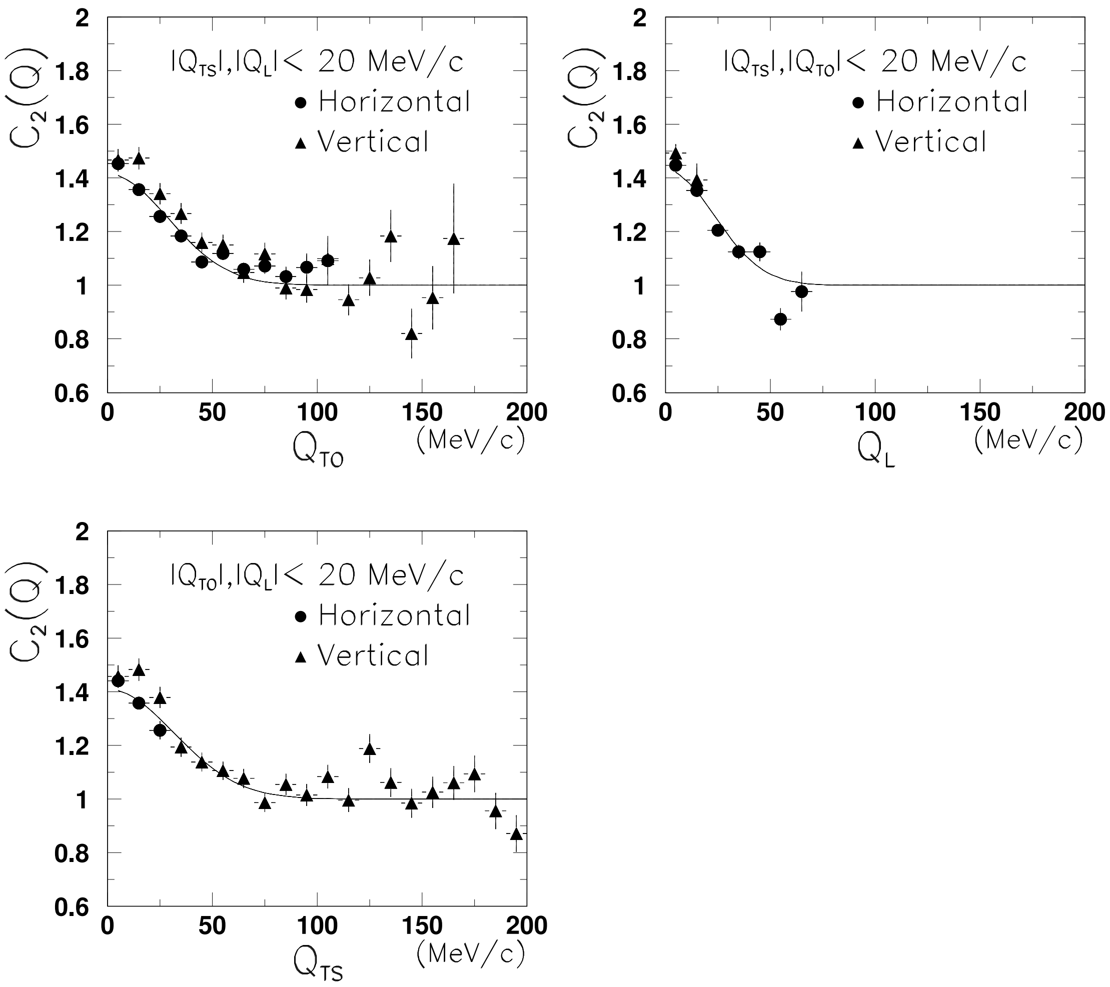

Figure 5.3: The projections of the 44mr $\pi^-\pi^-$ correlation function using the standard Bertsch-Pratt parameterization. The projections from both the horizontal and vertical settings are shown, as well as the projection of the gaussian fit to the data. This correlation function is fully corrected and uses the Coulomb Wave correction. Error bars on the data points are statistical only.

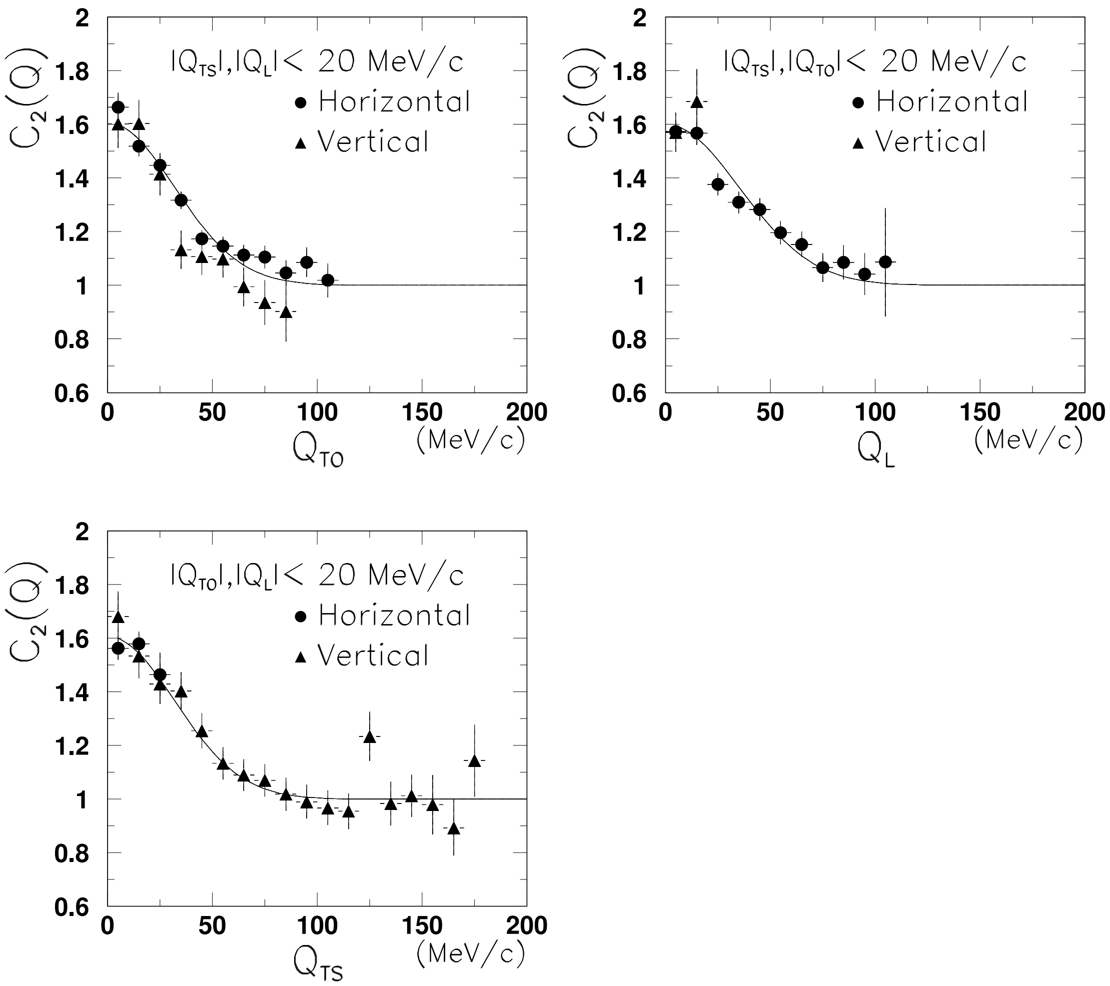

Figure 5.4: The projections of the 131mr $\pi^+\pi^+$ correlation function using the standard Bertsch-Pratt parameterization. The projections from both the horizontal and vertical settings are shown, as well as the projection of the gaussian fit to the data. This correlation functions is fully corrected and uses the Coulomb Wave correction. Error bars on the data points are statistical only.

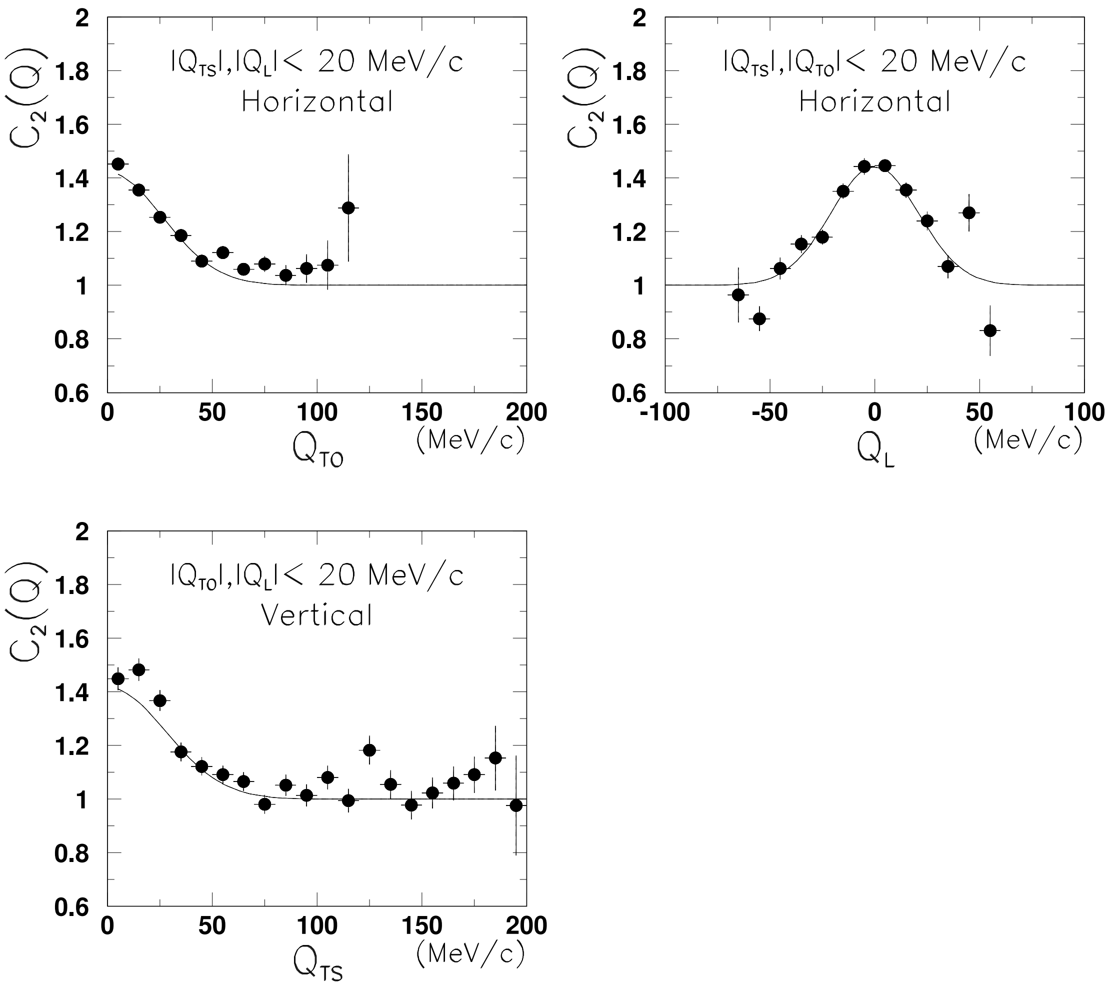

Figure 5.5: The projections of the 44mr $\pi^-\pi^-$ correlation function using the three-dimensional parameterization with the R^2_{OL} cross term. The Q_{TO} and Q_L projections come from the horizontal setting, while the Q_{TS} projection comes from the vertical setting. This correlation function is fully corrected and uses the Coulomb Wave correction. Error bars on the data points are statistical only.

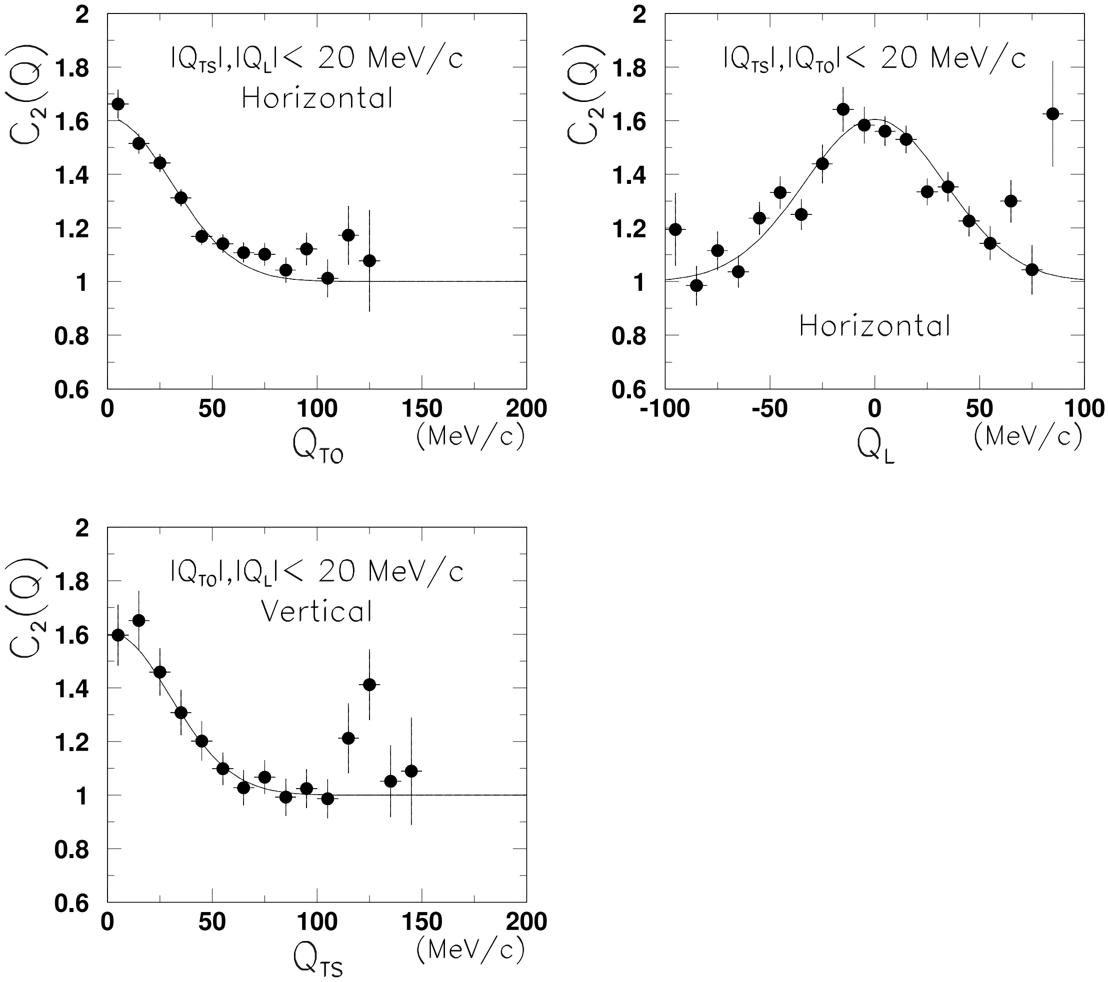

Figure 5.6: The projections of the 131mr $\pi^+\pi^+$ correlation function using the three-dimensional parameterization with the R_{OL}^2 cross term. The Q_{TO} and Q_L projections come from the horizontal setting, while the Q_{TS} projection comes from the vertical setting. This correlation function is fully corrected and uses the Coulomb Wave correction. Error bars on the data points are statistical only.

	System	λ	R_{TO} (fm)	R_{TS} (fm)	R_L (fm)	χ^2/DOF
Coul.	44mr $\pi^-\pi^-$	0.495 ± 0.023	4.88 ± 0.21	4.45 ± 0.32	6.03 ± 0.35	1683/2105
Wave	131mr $\pi^+\pi^+$	0.679 ± 0.034	4.39 ± 0.18	4.39 ± 0.31	3.96 ± 0.23	1125/1574
Gamow	44mr $\pi^-\pi^-$	0.526 ± 0.022	4.36 ± 0.18	4.09 ± 0.26	5.55 ± 0.30	1684/2105
	131mr $\pi^+\pi^+$	0.707 ± 0.033	4.06 ± 0.16	4.21 ± 0.28	3.75 ± 0.20	1124/1574

Table 5.2: Fitted results of three-dimensional Gaussian parameterizations of the 44mr $\pi^-\pi^-$ and $\pi^+\pi^+$ correlation functions in Q_{TO}, Q_{TS} and Q_L. The results with both the Coulomb Wave and Gamow corrections are listed. Errors are statistical+systematic.

System	λ	R_{TO}(fm)	R_{TS}(fm)	R_L(fm)	R^2_{OL}(fm^2)	χ^2/DOF
44mr $\pi^-\pi^-$	0.524 ± 0.026	5.35 ± 0.25	5.07 ± 0.35	6.68 ± 0.39	10.7 ± 2.9	1822/2279
131mr $\pi^+\pi^+$	0.693 ± 0.037	4.59 ± 0.21	4.71 ± 0.36	4.15 ± 0.25	3.1 ± 1.4	1187/1655

Table 5.3: Fitted results of Gaussian parameterizations of the 44mr $\pi^-\pi^-$ and 131mr $\pi^+\pi^+$ correlation functions in Q_{TO}, Q_{TS} and Q_L including the R^2_{OL} cross-term. Only the results with the Coulomb Wave correction are listed. Errors are statistical+systematic.

Before discussing the implications of the fitted results, it is useful to understand that the exact meaning of the fit parameters and errors. For the three-dimensional fits without the cross-term there are 6 fit parameters. These are $norm_h, norm_v, \lambda, R_{TO}, R_{TS}$, and R_L, where $norm_h$ and $norm_v$ are the horizontal and vertical normalizations respectively. For each fit value (A_i), a one standard deviation error is quoted (σ_i). This means that there is 68% chance that the true value of the parameter A_i lies between $A_i - \sigma_i$ and $A_i + \sigma_i$. The probability that two fit parameters are both within 1 σ of the quoted value is only 46%. Hence, for a 6 parameter fit, the probability is very small that the true value of all 6 parameters are within 1 σ of the fit values.

In addition, the fit parameters are highly correlated. This correlation is especially strong between the radius parameters and λ. A larger λ yields larger radii. As an example, the correlation coefficient between λ and R_{TO} is roughly 0.5 for the 44mr $\pi^-\pi^-$ data presented here. This means that if the true value of λ is 1 σ larger than the quoted value, then the true value of R_{TO} is roughly 0.5 σ larger than the quoted value.

Comparing the λ parameter from the one-dimensional Q_{inv} fits to the λ parameter from the three-dimensional fits, there is very good agreement for the 44mr $\pi^-\pi^-$ data but very poor agreement for the 131mr $\pi^+\pi^+$ data. As discussed earlier, the 1d gaussian parameterization does not seem to be very good for the 131mr $\pi^+\pi^+$ data, and this is probably the cause of the discrepancy in the λ parameters. The χ^2/DOF for the three-dimensional fits suggest that the gaussian parameterization is in fact valid for both data sets.

The low p_T $\pi^-\pi^-$ data have a transverse radius of 4.5-5.0 fm and a longitudinal radius of 6 fm. The gaussian equivalent of the hard sphere radius for a Pb projectile is

$$R_{gauss}(Pb) \simeq \frac{1.2A^{1/3}}{\sqrt{5}} = 3.2fm. \tag{5.4}$$

The initial projectile is much smaller than the freeze-out radii measured by the low p_T HBT measurements – this suggests that the system expands before the particles freeze-out.

For a first order phase transition from the Quark-Gluon Plasma, it is expected that there will be a long duration of particle emission. The signature for such a scenario would be the $R_{TO} \gg R_{TS}$. Using a cascade model, it was shown that this signature is only valid for low p_T pions [FSS95]. For the low p_T $\pi^-\pi^-$ measurement, $R_{TO} \approx R_{TS}$. Hence there is no direct evidence for a long duration of pion emission. It should be noted that the mean p_T of pions in the 44mr NA44 acceptance is 150 MeV/c, and the lifetime effect is most pronounced for pions with p_T <100 MeV/c. It should also be noted that the centrality of the data samples considered is $(\sigma_{trig}/\sigma_{geom}) \approx 18\%$. It is possible that at this centrality, no QGP state is formed or that any QGP state formed is very short-lived.

5.3 Comparison to 44mr $\pi^+\pi^+$ Data

NA44 has also measured the reaction Pb+Pb$\rightarrow \pi^+\pi^+ + X$ for the 158 GeV/nucleon Pb projectile. Comparing the 44mr $\pi^+\pi^+$ data to the 44mr $\pi^-\pi^-$ data taken in the same acceptance region should test whether isospin and/or central Coulomb effects are important for the interferometry measurements. The Pb+Pb has a large isospin imbalance (164 protons and 252 neutrons). Although it can probably be assumed that pions originating from the primary collision region should not have any isospin effects, the resonance decay contributions to the pion sample should be different for π^+ and π^-. As an example, the isospin imbalance of the Pb+Pb system should lead to an enhancement in the production of Λ's over $\bar{\Lambda}$'s, and the primary decay mode for the Λ is to a pion and a nucleon. Hence it would be expected that there are more π^-'s from Λ decay than π^+'s.

The 44mr $\pi^+\pi^+$ data were analyzed independently using very similar analysis techniques [Bea97]. The one-dimensional correlation functions in Q_{inv} along with the projections of the three-dimensional correlation functions in the standard Bertsch-Pratt parameterization are compared for the 44mr $\pi^-\pi^-$ and $\pi^+\pi^+$ data in Figure 5.7. Visually, the agreement between the two data sets is rather good. For the Q_{inv} parameterization, all data points seem to agree within the error bars except for the first point. For the three-dimensional projections the agreement is also good.

The fitted lambda and radius parameters for the 44mr $\pi^+\pi^+$ data are listed in Table 5.4. The one-dimensional fit of the 44mr $\pi^+\pi^+$ differs slightly from the fits of the data presented previously in that the first data point is not used in the fitting process. Neglecting this point reduces the radius and λ parameter.

System	λ	R_{inv} (fm)	χ^2/DOF
44mr $\pi^+\pi^+$	0.503 ± 0.046	6.66 ± 0.41	39/26

System	λ	R_{TO} (fm)	R_{TS} (fm)	R_L (fm)	χ^2/DOF
44mr $\pi^+\pi^+$	0.569 ± 0.035	5.50 ± 0.26	5.87 ± 0.58	6.53 ± 0.48	1423/1720

Table 5.4: Fitted results of one-dimensional and three-dimensional Gaussian parameterizations of the 44mr $\pi^+\pi^+$ correlation function taken from [Bea97]. The results are from Coulomb Wave corrected data. Errors are statistical+systematic.

Comparing the three-dimensional fit results for the 44mr $\pi^-\pi^-$ (Table 5.2) and 44mr $\pi^+\pi^+$ data one finds that the three-dimensional λ and radius parameters are larger for the $\pi^+\pi^+$ data. The difference in the λ parameter is roughly 2 σ, and the

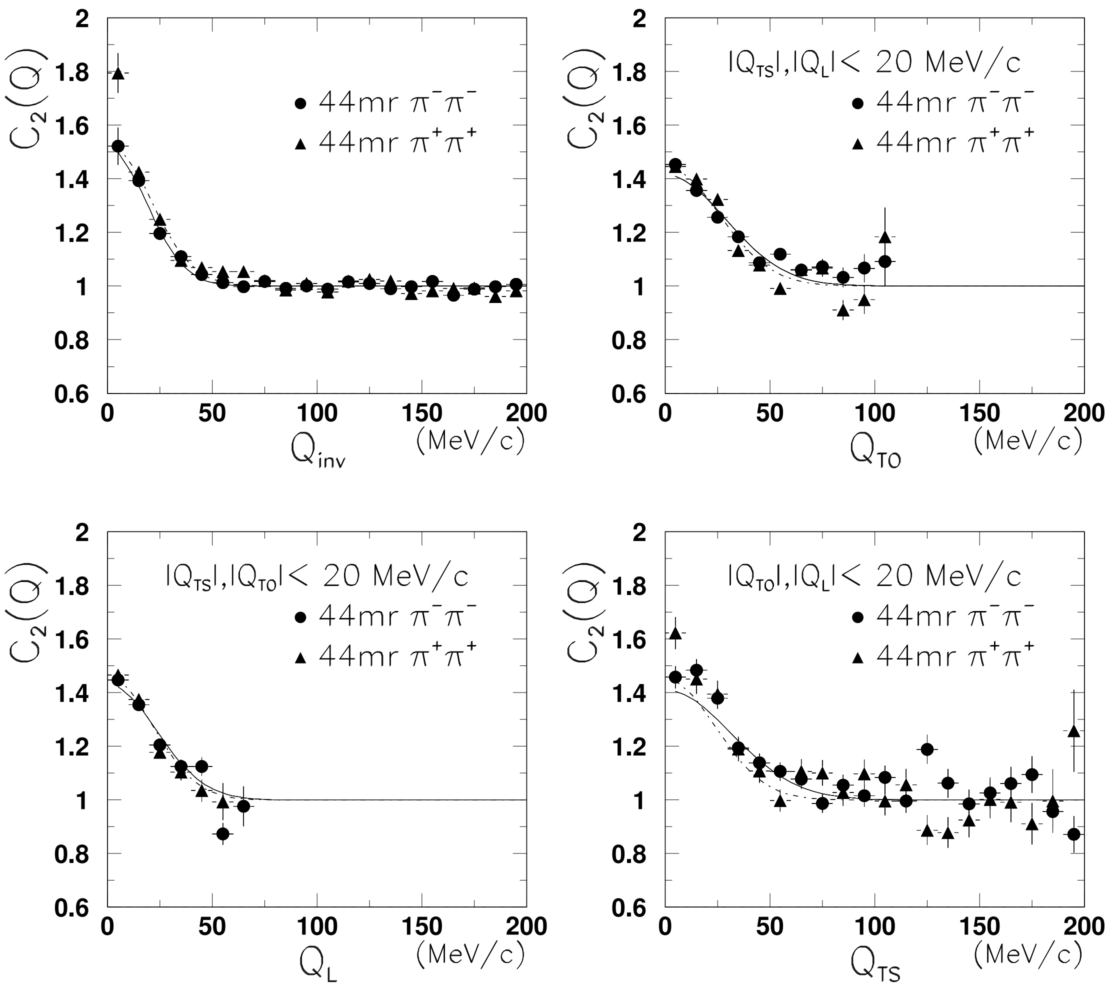

Figure 5.7: Comparisons of the 44mr $\pi^-\pi^-$ and $\pi^+\pi^+$ correlation functions in Q_{inv} and the projections of the three-dimensional correlation functions. The projections in Q_{TO} and Q_L come from the horizontal setting and the projection in Q_{TS} comes from the vertical setting. These correlation functions are fully corrected and use the Coulomb Wave correction. Error bars on the data points are statistical only. The fit to the $\pi^-\pi^-$ is the solid line, and the fit to the $\pi^+\pi^+$ data is the dashed-dotted line.

radius parameters are larger by 1-3 σ. As mentioned previously, however, the λ parameter is strongly correlated with the radii in the fits. In order to test whether these differences are physically significant, a χ^2 difference per degree of freedom comparison was made between the two data sets. The overall χ^2 difference per degree of freedom is 2837/2951. Most of the data, however, is in the flat region of the correlation function. A second χ^2 difference between the two data sets was calculated for bins in which $|Q_{TO}|, |Q_{TS}|, |Q_L| <$80 MeV/c. In this region of the Bose-Einstein correlation, the χ^2 difference per degree of freedom is 450/440. Since this value is close to unity, it is impossible to say that there is a statistically significant difference between the 44mr $\pi^-\pi^-$ and $\pi^+\pi^+$ data. As an additional test, the 44mr $\pi^-\pi^-$ data was fit with the λ parameter fixed to the value taken from the $\pi^+\pi^+$ fit, and the radius parameters were found to agree within 1 σ.

The 131mr $\pi^+\pi^+$ data, however, are clearly different than the 44mr $\pi^+\pi^+$ data. A χ^2 difference per DOF test was performed for bins in which $|Q_{TO}|, |Q_{TS}|, |Q_L| <$80 MeV/c, and the result was 518/371. The λ parameter is larger for the high p_T data, and all three radius parameters are smaller. The change in radius parameters is largest for R_L. The larger λ parameter for the high p_T data can be understood quite easily in terms of a reduced resonance contribution to the pion sample. Resonances tend to produce pions of low p_T, so the resonance contribution to the low p_T data is much larger. This leads to the smaller λ parameter for the low p_T data.

The decrease in radii with increasing p_T can arise in several ways. In a baryon rich environment, the interferometric radii are related to the mean free path of a pion in nuclear matter. Higher p_T pions have a smaller elastic scattering cross section with a nucleon. Hence higher p_T pions leave the source at an earlier time when the size of the system is smaller. Another possible explanation is that the pions arise from a system with a transverse flow gradient – faster pions tend to originate from a region towards the surface (where the transverse flow is largest). A third explanation is the short-lived resonance contribution to the pion sample [SX96]. In reality, these three effects can all be important. The cause of the decreasing radii with increasing transverse momentum is best understood in the context of specific models and this question will be address in Chapter 6.

5.4 Comparison to NA44 S+Pb Results

Pion interferometry measurements were performed by the NA44 collaboration for the system S+Pb at 200 GeV/nucleon [BOG93, BOG95, BEK95]. The experimental apparatus was significantly different, but the acceptance was the same and thus the results can be compared directly. Events from the 3% most central events were analyzed.

The fitted results from the one-dimensional parameterization of the correlation functions are listed in Table 5.5. The fitted results from the the three-dimensional parameterization of the correlations function are list in Table 5.6. The NA44 collaboration only took horizontal S+Pb 44mr $\pi^-\pi^-$ data, so the error on R_{TS} is rather large. Note that in the S+Pb correlation analysis, the Gamow correction was used instead of the Coulomb Wave correction. Hence, it is most accurate to compare the

S+Pb results to the Gamow corrected Pb+Pb results. In reality, the smaller system sizes for the S+Pb system mean that the Gamow correction is a very good approximation of the Coulomb Wave calculation. The radii extracted using the Coulomb Wave calculation are only 5% larger than those extracted using the Gamow correction and the λ parameter is unchanged [BEK95].

System	λ	R_{inv} (fm)	χ^2/dof
44mr $\pi^-\pi^-$	0.42 ± 0.02	4.00 ± 0.27	19/25
44mr $\pi^+\pi^+$	0.56 ± 0.02	5.00 ± 0.22	29/25
131mr $\pi^+\pi^+$	0.48 ± 0.02	4.27 ± 0.23	27/20

Table 5.5: Fitted results of Gaussian parameterizations of the S+Pb$\rightarrow \pi^+\pi^+ + X$ and S+Pb$\rightarrow \pi^-\pi^- + X$ correlation functions in Q_{inv}. The data are Gamow corrected and the results are taken from [BEK95, BOG95]. Errors are statistical+systematic.

System	λ	R_{T_o} (fm)	R_{T_s} (fm)	R_L (fm)	χ^2/dof
44mr $\pi^-\pi^-$	0.49 ± 0.03	3.61 ± 0.20	3.71 ± 0.80	4.43 ± 0.35	3029/1174
44mr $\pi^+\pi^+$	0.56 ± 0.02	4.02 ± 0.14	4.15 ± 0.27	4.73 ± 0.26	1201/1415
131mr $\pi^+\pi^+$	0.55 ± 0.02	2.97 ± 0.16	2.95 ± 0.24	3.09 ± 0.19	1500/1095

Table 5.6: Fitted results of Gaussian parameterizations of the S+Pb$\rightarrow \pi^+\pi^+ + X$ and S+Pb$\rightarrow \pi^-\pi^- + X$ correlation functions in Q_{TO}, Q_{TS} and Q_L. The data are Gamow corrected and the results are taken from [Lee93, BOG95, BEK95]. Errors are statistical+systematic.

Comparing the one-dimensional results, the radius parameter are larger for Pb induced collisions than S induced collision. This is also true for the results from the three-dimensional parameterization. The radius parameters, however, do not seem to scale with the nuclear radii. The ratio of the Pb to S nuclear radii is 1.87. The ratio of the measured 44mr $\pi^-\pi^-$ Pb+Pb and S+Pb sideward radii is 1.10 ± 0.25. Since the S+PB $\pi^-\pi^-$ results come only from the horizontal setting, it is perhaps better to compare to the 44mr S+Pb $\pi^+\pi^+$ results. In this case, the ratio of the sideward radii is 0.98 ± 0.09. For the 131mr $\pi^+\pi^+$ results, the ratio of the measured sideward radii is 1.43 ± 0.15. Since R_{TS} is thought to scale most directly with the size of the system, this suggests the final freeze-out radius is not very sensitive to the initial size of the system. Of course, the Pb+Pb interferometry results come from less central collisions (top 18%) than the S+Pb interferometry results (top 3%) and this could reduce the freeze-out radius.

For the 44mr data, the λ parameter is very similar for Pb+Pb collisions and S+Pb collisions. If it assumed that the λ parameter is determined primarily by the fraction of pions that come from resonances, then this suggests that the resonance pion production relative to the direct pion production is very similar in S+Pb and Pb+Pb collisions. As a function of p_T, however, the λ parameter for S+Pb collisions decreases slightly for the higher p_T pions, whereas for the Pb+Pb system it increases with increasing p_T.

5.5 Comparison to Pion Interferometry Results at Lower Energies

The CERN SPS is currently the highest energy heavy-ion facility available. Lower energy pion interferometry measurements have been performed at the Brookhaven Alternating Gradient Synchrotron using a ^{197}Au beam at 10.8 GeV/nucleon [Bar97] and at the Lawrence Berkeley Laboratory Bevalac using a ^{139}La beam at 1.26 GeV/nucleon [Bos93].

When comparing interferometry results from different experiments it is very important to understand the acceptances of the different detectors and the details of the correlation analysis. The Bevalac results come from the Janus Spectrometer [Cha91]. This spectrometer had two angular setting, $\theta_{lab} = 0\%$ and $\theta_{lab} = 45\%$. The 45% setting is close to mid-rapidity so it can be compared most directly to NA44 results. The p_T range of the 45% setting is 100-1000 MeV/c. The correlation function is parameterized by

$$C_2(Q_T, Q_L, Q_0) = 1 + \lambda e^{(-Q_T^2 R_T^2 - Q_L^2 R_L^2 - Q_0^2 R_0^2)/2}, \tag{5.5}$$

where $Q_0 = |E_1 - E_2|$ is the energy difference. The Bevelac data were analyzed in the Center-of-Mass frame, but for the mid-rapidity data this frame should be almost equivalent to the LCMS frame.

Comparing to the E877 results [Bar97] is a little more precarious since the E877 acceptance is at forward rapidity. The mean rapidity of the E877 pion sample is 3.1 while mid-rapidity for collisions at 10.8 GeV/c is 1.57. The p_T range of the E877 pion acceptance is $0 < p_T < 500$ MeV/c which is very similar to the NA44 44mr acceptance. The correlations are analyzed in the beam rapidity frame (i.e. y=3.14). Since the mean pion rapidity is 3.1, this frame is almost equivalent to the LCMS frame. It should be noted, however, that since these interferometry measurements are at forward rapidity, the projectile fragment region of the source is sampled. For S+S at 200 GeV/nucleon collisions, however, it was shown that the radius parameters do not depend very strongly on the rapidity of the pions [Alb95b], and it might be expected that the same is true for Au+Au collisions at 10.8 GeV/c. The E877 analysis uses the Pratt-Bertsch parameterization of the correlation function with R_{OL}^2 cross-term, so the equivalent NA44 results from Table 5.3 will be used for comparison. The centrality of the E877 measurements is the top 10% of the geometrical cross section.

Figure 5.8 shows that center of mass energy dependence of the R_{TO} and R_L radius parameters for heavy symmetric systems. For the La+La results at 1.26 GeV/nucleon it has been assumed that $R_{TO} \approx R_T$. Both the transverse and longitudinal radii increase dramatically when the beam energy increases from 1.26 GeV/nucleon to 10.8 GeV/nucleon. Somewhat surprisingly, as the beam energy is further increased from 10.8 GeV/nucleon to 158 GeV/nucleon, R_L increases only slightly and R_{TO} decreases. This could be a signal for the onset of new physics.

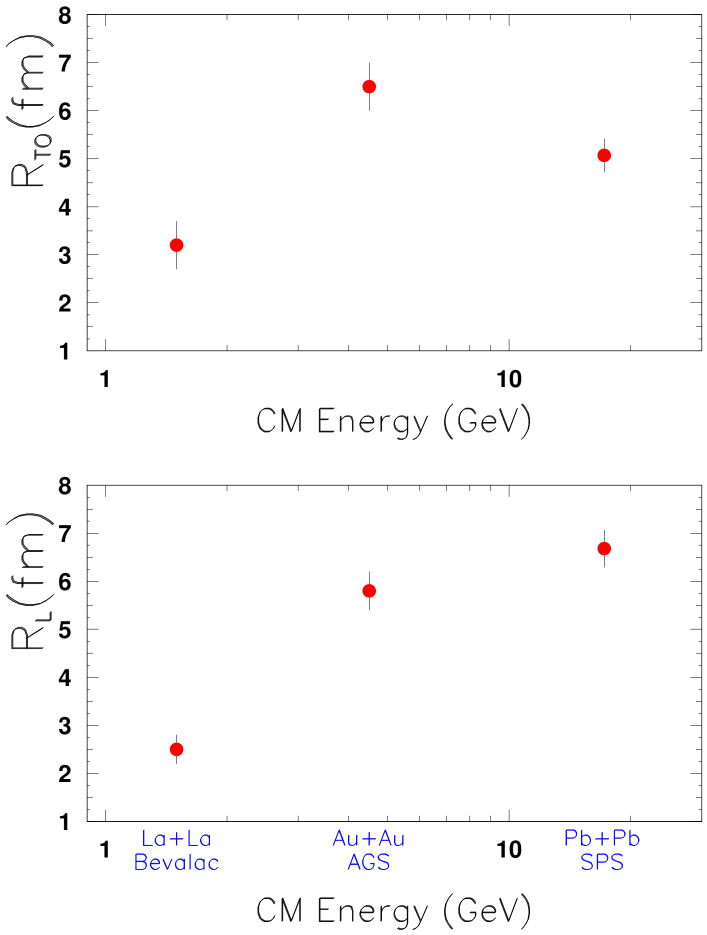

Figure 5.8: The center of mass energy dependence of the $\pi^-\pi^-$ transverse and longitudinal radius parameters. The La+La results come from [Bos93] and the Au+Au results come from [Bar97].

CHAPTER 6

MODEL COMPARISONS

The space-time evolution of a relativistic heavy-ion collision is a very complicated process that cannot be described very well analytically. The experimental data yield little insight without comparison to specific models. In this chapter, the data will be compared to two specific models, both of which have been found to describe previous experimental data reasonably well. The first model is Relativistic Quantum Molecular Dynamics (RQMD), a semi-classical transport model that seeks to explain the evolution of a heavy-ion collision from first principles. The second model used is a simple rescattering model that is useful for disentangling the effect of final state strong rescattering on the measured experimental observables. In addition, the simple rescattering model will be used to understand the effects of the central Coulomb potential on the current pion interferometry measurements.

6.1 Comparison to RQMD

RQMD is an attempt to model a nucleus-nucleus collision from the stage before the nuclei collide until the final freeze-out of all particles [Sor95]. The model will be explained here only briefly, but more details can be found in [SSG89, SSG89b, SKM90]. In high energy nucleus-nucleus collisions, such as Pb+Pb at 158 GeV/nucleon, RQMD initial goes through a pre-hadronic stage. In this stage, the system exists in the form of excited strings and resonances. If the density is sufficient, the strings may fuse into "color ropes", which are a model for locally deconfined quark matter. Eventually the strings and color ropes decay into normal hadrons and resonances which then interact via strong binary collisions. After strong rescattering, the particles freeze-out, yielding a prediction for the phase space density function $S(x,p)$ for the produced particles. This phase space density function can then be used to predict experimental observables, which are then compared to experiment. In the case of interferometry measurements, comparison to a model such as RQMD is useful in that it allows one to determine which characteristics of the final state are probed via HBT. To a lesser extent, it allows one to determine the sensitivity of the measured observables to underlying physics in the pre-hadronic stage.

The two particle emission probability is [SBJ93]:

$$P(\vec{p}_1,\vec{p}_2) = \int d^3r_1 dt_1 d^3r_2 dt_2 S(\vec{r}_1,t_1,\vec{p}_1) S(\vec{r}_2,t_2,\vec{p}_2) |\psi_{12}(\vec{r}_1,\vec{p}_1;\vec{r}_2,\vec{p}_2)|^2, \qquad (6.1)$$

where $\psi_{12}(\vec{r_1}, \vec{p_1}; \vec{r_2}, \vec{p_2})$ is the two-particle symmeterized wave function including final state Coulomb and strong interactions. The correlation function is calculated as

$$C_2(Q) = \sum_{i=1}^{N(Q)} \frac{|\psi_{12i}|^2}{N(Q)}, \tag{6.2}$$

where $N(Q)$ is the number of pairs in each Q bin. Since ψ_{12} is the Coulomb distorted outgoing wave function, the correlation function needs to be Coulomb corrected in order to compare to the experimental data. This is done using the same iterative Coulomb Wave function integration method used for the NA44 data. Separate correlation functions are formed corresponding to the horizontal and vertical NA44 acceptances, and these correlation functions are fit simultaneously in the same way as the NA44 data. In addition, the centrality trigger of NA44 is modeled and RQMD events are selected to match the centrality range of the data.

The predicted RQMD correlation function for the 44mr $\pi^-\pi^-$ and 131mr $\pi^+\pi^+$ settings are compared to the NA44 data in Figures 6.1 and 6.2. For the 44mr $\pi^-\pi^-$ setting, the agreement between RQMD is reasonably good although RQMD predicts a narrower correlation function. In contrast, RQMD predicts the correct widths for the 131mr $\pi^+\pi^+$ data but seems to drastically overpredict the intercept at $Q = 0$. The results from the one-dimensional and three-dimensional parameterizations of the predicted RQMD correlation functions are listed in Tables 6.1 and 6.2, respectively. Also included are the results of the gaussian parameterization of the RQMD 44mr $\pi^+\pi^+$ correlation function.

For Pb+Pb collisions at 158 GeV/nucleon, RQMD predicts a much larger λ parameter for the high p_T pion pairs compared to the low p_T pion pairs. This is in contrast

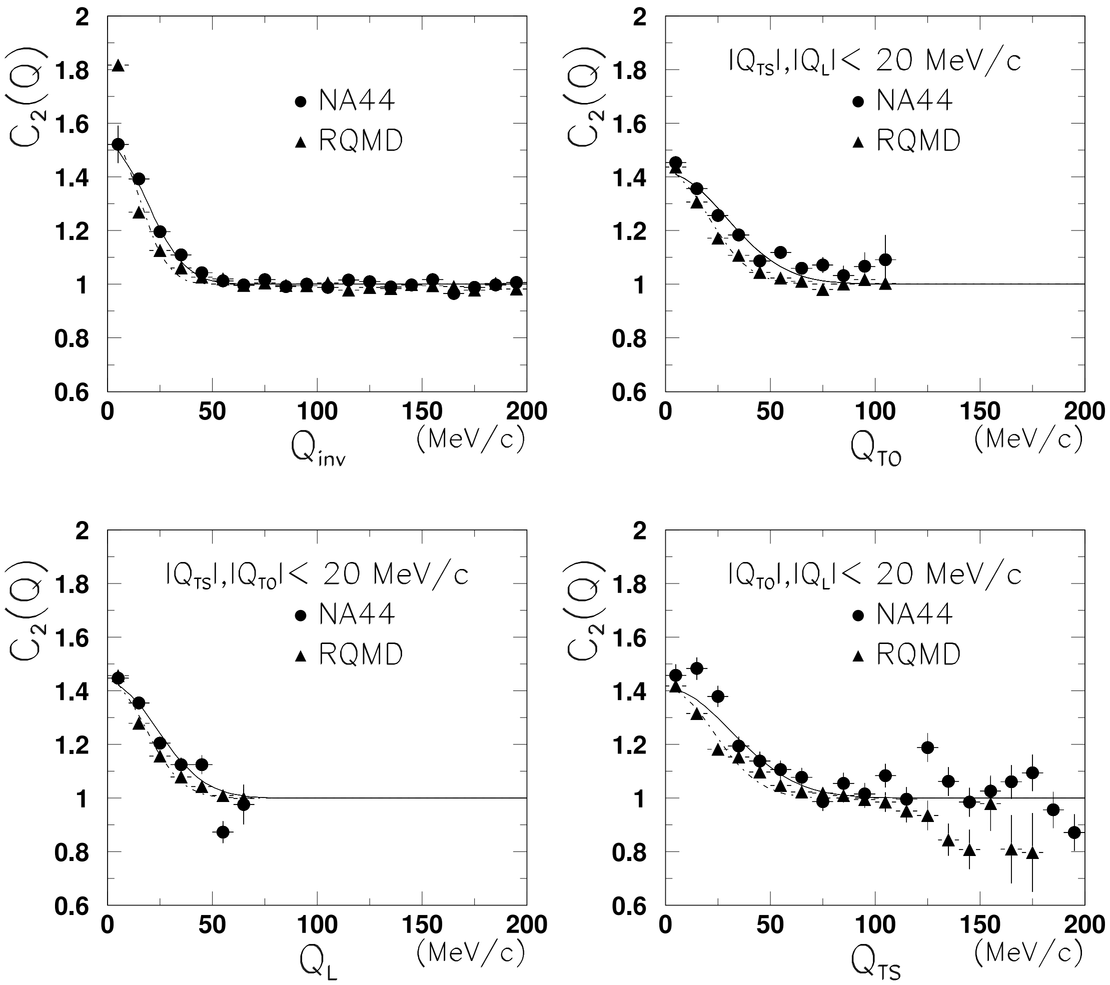

Figure 6.1: Comparisons of the NA44 and RQMD 44mr $\pi^-\pi^-$ correlation functions in Q_{inv} and the projections of the three-dimensional correlation functions. The projections in Q_{TO} and Q_L come from the horizontal setting and the projection in Q_{TS} comes from the vertical setting. Error bars on the data points are statistical only. The fit to the NA44 data is the solid line, and the fit to the RQMD prediction is the dashed-dotted line.

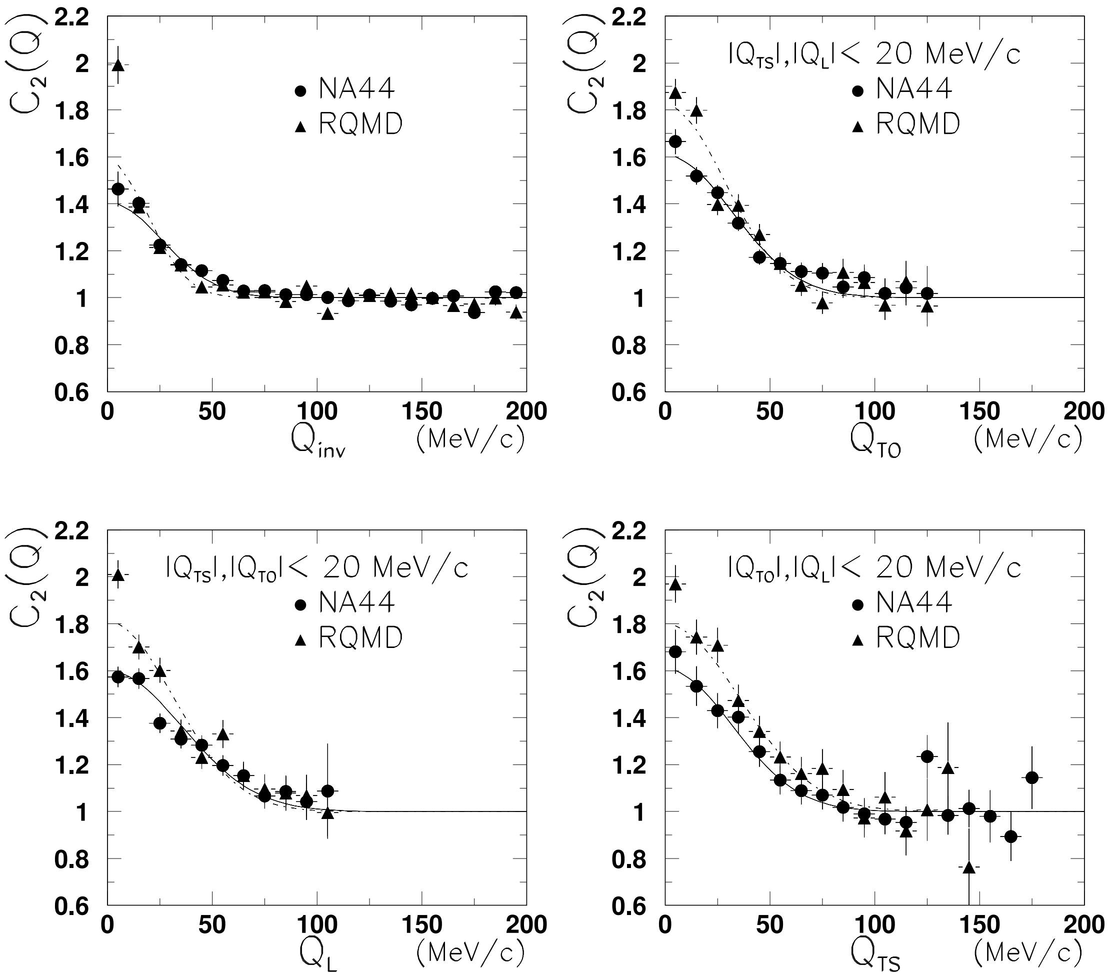

Figure 6.2: Comparisons of the NA44 and RQMD 131mr $\pi^+\pi^+$ correlation functions in Q_{inv} and the projections of the three-dimensional correlation functions. The projections in Q_{TO} and Q_L come from the horizontal setting and the projection in Q_{TS} comes from the vertical setting. Error bars on the data points are statistical only. The fit to the NA44 data is the solid line, and the fit to the RQMD prediction is the dashed-dotted line.

System	λ	R_{inv} (fm)	χ^2/N
44mr $\pi^-\pi^-$	0.58 $\pm$ 0.02	9.96 $\pm$ 0.29	11.0
131mr $\pi^+\pi^+$	0.59 $\pm$ 0.05	7.36 $\pm$ 0.48	3.4
44mr $\pi^+\pi^+$	0.67 $\pm$ 0.02	9.06 $\pm$ 0.21	8.6

Table 6.1: Fitted results of Gaussian parameterizations of the RQMD $\pi^+\pi^+$ and $\pi^-\pi^-$ correlation functions in Q_{inv}.

System	λ	R_{TO} (fm)	R_{TS} (fm)	R_L (fm)	χ^2/N
44mr $\pi^-\pi^-$	0.58 $\pm$ 0.01	6.96 $\pm$ 0.14	6.23 $\pm$ 0.20	7.94 $\pm$ 0.21	1.38
131mr $\pi^+\pi^+$	0.92 $\pm$ 0.04	4.93 $\pm$ 0.17	3.92 $\pm$ 0.21	4.47 $\pm$ 0.22	1.35
44mr $\pi^+\pi^+$	0.67 $\pm$ 0.01	6.43 $\pm$ 0.11	5.49 $\pm$ 0.14	7.68 $\pm$ 0.17	1.39

Table 6.2: Fitted results of Gaussian parameterizations of the RQMD $\pi^+\pi^+$ and $\pi^-\pi^-$ correlation functions in Q_{TO}, Q_{TS} and Q_L.

to the S+Pb RQMD predictions where the 44mr and 131mr correlation functions from RQMD have similar λ parameters [BEK95]. This suggests that RQMD under-predicts the fraction of high p_T pions coming from resonance decays in Pb+Pb collisions. It should be noted, however, that the RQMD correlation functions are made assuming a detector with perfect momentum resolution and two-track efficiency. It is believed that the NA44 data have been properly corrected for these experimental problems, but these corrections are somewhat uncertain at extremely low Q.

Comparing the fitted radii from RQMD for the 44mr $\pi^-\pi^-$ and $\pi^+\pi^+$ settings, it is interesting to note that RQMD predicts a smaller λ parameter and larger radii for the $\pi^-\pi^-$ data. This is in conflict with the NA44 measurements. RQMD does not include Coulomb interactions, so the predicted difference in the correlation function for the positives and negatives must be due to an isospin imbalance effect. It would be expected that the increased number of π^- coming from Λ decays would lead to such an effect. This is a bit difficult to study, however, since most Λ's decay in the first dipole magnet and are hence reconstructed with the wrong momentum. This fact is not included in the current RQMD calculations.

Although the agreement between the NA44 data and RQMD is not perfect, RQMD can nonetheless be used to look back into the source and see what is actually being measured. Figure 6.3 shows the freeze-out distributions for RQMD pions in x, y, z, and t, where z is beam direction and x is defined as the center of the NA44 azimuthal acceptance. The freeze-out distributions are shown for both the low and high angle settings. It is clear that only a small part of the source is sampled. In particular, the x distribution shows that source seems somewhat opaque - pions in the NA44 acceptance come from the side of the source in the direction of the detector. For the 131mr setting, the opacity effect is even worse - pions freeze-out from the edge of the source. Also note that the higher p_T pions tend to freeze-out at an earlier time.

These freeze-out distributions can be characterized by a mean freeze-out space-time position and a variance around the mean. These values, calculated from RQMD, are listed in Table 6.3 for all pions, pions in the 44mr horizontal and vertical acceptances, and pions in the 131mr horizontal and vertical acceptance. One important experimental question that can be addressed here is whether or not it is valid to use two settings (horizontal and vertical) with slightly different acceptances to measure the three-dimensional correlation function. Table 6.3 shows that horizontal and vertical settings do in fact measure essentially the same source, so the method used by NA44 to measure the three-dimensional correlation function is valid.

	x		y		z		t	
	mean	σ	mean	σ	mean	σ	mean	σ
ALL	0.0	5.6	0.0	5.7	0.0	8.6	19.9	16.4
44 mr H	2.8	5.0	0.0	5.1	4.3	5.5	17.2	7.5
44 mr V	3.3	4.7	0.0	5.0	3.6	5.6	16.8	7.5
131 mr H	5.8	3.5	0.0	4.2	0.6	4.8	14.4	6.9
131 mr V	5.8	3.5	0.0	4.2	0.1	4.7	14.3	6.8

Table 6.3: The RQMD freeze-out distributions for pions, characterized by a mean value and σ (both in fm). 'All' refers to all pions from RQMD, 'H' is the horizontal setting, and 'V' is the vertical setting.

Looking at Tables 6.2 and 6.3 it is clear that the difference between R_{TO} and R_{TS} does not give an accurate indication of the duration of particle emission. Looking at the expressions for the radii in terms of variances (equation (2.44)), the lifetime can be extracted assuming that the two transverse dimensions of the system are equal (i.e. $\langle x^2 \rangle \approx \langle y^2 \rangle$):

$$\tau \approx \frac{R_{TO}^2 - R_{TS}^2}{\beta_T^2}, \tag{6.3}$$

where τ is the duration of particle emission and β_T is the mean transverse velocity of the pairs. For an opaque source, however, this expression is not valid since $\langle x^2 \rangle \neq \langle y^2 \rangle$.

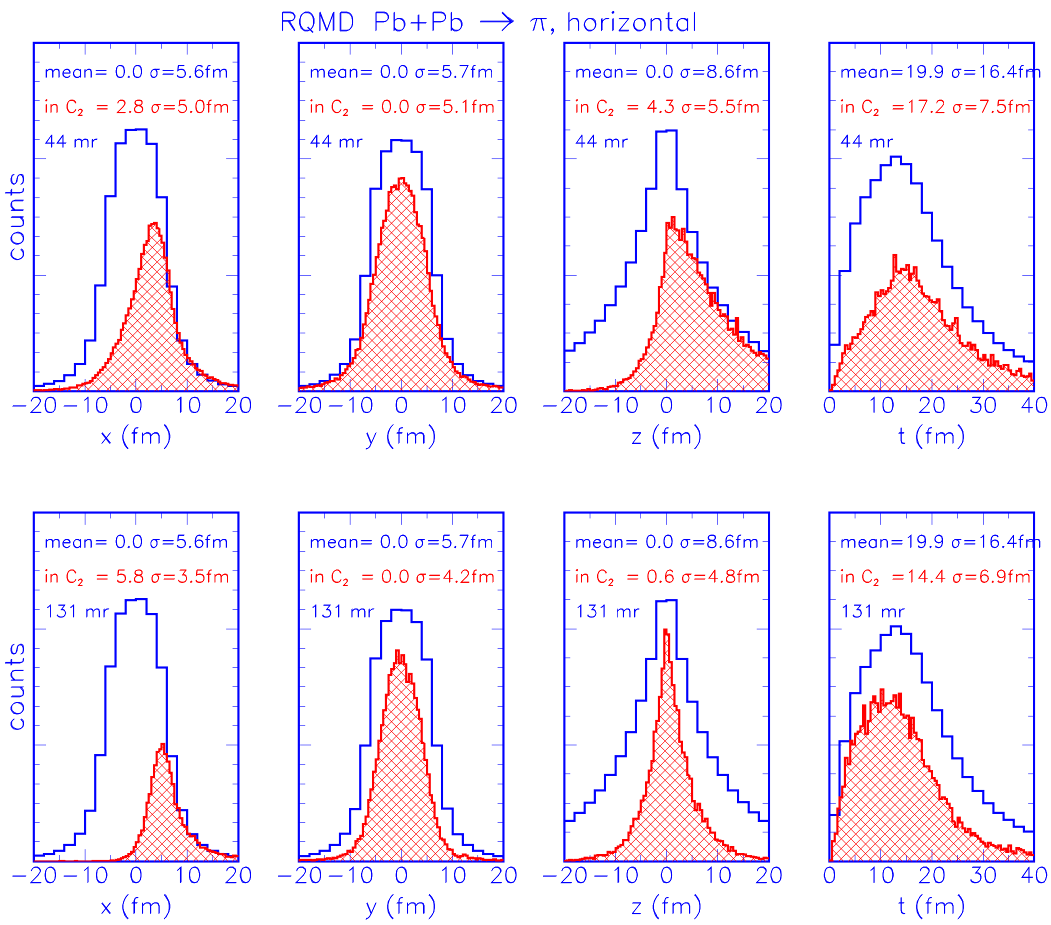

Figure 6.3: The RQMD freeze-out distributions for pions in cartesian coordinates. The empty histograms are for all pions, and the filled histograms are for pions in the NA44 horizontal acceptances. The top panels are for the 44mr horizontal setting, and the bottom panels are for the 131mr horizontal setting. The relative normalizations are arbitrary.

6.2 Comparison to a Simple Rescattering Model

The RQMD calculations essentially have two stages. In the initial stage, the authors make some theoretical conjecture about the behavior of nuclear matter under extreme conditions. After this, the calculations enter the hadronic stage where the evolution of the system is governed by the well known physics of the strong interaction. One question that should be asked is how sensitive the model predictions are to the assumptions about the early stages of the collision. A way of addressing this question is to study directly the effects of the rescattering stage on the hadronic observables. In order to do this, a simple rescattering model [Hum94, Hum96, Hum97] was developed.

In the rescattering model calculations, no attempt is made to understand the earliest stage of the collisions. The evolution of the system begins after all particles have hadronized. The initial transverse radius of the system is simply taken to be the transverse radius of the projectile, and the z distribution and hadronization time for the particles are given by the the inside-outside cascade model. In this model, each particle freezes out at a fixed time in its local reference frame:

$$z_{had} = \tau\ cosh(y), \tag{6.4}$$

$$t_{had} = \tau\ sinh(y), \tag{6.5}$$

where y is the rapidity and τ is the local hadronization time. The initial multiplicities N_i and rapidity distributions σ_i for the various particles species i are extracted from experimental data. The initial transverse momentum distributions for the particles are given by a Boltzmann thermal distribution

$$\frac{1}{m_T}\frac{dN_i}{dm_T} \propto e^{-m_T/T_i}, \tag{6.6}$$

where T_i is the slope parameter for a particle of species i. The slope parameters for the various particles are related to the intial freeze-out temperature T_{init} and the initial transverse expansion velocity β_{init} by

$$T_i = T_{init} + m_i\beta_{init}^2, \tag{6.7}$$

where m_i is the mass of particle i. This relation was derived empirically from NA44 transverse mass spectra [Bea97b].

Initially, the rescattering calculation included only nucleons, pions and kaons [Hum94, Hum96]. This leads to problems when comparing to HBT data since pions from resonance decays influence the shape of the correlation function and reduce the λ parameter. For this reason, the $\rho, \omega, \eta, \eta', \phi, \Delta$, and K^* resonances were added to the model [Hum97]. Resonances are present in the initial stage, but can also be created during the rescattering stage.

After initialization the particles scatter with one another using isospin averaged cross sections. The scattering processes include resonance production and decay. After the scattering process, the particles freeze out and a list of positions, momenta, and particle types is produced. No long range Coulomb interactions are included in the model.

After the list of freeze-out positions and momenta have been created, the correlation function is formed. The calculation of the correlation function is similar to the

RQMD calculation except that the plane wave approximation is used (i.e. final state Coulomb distortions are ignored). In the plane wave approximation, the weighting factor in equation (6.1) is

$$|\psi_{12}(\vec{r}_1, \vec{p_1}; \vec{r}_2, \vec{p}_2)|^2 = 1 + cos[(\vec{r}_1 - \vec{r}_2) \cdot (\vec{p}_1 - \vec{p}_2) - (t_1 - t_2) \cdot (E_1 - E_2)]. \qquad (6.8)$$

The correlation function is then fit in the three-dimensional Bertsch-Pratt parameterization.

There are several other additional simplifications in the rescattering model calculations compared to the RQMD calculations. The model of the NA44 acceptance is simplified such that there are not separate horizontal and vertical settings, but the rapidity and p_T range of the NA44 acceptances are taken into account. Also, there are no impact parameter considerations in the rescattering model calculations. The initial multiplicities, which should be related to the impact parameter, are taken from central collisions. Because of this lack of impact parameter considerations, the events look very similar and can thus be combined to improve the statistics in the correlation function. The calculations presented here use only 50 events.

In principle the model has many free parameters, but most can be constrained by experimental data. The initial multiplicities and rapidity distributions are taken directly from experiment. This essentially leaves three free parameters. These are the intial temperature (T_{init}) and transverse expansion velocity (β_{init}) from equation (6.7) and the hadronization time (τ). NA44 has measured the single inclusive spectra for pions, kaons, and protons [Bea97b] and the slope parameters from these data can be used to constrain these parameters but not to fix them entirely. It was found that the NA44 single particle data can be described equally well under at least two distinct scenarios [Hum97]. For a short hadronization time ($\tau = 1$fm/c), matching the NA44 slopes data requires a very high initial temperature ($T_{init} \approx 270$MeV) and no initial transverse expansion. In contrast, a long hadronization time ($\tau = 10$fm/c) requires a lower initial temperature ($T_{init} \approx 140$MeV) and a large initial transverse expansion $\beta_{init} = 0.45$. For the shorter hadronization time, the initial density is higher leading to a larger amount of rescattering that can generate the collective expansion implied by the NA44 slopes data.

HBT data can be used to uniquely determine the initial conditions for the rescattering model. It was shown that within this model, the low p_T longitudinal radius (R_L) is very sensitive to the hadronization time and grows with increasing τ [Hum97]. The model predicts that R_L will be roughly 8 fm for $\tau = 1$ fm/c and roughly 11 fm for $\tau = 10$ fm/c. Hence, the comparisons here will be made for the case where $\tau = 1$ fm/c. The NA44 44mr $\pi^-\pi^-$ and 131mr $\pi^+\pi^+$ data are compared to the predictions of the rescattering model in Figures 6.4 and 6.5, respectively. The predicted values for the fits to the rescattering model correlation functions are listed in Table 6.4.

System	λ	R_{TO} (fm)	R_{TS} (fm)	R_L (fm)
44mr $\pi\pi$	0.63 ± 0.03	6.37 ± 0.26	5.55 ± 0.12	8.13 ± 0.63
131mr $\pi\pi$	0.56 ± 0.02	4.35 ± 0.30	3.90 ± 0.26	4.71 ± 0.30

Table 6.4: Fitted results of Gaussian parameterizations of the rescattering model $\pi\pi$ correlation functions in Q_{TO}, Q_{TS} and Q_L for the NA44 44mr and 131mr settings.

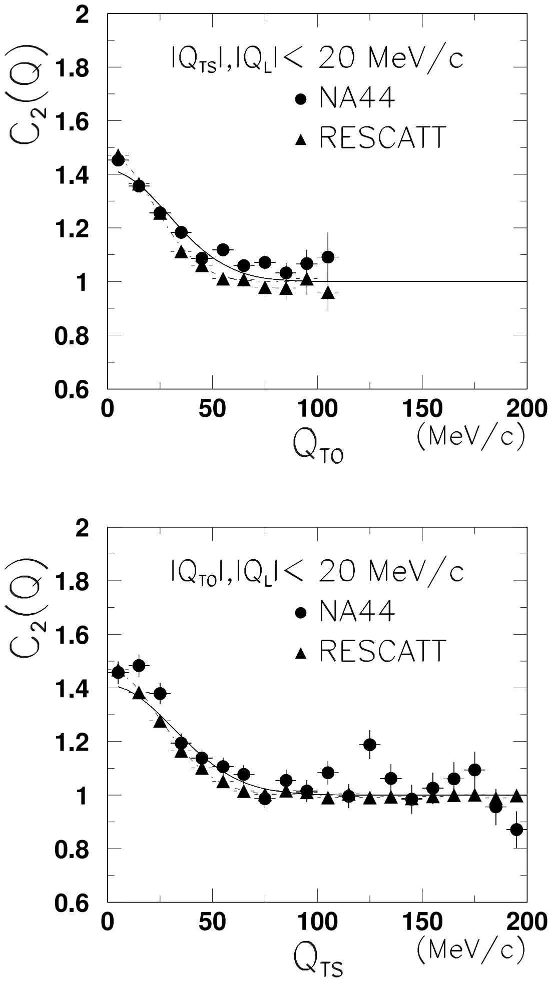

Figure 6.4: Comparisons of the NA44 and rescattering model 44mr $\pi^-\pi^-$ projections of the three-dimensional correlation function. The projections in Q_{TO} and Q_L come from the horizontal setting and the projection in Q_{TS} comes from the vertical setting. Error bars on the data points are statistical only. The fit to the NA44 data is the solid line, and the fit to the rescattering model prediction is the dashed-dotted line.

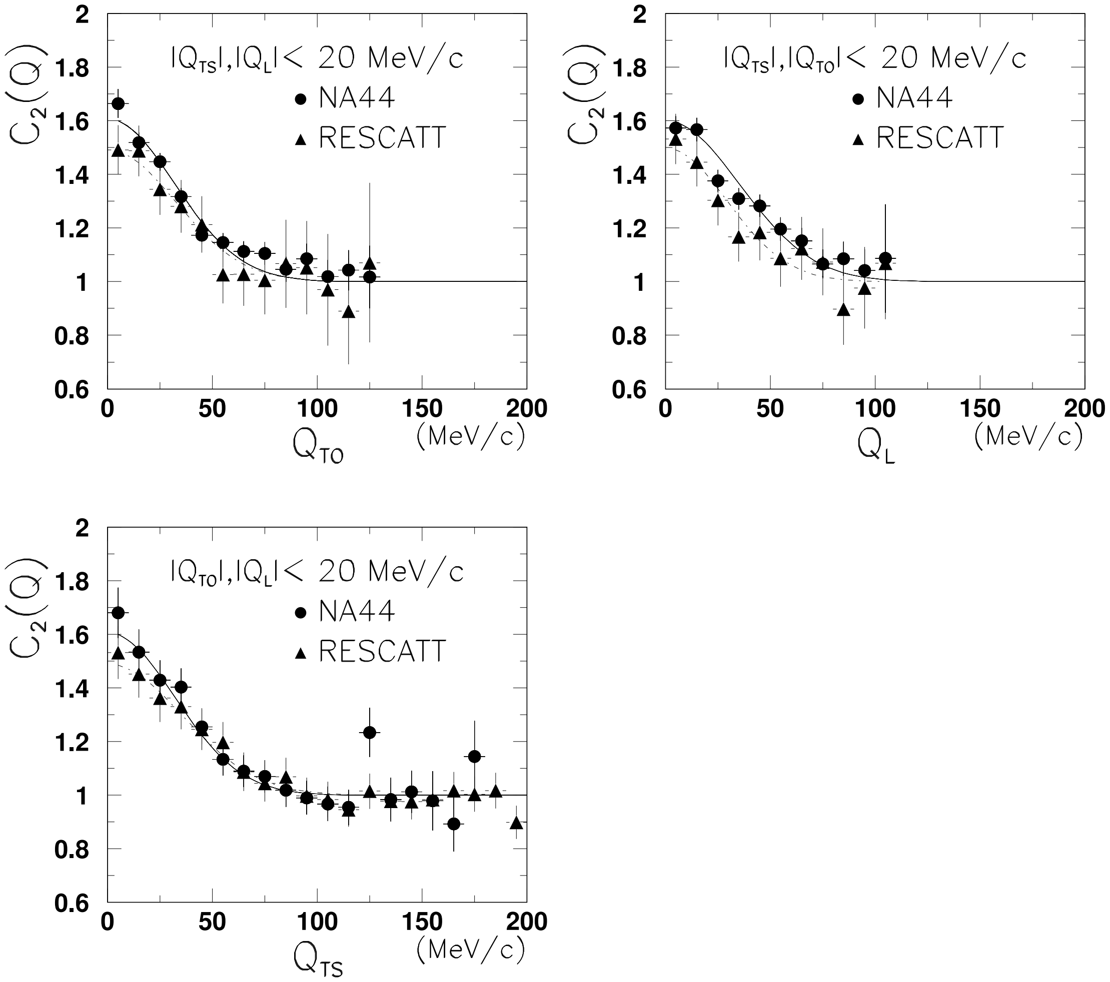

Figure 6.5: Comparisons of the NA44 and rescattering model 131mr $\pi^+\pi^+$ projections of the three-dimensional correlation function. The projections in Q_{TO} and Q_L come from the horizontal setting and the projection in Q_{TS} comes from the vertical setting. Error bars on the data points are statistical only. The fit to the NA44 data is the solid line, and the fit to the rescattering model prediction is the dashed-dotted line.

For the low p_T setting, the model over-predicts the radius and λ parameters. For the high p_T data, the radius parameters from the model are similar to the experimentally measured radius parameters. The model predicts that the λ parameter decreases with increasing p_T and this contradicts the data. It is interesting to note that the predictions of RQMD and the rescattering model are very similar except for the λ parameter for the 131mr setting. This suggests that the rescattering process, which is present in both this model and RQMD, has a large influence on the observed radii. Indeed, it appears as if the collective expansion that leads to a reduction in the measured radius parameters with increasing p_T can be explained almost entirely as an effect of the rescattering process.

Another thing that is interesting to note is that the deviation of the λ parameters from unity can be understood almost entirely in terms of pions from resonance decay. Before the addition of resonances, the rescattering model predicted that the λ parameter should be very close to unity [Hum96]. With the addition of a few resonances, however, the rescattering prediction for the λ parameter is almost consistent with the data. This model does not include some resonances that might be expected to influence the value of the intercept, most noticeably the Λ. Nonetheless, it is possible to conclude that it is not necessary to assume a coherent source of pions in order to explain the experimentally observed λ parameters.

The initial temperature for these calculations is 270 MeV and the initial energy density is 4.88 GeV/fm^3. Lattice QCD calculations predict that the QCD phase transition occurs in a baryon-free environment for a temperature somewhere between 140

MeV and 265 MeV [Lae96]. Bag Model calculations also predict a critical temperature around 140 MeV [Wong94]. Hence it is questionable whether hadronic matter can exist at the extreme temperature and energy density required in order to make the rescattering calculation agree with the experimental data.

6.3 Rescattering + Coulomb Model

Recent NA44 measurements of the transverse mass ($m_T = \sqrt{p_T^2 + m^2}$) dependence π^-/π^+ ratio in 158 GeV/nucleon Pb+Pb collisions [Bog96] show a noticeable enhancement in the π^-/π^+ ratio at low m_t. This enhancement has been interpreted as evidence for a strong Coulomb interaction between the pion emitting source and the outgoing pions [Bog96, BBG97]. The strong central Coulomb potential is created by the primary protons in the projectile and target nuclei.

This section explores the influence of this central Coulomb potential on two-pion Bose-Einstein correlation measurements. The single particle data [Bog96] suggest that central Coulomb effects will be important only for low-p_T pion correlation measurements, but these measurements have been shown to be most sensitive to the lifetime of the pion emitting source [FSS95]. It is thus important to understand the central Coulomb effects in order to extract useful information from pion interferometry measurements.

As input to these calculations, 158 GeV/nucleon Pb+Pb events from the simple rescattering model were used. The rescattering process generates strong position-momentum correlations, which are important for the Coulomb calculations. Coulomb interactions are assumed to not be important during the strong rescattering stage. The effects of the Coulomb interaction are added after freeze-out using an analytic correction to the particle momenta. The model produces a list of particle freeze-out positions and momenta. Coulomb interactions are added by assuming that these particles are produced in a classical Coulomb potential[Bay96]. The average classical Coulomb potential is

$$V_s = \frac{Z_{eff} e^2}{r_a}, \tag{6.9}$$

where Z_{eff} is the effective charge and r_a is the average freeze-out radius. Of course, in a realistic model, each particle is produced in a different Coulomb potential that depends on freeze-out time and position. Using the average Coulomb potential, however, is computationally much simpler and should not change the qualitative conclusions.

Using simple energy and momentum conservation, the momentum of the particle at freeze-out can be related to the momentum of the particle at the detector using

$$E(p) = E(p_i) + V_s, \tag{6.10}$$

where p is the measured momentum of the particle, p_i is the momentum of the particle at freeze-out, $E(p) = (p^2 + m^2)^{1/2}$, and V_s is the effective average Coulomb potential. Note that V_s is positive for positive particles and negative for negative particles. Using this equation, the momentum shift for each particle is calculated:

$$\Delta p = p - p_i. \tag{6.11}$$

Up to this point the calculation is identical to [Bay96]. In [Bay96, PBM97], the π^+/π^- ratio at mid-rapidity is calculated to be,

$$\frac{N(\pi^+)}{N(\pi^-)} = \frac{\sqrt{p_t^2 - 2E(p_t)|V_s| + V_s^2}\,(E(p_t) - |V_s|)}{\sqrt{p_t^2 + 2E(p_t)|V_s| + V_s^2}\,(E(p_t) + |V_s|)} \tag{6.12}$$

The effect of the central Coulomb potential on the measured momentum difference is calculated to be,

$$Q \approx Q_i(1 + \frac{V_s}{p_i}), \tag{6.13}$$

where Q_i is the momentum difference at freeze-out and Q is the measured momentum difference. This formula predicts that negatively charged particle pairs will give a measured source size that is larger than the actual source size and that positively charged pairs will give a measured source size that is smaller than the actual source size.

The simple analytical calculation [Bay96] does not include any directional dependence. The correlation functions in this thesis are typically measured experimentally in the three-dimensional Pratt-Bertsch parameterization. Here, the directional dependence is explicitly considered. Δp is calculated analytically using equation (6.11), and then the directional dependence is added using

$$\vec{p} = \vec{p_i} + \Delta p\ \hat{x}, \tag{6.14}$$

where $\hat{x}$ is the unit vector in the direction of the freeze-out position $\vec{x}$. This approach assumes that the central Coulomb charge is spherically symmetric.

The procedure used in these calculations is the following. Events were generated using the simple rescattering model. This produces a list of pion freeze-out momenta and positions. The Coulomb potential is added using equations (6.10),(6.11), and (6.14). The correlation functions are then calculated using the procedure described previously. The only free parameter in the calculation is magnitude of the average Coulomb potential, V_s.

The average Coulomb potential V_s is found by fitting equation (6.12) to the NA44 data [Bog96]. The data are shown along with the analytical fit to the data in Figure 6.6. The value of V_s extracted from the single particle data is $\approx$5 MeV. This is actually a lower limit on the Coulomb potential since equation (6.12) is the mid-rapidity limit ($y = 2.9$) and the NA44 data were measured over the rapidity range $3.1 < y < 4.1$. This value of V_s is still large enough to have effects on the measured pion correlation functions.

The correlation function is calculated with three values of V_s: $V_s = 0$ (i.e., no Coulomb effects), $V_s = 5$ MeV (i.e., $\pi^+\pi^+$), and $V_s = -5$ MeV (i.e., $\pi^-\pi^-$). Figure 6.7 compares the momentum difference shifts in Q_{TS}, Q_{TS} and Q_L for the positive pion pairs ($V_s = 5$ MeV) and the negative pion pairs ($V_s = -5$ MeV). These momentum difference shifts are then characterized by a mean momentum shift and an RMS deviation of the momentum shift, and the values are listed in Table 6.5. Figure 6.5 and Table 6.5 show that the mean shift in all three components of the momentum difference is small. This is what would be expected since pions of similar momentum should experience roughly the same Coulomb impulse. The RMS deviations of the momentum shift, however, are significantly larger than the mean shifts. This means

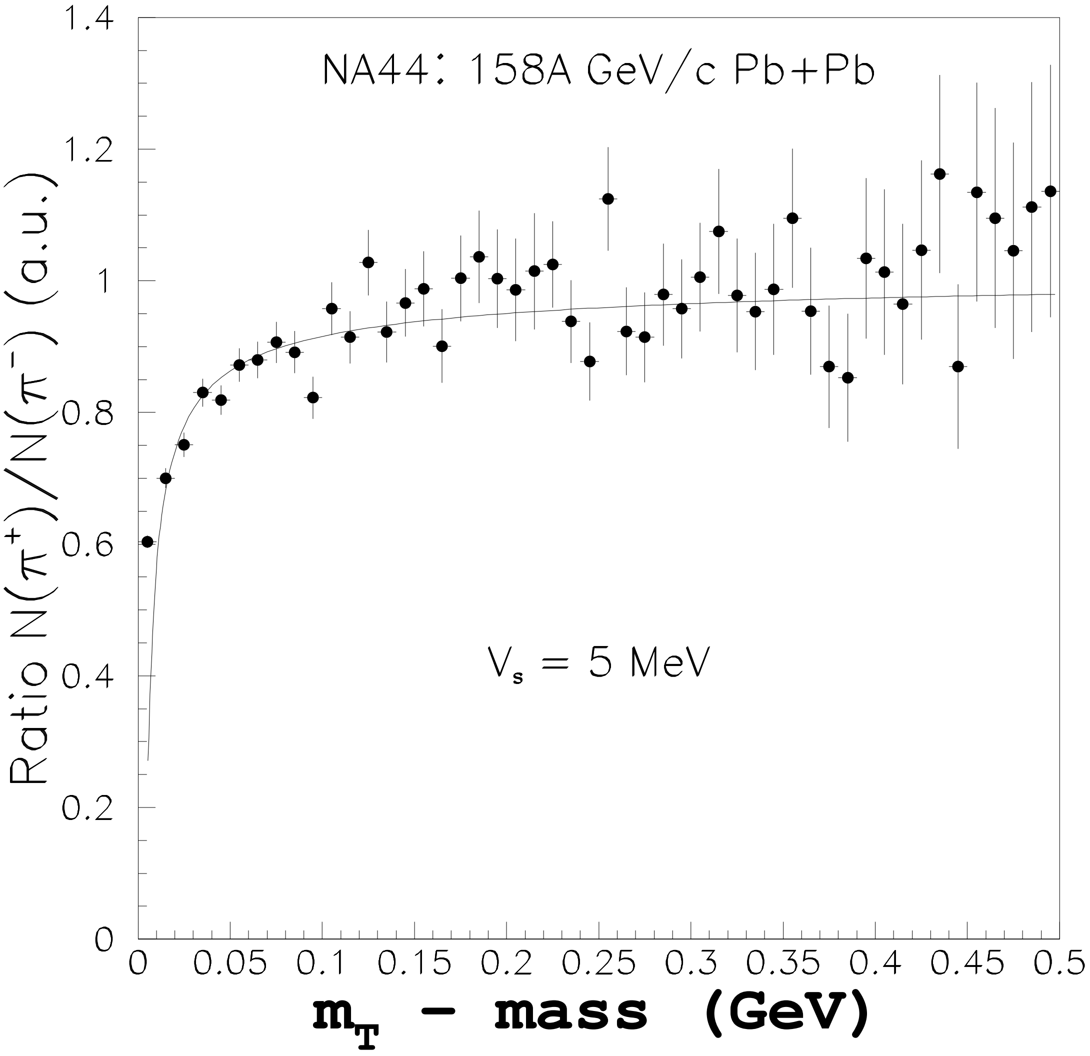

Figure 6.6: The NA44 $\pi+/\pi^-$ ratio compared to the analytical fit to the data. The data are taken from [Bog96].

that although the net momentum difference shift is small, the direction of the momentum difference vector is changed appreciably by the central Coulomb potential.

	$\pi^-\pi^-$		$\pi^+\pi^+$	
	mean(MeV/c)	RMS(MeV/c)	mean(MeV/c)	RMS(MeV/c)
ΔQ_{t_s}	-2.4	6.4	2.5	6.3
ΔQ_{t_o}	-1.6	6.0	1.7	5.9
ΔQ_l	-1.3	5.0	1.5	4.8

Table 6.5: The mean and RMS deviations of the momentum difference shifts caused by the central Coulomb potential for negative and positive pion pairs in the 44mr NA44 acceptance.

The projections of the correlation functions in the NA44 44mr acceptance with and without the central Coulomb potential are shown in Figure 6.8, and the extracted fit parameters are listed in Table 6.6. The extracted radii are smaller for both the positive and negative Coulomb potentials compared to the extracted radii without the Coulomb potential, and the reduction is largest for R_L. The magnitude of the reduction in R_L and λ is largest for the negative pions. The transverse radius parameters (R_{TS} and R_{TO}) are affected only slightly. Comparing R_L and λ for the negative and positive Coulomb potentials with the corresponding NA44 results in Tables 5.2 and 5.4, the addition of the central Coulomb potential seems to reproduce a trend in the data, namely that the λ parameter and R_L are smaller for the $\pi^-\pi^-$ data set. In addition, the addition of the central Coulomb potential brings the rescattering model predictions closer to the measured data.

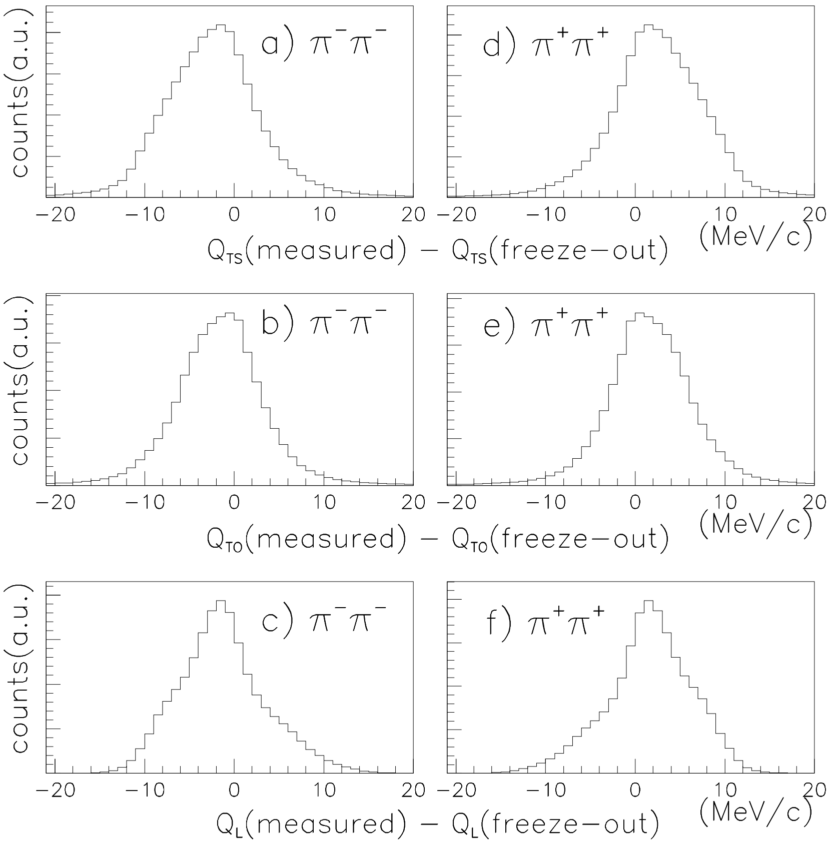

Figure 6.7: The shifts in Q_{TS}, Q_{TO}, and Q_L due to the central Coulomb potential for negative and positive pion pairs. The average Coulomb potential $V_s = 5$ MeV. The calculation is for the NA44 44mr setting.

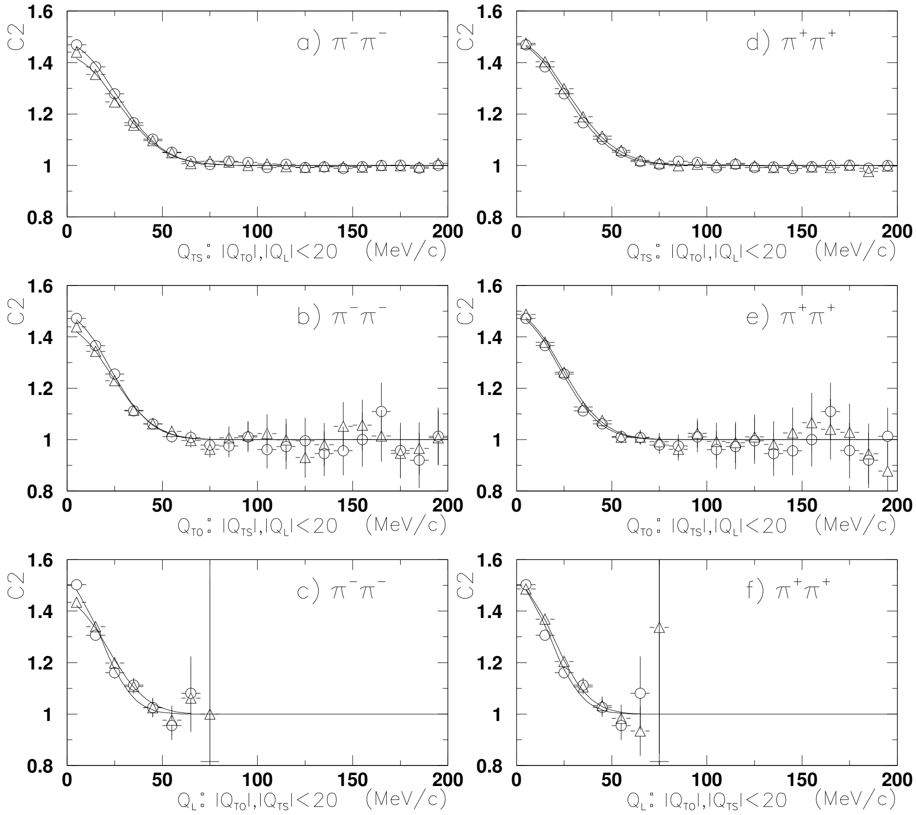

Figure 6.8: The projections of the 44mr correlation functions (C2) in Q_{TS}, Q_{TO}, and Q_L for positive and negative pions (open triangles) compared with the projections without the central Coulomb potential (open circles). The fit functions are also included. The projections are over the lowest 20 MeV in the other momentum difference directions.

V_s(MeV)	R_{t_s}(fm)	R_{t_o}(fm)	R_l(fm)	λ
0.	5.55 ± 0.12	6.37 ± 0.26	8.13 ± 0.63	0.63 ± 0.03
-5.0 ($\pi^-\pi^-$)	5.53 ± 0.09	6.17 ± 0.06	6.73 ± 0.13	0.54 ± 0.01
5.0 ($\pi^+\pi^+$)	5.33 ± 0.10	6.14 ± 0.16	7.38 ± 0.22	0.62 ± 0.02

Table 6.6: The fitted results of the gaussian parameterization of the correlation functions for pions without the central Coulomb potential, with a negative Coulomb potential ($\pi^-\pi^-$), and with a positive Coulomb potential ($\pi^+\pi^+$). These calculations are for the NA44 44mr acceptance.

There are two effects due to the central Coulomb potential that lead to a distortion of the correlation function. The central Coulomb potential introduces a net shift in the momentum difference. This net shift was pointed out in [Bay96], [Bar96]. The net shift in the momentum difference, however, has only a small effect compared to the momentum difference smearing effect. The momentum difference smearing effect, characterized by the RMS of the momentum difference shift distributions, is the more important of the two effects and leads to a reduction of the measured radii and lambda parameters. The effect is similar to the well understood effect of the experimental momentum resolution on the correlation function. The momentum difference smearing due to the central Coulomb potential is similar for Q_{TS}, Q_{TO} and Q_L, but, due to the larger radius in the longitudinal direction, the change in the extracted radius is largest for R_L.

In [Bay96] only the net momentum difference shifts were considered. This leads to the conclusion that positively charged pairs should measure a source size smaller than the true source size and negatively charged pairs should measure a source size larger than the true source size. The present work suggests that both negative and positive pairs measure a source size smaller than the true source size due to the momentum difference smearing effect.

In [Bar96], the influence of the nuclear Coulomb charge on the measured transverse correlation radii is much larger than in the present work and qualitatively different. This is probably due to the different approach used here. In [Bar96], the Klein-Gordon equation is used to find the wave function for a particle originating in a Coulomb potential parameterized by

$$U = \pm Ze^2\Phi(r/\sqrt{2}R_0)/r, \tag{6.15}$$

where Z is the charge number, R_0 is the source radius, and Φ is the error function. In [Bar96], the calculation is for Au+Au collisions at 1 GeV/nucleon. R_0 is estimated to be 4.5 fm and Z is taken to be 160. Equation (6.15) reduces to equation (6.9) in the limit $r > R_0$. In this work, however, equation (6.9) is not actually used to calculate the value of the average Coulomb potential V_s, but instead a value of V_s is extracted from experimental data. This leads to a smaller value for the average Coulomb potential than would be extracted from equation (6.15). If equation (6.9) is evaluated with $Z_{eff} = 160$ and $r_a = 4.5$ fm, a value of $V_s \approx 50$ MeV is extracted, which should be compared to value $V_s = 5$ MeV extracted from the experimental data and used for these calculations. In addition, it is assumed in the present work that the net nuclear Coulomb charge is spherically symmetric, whereas [Bar96] only looks at the effect of the Coulomb field in the transverse direction. The current model has in fact been examined for the case in which the Coulomb field is assumed to have only a transverse component, and in that case it was found that the transverse radii R_{TO} and R_{TS} are reduced much more strongly than for the central potential used in the calculations presented here. Even in the limit where the Coulomb field is assumed to have only a transverse component, the current work disagrees qualitatively with [Bar96] in that the Coulomb potential reduces all measured correlation radii whereas [Bar96] predicts that the measured sideward radius R_{TS} should be larger than the true source size for low-p_T $\pi^-\pi^-$ pair measurements.

The problem of the central Coulomb potential on the measured pion correlation functions was also addressed in Ar + KCl collisions at 1.8 GeV/nucleon [ZAJ84]. The approach used, however, was much different than that used here. In [ZAJ84], an attempt was made to correct the experimental data for the central Coulomb distortions. The momentum shift of each pion due to the central Coulomb charge was calculated using a formalism correct in both the classical and quantum mechanical limit [GK79]. It was found that the central Coulomb effect on the measured correlation function was small compared to the experimental error on the measured radii. The measured radii in [ZAJ84] were much smaller than the measured radii in Pb+Pb collisions at 158 GeV/nucleon, so the momentum difference smearing effect should be much less important.

CHAPTER 7

CONCLUSIONS

High energy Pb+Pb collisions at the CERN SPS create the hottest and densest hadronic matter currently accessible in a laboratory. By accessing hadronic matter under such extreme conditions, it is possible to test the prediction of a QCD phase transition. Experiment NA44 looks at the hadronic observables originating from such collisions with the goal of understanding the hadronic freeze-out conditions. The measurements can then be used to test various models and thus look for the QCD phase transition.

Pion interferometry measures indirectly both the volume of the system and the freeze-out dynamics. The experimental HBT results presented show that at freeze-out the system is larger than the initial projectile. The similarity between R_{TO} and R_{TS} suggests that the source is either short-lived, in contradiction with the predictions for a first order QCD phase transition, or that the source is somewhat opaque. In addition, the reduction of the HBT radius parameters with increasing p_T suggest that the system has strong collective transverse expansion at freeze-out. By comparing the $\pi^-\pi^-$ and $\pi^+\pi^+$ interferometry measurements it was shown that the $\pi^+\pi^+$ radius parameters are slightly larger, but that this difference is not statistically significant when the data are compared directly.

In comparison to the S+Pb system at a similar energy, it is clear the the radius parameters do not scale directly with the size of the projectile. This supports the conclusion that the HBT results are strongly modified by the dynamics of the system. Comparing the results to other heavy projectile-target combinations at lower energies, it was shown that the increase in the interferometric radius parameters was large when going from a projectile energy of 1.26 GeV/nucleon to 10.8 GeV/nucleon, but that no such increase was seen in going from a projectile energy of 10.8 GeV/nucleon to a projectile energy of 158 GeV/nucleon.

The RQMD model does a reasonable job predicting the pion interferometry measurements, although the radius parameters predicted for the NA44 44mr setting are slightly larger than the measured radius parameters. RQMD also supports the picture that the decrease in the radius parameters with increasing p_T comes from the expansion dynamics of the system.

A purely hadronic rescattering model can also reproduce the data equally as well as RQMD, but the initial conditions needed may be beyond the limits of hadronic matter. The rescattering model also predicts the measured λ parameters reasonably well, and this suggests that the deviation of the λ parameter from unity is due to the contribution of resonances in the pion sample and not a result of a coherent component of the source.

Finally, it was shown using the rescattering model coupled to a classical Coulomb model that final state central Coulomb interactions lead to a reduction in the measured λ and radius parameters due to a smearing of the momentum difference. Adding the central Coulomb interaction improved the agreement between the rescattering model and the data.

Appendix A

KINEMATICAL VARIABLES

Throughout this work, the convention is used that $\hbar = c = 1$.

The NA44 cartesian coordinate system is defined as the following. The beam axis defines the z direction, and the center of the NA44 azimuthal acceptance transverse to the beam direction defines the x direction. The y direction is perpendicular to these two directions, and is hence the vertical direction.

The transverse momentum is defined as

$$p_T = \sqrt{p_x^2 + p_y^2}. \tag{A.1}$$

The momentum in the beam direction is usually expressed in terms of the rapidity

$$y = \frac{1}{2} ln(\frac{E + p_z}{E - p_z}) = tanh^{-1}(\frac{p_z}{E}), \tag{A.2}$$

where E is the energy of the particle. The rapidity is additive like a gallilean velocity, and rapidity differences are invariant under a Lorentz transformation. In the limit $p_z \ll E$, the rapidity reduces to β where $\beta = v/c$.

If a sufficient number of collisions are averaged over it can be assumed that the source is azimuthally symmetric. For such sources, the physics observables are only a function of the transverse momentum and the rapidity.

Another variable used is the transverse mass

$$m_T = \sqrt{p_T^2 + m^2}, \tag{A.3}$$

where m is the mass of the particle. The energy and momentum in the z direction for a particle can be written as

$$E = m_T \, cosh(y), \tag{A.4}$$

$$p_z = m_T \, sinh(y). \tag{A.5}$$

For a thermalized system, the single particle spectra should follow a Boltzmann distribution:

$$\frac{1}{m_T}\frac{dN}{dm_T} \propto e^{-m_T/T(y)} \tag{A.6}$$

where $T(y)$ is the slope parameter at fixed rapidity y.

For non-identified particles, it is impossible to calculate the rapidity. It is possible, however, to calculate a pseudo-rapidity defined by

$$\eta \equiv -ln \, tan(\theta/2). \tag{A.7}$$

In the limit $p \gg m$ one can expand equation A.2 and find that the rapidity is approximately equal to the pseudo-rapidity:

$$y = \frac{1}{2} ln \frac{cos^2(\theta/2) + m^2/4p^2 + \cdots}{sin^2(\theta/2) + m^2/4p^2 + \cdots} \approx \eta. \tag{A.8}$$

Appendix B

SYSTEMATIC ERRORS

Systematic errors are very tricky to evaluate, especially for HBT measurements. Basically there are two types of systematic errors. There are the "known" systematic errors which are found by trying every possible thing that one can think of that might change the results. Everything not found in this random process becomes an "unknown" systematic error which is by definition not included in the systematic error calculation. This appendix will examine the known systematic errors and the effect they have on the results.

Systematic errors are found and evaluated by varying the analysis conditions and cuts used in the analysis. The "standard" parameters used in the analysis are listed in Table B.1 along with the variations used in the systematic error analysis. The meaning of each parameter is explained below.

NSC_CUT is minimum number of strip chamber hits used for a valid pair. In the reconstruction, a track is require to have valid hits in 3 of the 4 strip chamber planes. This means that a pair of tracks can have either 6,7,or 8 strip chamber hits. If NSC_CUT=7, then pairs with only 6 strip chamber hits are thrown out in the real data, background data, and MC data.

PC_CUT is the minimum separation, in cm, for two tracks at the pad chamber. This cut is made because the pad chamber is unable to resolve extremely close hits. Ideally, this effect should be taken care of in the MC, but it is very difficult to evaluate whether or not the MC calculates the efficiency for resolving nearby pairs at the PC correctly.

RESNEW is a factor that changes the momentum resolution of the spectrometer assumed during the acceptance correction. The momentum resolution calculated by the MC is nearly correct, but it is very difficult to be certain. In order to account for this uncertainty, the MC momentum resolution is varied by $\pm 20\%$.

The "# of λ's" refers to whether or not the horizontal and vertical settings are allowed to have different λ parameters during the iterative correction process. Since the corrections depend on the assumed shape of the correlation function, allowing the horizontal and vertical settings to have different λ parameters changes the values of the correlation function at low $\vec{Q}$ for cases in which the two data sets have slightly different λ parameters.

DYH2MIN is the minimum y separation between valid tracks at hodoscope 2. Although tracks that hit two different hodoscope slats should have no efficiency problems in the y direction, this is not true since the y position of a track at H2 used for the momentum calculation is the fitted position and not the raw position. It was found that strip chambers have problems resolving tracks that are close in y, and this can lead to ghost pairs. These ghost pairs can be eliminated by requiring that the tracks are separated by at least 1.0 cm in the y direction at H2. These ghosts are especially problematic for the 131mr vertical setting since tracks are very closely spaced in y at the first strip chamber. Hence, the standard 131mr case uses DYH2MIN=1.0 cm.

Parameter	Standard	Variation
NSC_CUT	6	7
PC_CUT (cm)	0.5	1.0
RESNEW	1.0	1.2
		0.8
# of λ's	1	2
DYH2MIN (cm)	0.0	1.0

Table B.1: The standard HBT cuts and the variations used in the systematic error analysis. The meaning of each cut is explained in the text. Note that for the 131mr $\pi^+\pi^+$ data, the standard DYH2MIN is 1.0 cm and the variation is 0.0 cm.

The effects of changing the analysis conditions on the fitted results are shown in Table B.2 for the 44mr $\pi^-\pi^-$ three-dimensional fits. R_{TO} and R_L change very little as the analysis conditions are varied, while R_{TS} varies much more dramatically. In particular, using NSC_CUT=7 or allowing the horizontal and vertical settings to have different λ parameters causes R_{TS} to increase by roughly 3σ compared to the standard case. These two variations also have the largest effect on the λ parameter. Using NSC_CUT=7 causes the λ parameter to increase by 2.5σ compared to the standard case. When the horizontal and vertical settings are allowed to have different λ parameters, the vertical λ parameter is significantly larger than the horizontal λ parameter. There are clearly systematic errors that need to be taken into account.

At least two methods can be used to calculate systematic errors on the fit parameters. In both methods, analysis uncertainties are found using the the trial and error

Case	λ (λ_{vert})	R_{TO} (fm)	R_{TS} (fm)	R_L (fm)
Standard	0.50±0.02	4.97±0.17	4.60±0.23	6.13±0.26
NSC_CUT=7	0.55±0.02	4.72±0.17	5.26±0.31	5.91±0.27
PC_CUT=1.0	0.50±0.02	5.01±0.17	4.65±0.24	6.13±0.26
RESNEW=1.2	0.50±0.02	4.94±0.16	4.27±0.21	6.17±0.26
RESNEW=0.8	0.49±0.02	4.92±0.17	4.73±0.25	6.01±0.27
2 λ's	0.48±0.02 (0.66±0.03)	5.04±0.16	5.47±0.25	6.00±0.27
DYH2MIN=1.0	0.46±0.02	4.98±0.18	4.56±0.27	5.86±0.28

Table B.2: Fitted results of three-dimensional Gaussian parameterizations of the 44mr $\pi^-\pi^-$ correlation functions in Q_{TO}, Q_{TS} and Q_L using the Coulomb wave correction. The errors are statistical only.

method. The method used in this thesis was explained in section 4.6. The systematic errors on the data points are calculated by varying the analysis conditions and calculating what effect the variations have on the data points. The systematic errors are then incorporated into the fit. This method has the advantage that the statistical and systematic covariance matrices are additive as shown in equation 4.25. This method also has several disadvantages. The fit values change when the systematic errors are added to the fit. This can be seen by comparing the "standard" results in Table B.2 to the results presented in Table 5.2. In addition, it is impossible to factorize the contributions of the systematic and statistical errors to the total error. In fact, the values of the quoted errors increase only slightly when the systematic errors are added.

The alternative method is to calculate the RMS deviation of the fit parameters R_i as the analysis conditions are changed and call this the systematic error. For this method, the systematic error is

$$\sigma_{sys}^2(R_i) = \frac{1}{N-1}\sum_{i=1}^{N}(R_{iN} - \bar{R}_i)^2, \tag{B.1}$$

where N is number of variations, R_{iN} is the fit value for parameter i for the Nth case, and $\bar{R}_i$ can be either the mean value of the fit parameter R_i or value of R_i from one's favorite case. The total error is then found by adding the systematic and statistical errors in quadrature:

$$\sigma_{tot}^2(R_i) = \sigma_{stat}^2(R_i) + \sigma_{sys}^2(R_i). \tag{B.2}$$

This assumes that the statistical and systematic errors are independent and the the systematic errors on the fit parameters are uncorrelated. As shown earlier, the systematic errors on R_{TS} and λ are highly correlated, so part of this assumption is incorrect.

In spite of the problems with both methods of calculating systematic errors, the methods will be compared. Table B.3 compares the results of the two methods of systematic error calculation: "Method 1" is the method outlined in section 4.6, and "Method 2" is the method discussed in the previous paragraph. for method 2, the mean value of each fit parameter is used in equation B.1. The two methods yield equivalent results for R_{TO} and R_L. The result for the λ parameter is the same although method 2 gives a larger error estimate. R_{TS} differs by 1σ between the two methods, and the error estimate is larger using method 2. It is interesting to note that in the case there there is a known correlated error between two fit parameters (R_{TS} and λ), method 2 gives a larger error estimate on compared to method 1.

Error Method	λ	R_{TO} (fm)	R_{TS} (fm)	R_L (fm)
Method 1	0.495 ± 0.023	4.88 ± 0.21	4.45 ± 0.32	6.03 ± 0.35
Method 2	0.497 ± 0.034	4.94 ± 0.20	4.79 ± 0.48	6.03 ± 0.29

Table B.3: Comparison of the results of three-dimensional Gaussian parameterizations of the 44mr $\pi^-\pi^-$ correlation functions in Q_{TO}, Q_{TS} and Q_L using the two methods of systematic error calculations.

Bibliography

[Alb95] Th. Alber et al. (NA35 Collaboration), Phys. Rev. Lett. **74** (1995) 1303.

[Alb95b] Th. Alber et al. (NA35 Collaboration), Z. Phys. **C 66** (1995) 77.

[Alb97] Th. Alber et al. (NA35 Collaboration), Z. Phys. **C73** (1997) 443.

[AS95] S.V. Akkelin, Yu. M. Sinyukov, Phys. Lett. **B356** (1995) 525.

[Bar96] H.W. Barz, Phys. Rev. **C53** (1996) 2536.

[Bar97] J. Barrette et al. (E877 Collaboration), Phys Rev. Lett. **78** (1997) 2916.

[Bay69] G. Baym, **Lectures on Quantum Mechanics**, Addison Wesley (1969).

[Bay96] G. Baym and P. Braun-Munzinger, Nucl. Phys. **A610** (1996) 286c.

[BBG97] H.W. Barz, J.P. Bondorf, J.J. Gaardhøje, H. Heiselberg, Phys. Rev. **C56** (1997) 1553.

[Bea97] I. G. Bearden et al. (NA44 Collaboration), to be submitted to Phys. Rev. C.

[Bea97b] I.G. Bearden et al. (NA44 Collaboration), Phys. Rev. Lett. **78** (1997) 2080.

[BEK94] H. Beker et al. (NA44 Collaboration), Z. Phys. **C64** (1994) 209.

[BEK95] H. Beker et al. (NA44 Collaboration), Phys. Rev. Lett. **74** (1995) 3340.

[Ben79] W. Benenson et al., Phys. Rev. Lett. **43** (1979) 683.

[BGT88] G. Bertsch, M. Gong, and M Tohyama, Phys. Rev. **C 37** (1988) 1896.

[BGJ90] D.H.Boal, C.Gelbke, B.K.Jennings, Rev. Mod. Phys. **64** (1990) 553.

[BOG93] H. Boggild et al. (NA44 Collaboration), Phys. Lett. **B302** (1993) 510.

[BOG95] H. Boggild et al. (NA44 Collaboration), Phys. Lett. **B349** (1995) 386.

[Bog96] H. Boggild et al. (NA44 Collaboration), Phys. Lett. **B372** (1996) 339.

[Bos93] H. Bossy et al., Phys. Rev. **C47** (1993) 1659.

[Bow85] M.G. Bowler, Z. Phys **C29** (1985) 617.

[BOW88] M.G. Bowler, Z. Phys **C39** (1988) 81.

[BRO74] K.L.Brown, and Ch. Iselin, CERN 74-2 (1974).

[BRO80] K.L.Brown, R.Rothacker, D.C.Carey, and Ch. Iselin, CERN 80-04 (1980).

[BRU88] R. Brun and D. Lienart, **HBOOK Users Guide**, CERN Program Library Y250 (1988).

[Cha91] A. D. Chacon et al., Phys. Rev. **C43** (1991) 2670.

[CNH95] S. Chapman, J.R. Nix, U. Heinz, Phys Rev. **C52** (1995) 2694.

[CSH95] S. Chapman, P. Scotto, U. Heinz, Phys. Rev. Lett. **22** (1995) 4400.

[FAB95] C.W.Fabjan et al., Nucl. Inst. Meth. **A367** (1995) 240.

[FSS95] D.E. Fields, J.P. Sullivan, J. Simon-Gillo, H. van Hecke, B.V. Jacak and N. Xu, Phys. Rev. **C52** (1995) 986.

[GGLP60] G. Goldhaber, S. Goldhaber, W. Lee, and A. Pais, Phys. Rev. **120** (1960) 300.

[GK79] M. Gyulassy and S.K. Kaufmann, Nucl. Phys. **A362** (1981) 503.

[GKW79] M. Gyulassy, S.K. Kaufmann, and L.W. Wilson, Phys. Rev. **C20** (1979) 2267.

[HBT56] R. Hanbury-Brown and R.Q. Twiss, Nature **178** (1956) 1046.

[HAR97] D. Hardtke, *Maxmiss = 1 or 0?* NA44 Note (1997).

[Hum94] T.J. Humanic, Phys. Rev. **C50** (1994) 2525.

[Hum96] T.J. Humanic, Phys. Rev. **C53** (1996) 901.

[Hum97] T.J. Humanic, Submitted to Phys. Rev. C.

[Lae96] E. Laermann, Nucl. Phys. **A610** (1996) 1c.

[Lee93] Y.Y. Lee, **Bose-Einstein Correlation of High Energy Heavy Ion Collision at CERN SPS**, Ph.d. Thesis, University of Pittsburgh (1993).

[MAE94] N.Maeda et al., Nucl. Inst. Meth. **A346** (1994) 132.

[MES61] A. Messiah, **Quantum Mechanics**, North-Holland Publishing Company (1961).

[MIN92] **MINUIT - Function Minimization and Error Analysis**, CERN Program Library D506 (1992).

[PAN93] S. Pandey, **Investigation of the Space-Time Evolution of the Interaction Region in Heavy Ion Collisions using Bose-Einsten Interferometry Techniques**, Ph.d. Thesis, University of Pittsburgh (1993).

[PBM97] P. Braun-Munzinger, Private Communication.

[PCZ90] S. Pratt, T Csörgő, and J. Zimányi, Phys. Rev. **C42** (1990) 2646.

[PEI93] T. Peitzmann, Z. Phys. **C 59** (1993) 127.

[Pra84] S. Pratt, Phys. Rev. Lett. **53** (1984) 1219.

[Pra86] S. Pratt, Phys Rev. **D33** (1986) 1213.

[Pra86b] S. Pratt, Phys Rev. **D33** (1986) 72.

[SBJ93] J. P. Sullivan, M. Berenguer, B. V. Jacak, S. Pratt, M. Sarabura, J. Simon-Gillo, and H. van Hecke, Phys Rev. Lett. **70** (1993) 3000.

[Sor95] H. Sorge, Phys. Rev. **C52** (1995) 3291.

[SKM90] H. Sorge, A.v. Keitz, R. Mattiello, H. Stöcker, W. Greiner, Z. Phys. **C47** (1990) 629.

[SPE94] M. Spegel, **Cathode Pad Chambers on the Trail of the Quark-Gluon Plasma**, Masters Thesis, Technical Univerity of Vienna (1994).

[SSG89] H. Sorge, H. Stöcker, W. Greiner, Nucl. Phys, **A498** (1989) 567c.

[SSG89b] H. Sorge, H. Stöcker, W. Greiner, Ann. Phys, **192** (1989) 266.

[Sul82] J.P. Sullivan et al., Phys Rev **C25** (1982) 1499.

[SX96] B.R. Schlei, N. Xu, Phys Rev **C54** (1996) R2155.

[Wong94] C-Y Wong, **Introduction to High-Energy Heavy-Ion Collisions**, World Scientific (1994).

[ZAJ84] W.A. Zajc et al., Phys. Rev. **C29** (1984) 2173.